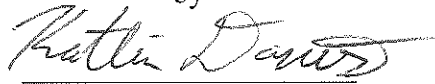


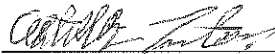
**Experimental and Computational Investigation of a Dual-Bell Nozzle**

A Major Qualifying Project Report  
Submitted to the Faculty of the  
WORCESTER POLYTECHNIC INSTITUTE  
in Partial Fulfillment of the Requirements for the  
Degree of Bachelor of Science  
in Aerospace Engineering

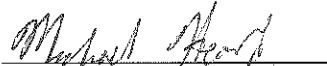
by

  
\_\_\_\_\_

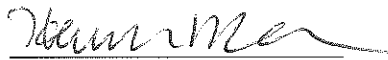
Katlin Davis

  
\_\_\_\_\_

Elizabeth Fortner

  
\_\_\_\_\_

Michael Heard

  
\_\_\_\_\_

Hannah McCallum

  
\_\_\_\_\_

Hunter Putzke

April 23, 2014

Approved by:

  
\_\_\_\_\_

Professor John J. Blandino, Advisor  
Aerospace Engineering Program  
Mechanical Engineering Department, WPI

## **Abstract**

Increased interest in the launch of nanosatellites has driven the development of alternative, more efficient, rocket nozzles. One such option is the dual-bell nozzle (DBN), in which the geometry is designed to achieve two ideal design points over the ascent profile, resulting in a higher average specific impulse for the booster stage compared to a conventional nozzle. This project involved the design of a DBN, which was then modeled using ANSYS Fluent. A scaled DBN was also fabricated and tested in an indraft supersonic wind tunnel. Results from the experimental characterization of the DBN, using schlieren imaging of flow structures, are presented and found to be qualitatively consistent with simulation results. Results of the Fluent simulations for a full-scale DBN and the scaled DBN tested in the wind tunnel are also presented.

*“Certain materials are included under the fair use exemption of the U.S. Copyright Law and have been prepared according to the fair use guidelines and are restricted from further use.”*

# Acknowledgements

We would like to thank the following individuals and groups for their help and support throughout the entirety of this project:

- Professor John Blandino for providing direction and guidance as our project advisor
- Zach Taillefer for running the vacuum chamber during wind tunnel testing
- Kevin Arruda and Matt DiPinto for helping with the machining of the wind tunnel
- Jonathon Jones for providing NanoLaunch vehicle data and ascent profiles
- Professor Adrianna Hera for providing Fluent instruction

# Authorship

<b>Section</b>	<b>Author</b>
<b><i>Introduction</i></b>	HLGM
<b><i>Background</i></b>	
2.1, 2.1.2, 2.1.3	KBD
2.1.1, 2.2	HLGM
2.3	ECF
2.4.1, 2.4.2	MWH
2.4.3, 2.4.4	HJP
<b><i>Methodology</i></b>	
3.1	KBD
3.2	ECF
3.3	HJP
3.4, 3.5	HLGM
<b><i>Experimental Procedures</i></b>	
4.1.1, 4.1.2, 4.1.3, 4.1.4, 4.2.3	KBD
4.3, 4.3.1	ECF
4.3.2, 4.3.3	KBD
<b><i>Numerical Simulation</i></b>	
5.1.1, 5.3.2	HLGM
5.1.2, 5.3.3, 5.3.4	HJP
5.2, 5.3.1	MWH
<b><i>Analysis and Discussion</i></b>	
6.1	HJP
6.2	HLGM
6.3	ECF
<b><i>Conclusion and Recommendations for Future Work</i></b>	
7.1	HLGM
7.2	MWH
<b><i>Appendix A: AIAA Paper</i></b>	ALL
<b><i>Appendix B: How to use the Schlieren System</i></b>	KBD
<b><i>Appendix C: Fluent Contours of Pressure</i></b>	HLGM, HJP, MWH
<b><i>Appendix D: Parabolic Coefficient Calculations</i></b>	HLGM
<b><i>Appendix E: Matlab Script</i></b>	HLGM

# Table of Contents

Abstract.....	i
Acknowledgements.....	ii
Authorship.....	iii
Table of Contents.....	iv
Table of Figures.....	viii
Table of Tables.....	xii
1 Introduction.....	1
2 Background.....	3
2.1 Nozzle Background.....	3
2.1.1 Advanced Nozzles.....	6
2.1.2 Dual-Bell Nozzle History.....	9
2.1.3 Nozzle Comparisons.....	10
2.2 Application.....	13
2.3 Schlieren Imaging.....	14
2.3.1 Optical Principles.....	15
2.3.2 Applications to Flow Regimes.....	16
2.3.3 Schlieren vs. Shadowgraph Techniques.....	17
2.3.4 Schlieren System Types.....	18

2.4	Computational Fluid Dynamics .....	19
2.4.1	Flow Regimes.....	19
2.4.2	Turbulence Models.....	20
2.4.3	FEM vs. FVM .....	21
2.4.4	Turbulence Model Comparisons .....	22
3	Methodology.....	25
3.1	Supersonic Wind Tunnel.....	25
3.2	Schlieren System.....	26
3.3	COMSOL vs. Fluent .....	28
3.4	Thrust Optimized Parabolic Contours.....	29
3.5	Dual-Bell Nozzle Design .....	33
4	Experimental Procedures.....	37
4.1	Setup and Experiments.....	37
4.1.1	Alignment and Focusing .....	37
4.1.2	Updates to Existing Schlieren System .....	38
4.1.3	Optimization and Specific Setup.....	41
4.1.4	System Validation Experiments .....	44
4.2	Manufacturing Test Nozzles .....	48
4.2.1	CAD Nozzle Modeling.....	49
4.2.2	Manufacturing Constraints .....	50



6.2	Full-Scale Nozzle Performance Comparison .....	100
6.3	Physical Interpretation.....	102
7	Conclusion and Recommendations for Future Work .....	104
7.1	Conclusion.....	104
7.2	Recommendations for Future Work.....	105
8	References .....	108
	Appendix A: AIAA Paper.....	110
	Appendix B: How to Use the Schlieren System.....	120
	Appendix C: Fluent Contours of Pressure .....	122
	Appendix D: Parabolic Coefficient Calculations.....	127
	Appendix E: MATLAB Scripts .....	130



# Table of Figures

Figure 1: A Dual-Bell Nozzle [Copyright ©Nasuti, F., Onofri, M., & Martelli, E., 2005 [4]]..... 5

Figure 2: Rao Parabolic Contour [Copyright Kulhanek 2012[6]] ..... 7

Figure 3: FSS vs. RSS within a conventional nozzle [Copyright © Hagemann and Frey 2008 [8]]..... 8

Figure 4: A shadowgram (left) and a schlieren image (right) [Copyright © Settles 2001 [13]]..... 17

Figure 5: Conventional Z-type system [Copyright © Settles 2001 [13]] ..... 18

Figure 6: A body placed in incompressible and compressible flow [Copyright © Auld and Srinivas 2006 [16]] ..... 19

Figure 7: Flow near boundary layer for laminar and turbulent flow [Copyright © NASA Glenn Research center 2000 [17]] ..... 20

Figure 8: Existing Schlieren setup. .... 26

Figure 9: TOP nozzle based on Rao's approximation [Copyright © Kulhanek, 2012 [6]].  
..... 30

Figure 10: Rao Contours for different altitudes..... 33

Figure 11: Dual-bell contour connecting two Rao contours designed for different ambient pressures..... 34

Figure 12: Dual-bell nozzle with normalized axes ..... 35

Figure 13: Dual-bell nozzle with labeled sections (axes scaled for clarity) ..... 35

Figure 14: Solid model of optical plate..... 40

Figure 15: Schlieren image of a candle flame ..... 45

Figure 16: Schlieren image of a heat gun .....	46
Figure 17: Schlieren Image of a Jet of Air.....	46
Figure 18: Schlieren image of the interference between a candle flame and a jet of air ..	47
Figure 19: Schlieren image of non-interference between a candle flame and a jet of air.	48
Figure 20: SSWT CAD model from the 2013 MQP [27].....	50
Figure 21: CAD model of new set-up with dual-bell contours.....	50
Figure 22: Wind tunnel set-up .....	52
Figure 23: Test section with labeled parts .....	53
Figure 24: Fixture plate attached to CNC machine .....	54
Figure 25: Dual-bell contour during machining process using the fixture plate .....	55
Figure 26: Lap joint used for O-ring joining surfaces .....	57
Figure 27: Test Setup.....	58
Figure 28: Normal shock with Rao Contours .....	60
Figure 29: Normal Shock with Angled Shape in Rao Contours.....	61
Figure 30: Early Development of Boundary Layer Structures .....	62
Figure 31: Advanced Development of Boundary Layer Structures.....	62
Figure 32: Shock structure at inflection point.....	63
Figure 33: Boundary layer flow features .....	64
Figure 34: Throat region shock and boundary feature.....	65
Figure 35: Series of boundary flow features.....	65
Figure 36: Rao nozzle mesh with downstream section.....	66
Figure 37: Dual bell nozzle mesh with downstream section .....	68
Figure 38: Rao Wind Tunnel Contour Mesh .....	70

Figure 39: Dual-Bell Wind Tunnel Contour Mesh.....	70
Figure 40: Key for Table 8.....	73
Figure 41: Fluent method of solving governing equations [Copyright © Fluent Inc., 2006] .....	75
Figure 42: Rao Mach contours with chamber pressures of 101325 Pa (1 atm) and back pressures of a) 6.6 Pa, b) 100 Pa, c) 10,000 Pa.....	78
Figure 43: Rao Mach contours with chamber pressures of 101325 Pa and back pressures of a) 25,000 Pa and b) 50,000 Pa.....	79
Figure 44: Rao Mach contour with a chamber pressure of 1 atm and a back pressure of 75,000 Pa.....	80
Figure 45: Dual-bell Mach contours. Top design pressure to 35.7 Pa; bottom atmospheric pressure to 35.7 Pa.....	82
Figure 46: Dual-bell Mach contours for design point pressure ratios of 150 (top) and 1000 (bottom).....	84
Figure 47: Dual-bell Mach contours for pressure ratios of 4.05, 10, and 20.26 in order from top to bottom.....	86
Figure 48: Dual-bell Mach contours for pressure ratios of 50 (top) and 100 (bottom) ....	88
Figure 49: Comparison of Mach Contours at Varying Back Pressures in Rao Nozzle Wind Tunnel Contour.....	90
Figure 50: Comparison of Mach Contours for the Dual-bell Contours.....	93
Figure 51: Fluent "schlieren" image at a pressure ratio of 4.....	97
Figure 52: Shock wave imaged using Fluent "schlieren" settings at a BP of 10.....	97
Figure 53: Genesis of the flow features in the Rao test section.....	98

Figure 54: Fluent "schlieren" imaging at a pressure ratio of 10. ....	98
Figure 55: Fluent "schlieren" image at a pressure ratio of 4.....	99
Figure 56: Fluent "schlieren" image at a pressure ratio of 10. ....	100
Figure 57: Wind Tunnel with Dual-Bell Contours Installed .....	105
Figure 58: Example of Light Interference .....	121

## Table of Tables

Table 1: Comparison of Nozzle Contour Types .....	12
Table 2: Comparison of Turbulence Modeling Systems .....	24
Table 3: Summary of Results from Optimization Exercise .....	42
Table 4: Optimal Configuration for Schlieren System .....	43
Table 5: Edge sizing definitions for mesh generation of Rao Nozzle .....	67
Table 6: Edge sizing definitions for mesh generation of dual-bell nozzle .....	68
Table 7: Edge Sizing Definitions for the Rao Wind Tunnel Contour Mesh.....	71
Table 8: Edge Sizing Definitions for the Dual-Bell Wind Tunnel Contour Mesh .....	72
Table 9: Statistics for Wind Tunnel Contour Meshes.....	73
Table 10: Summary of Convergence and Mass Flow Error for Rao Wind Tunnel Contour Cases .....	90
Table 11: Summary of Dual-Bell Contour Testing.....	93
Table 12: Dual-bell nozzle specific impulse calculation parameters.....	101
Table 13: Rao nozzle specific impulse calculation parameters .....	102

# 1 Introduction

The increasing prevalence of nanosatellites and lack of small payload (<10 kg) launch vehicles combined with the demand for higher rocket performance has led to the critical assessment of rocket engine propulsion systems. Advanced nozzle design can address this demand, and has resulted in this investigation of alternate nozzle geometry. A dual-bell nozzle represents a novel approach to this problem by utilizing two theoretically ideal design points over the ascent trajectory instead of just one design point. The primary focus for this project was to investigate the performance of a representative dual-bell nozzle both experimentally and computationally. A procedure to design a dual-bell nozzle was developed and implemented for a representative, nanosatellite launch system. A full-sized conventional nozzle was also designed for the purpose of comparing computational flow and performance characteristics. These nozzle contours were modified to facilitate incorporation into a supersonic wind tunnel through which flow structures were imaged using a schlieren optical system.

The schlieren system was created by Budgen et. al. [27], a Major Qualifying Project (MQP) during the 2012-2013 school year. The system was improved by creating an optical plate to secure the optical elements after an extensive re-calibration process. The dual-bell nozzle fabricated for testing in the wind tunnel had a “first contour” expansion ratio of 1:9.85 corresponding to an ideal design pressure ratio of 134. The downstream, “second contour” had an expansion ratio of 1:19.7 corresponding to an ideal design pressure ratio of 374. The conventional nozzle fabricated for testing in the wind tunnel had an expansion ratio of 1:11.3 corresponding to an ideal design pressure ratio of 102. In addition, the computational fluid dynamics program ANSYS Fluent was used to model both a hypothetical, full-scale nozzle as

well as the scale version tested in the wind tunnel. The dual-bell nozzle was designed for ideal isentropic expansion with an upstream contour area ratio of 1:31.4 and a downstream contour area ratio 1:64.5. These area ratios correspond to a pressure ratio (chamber-to-ambient) of 1000 (for the downstream contour) and 148 (for the upstream contour). By comparison, the conventional nozzle had an area ratio of 11.3. Simulations were performed for the full-scale dual-bell and conventional nozzles operating at pressure ratios (chamber-to-ambient) of 20, 50, 100, 150 and 1000.

The schlieren results were found to match images of the density gradient generated by 2-D Fluent analysis of the contours tested in the wind tunnel. This suggests that the Fluent models are significantly robust, and will predict reasonably accurate results for the cold flow tests modeled for the full-scale nozzles. The method to design the dual-bell nozzle should be refined by future groups to optimize the inflection location, and hence the corresponding design pressure ratios, so as to maximize the average specific impulse over the entire altitude range over which the nozzle is to be used.

## 2 Background

### 2.1 Nozzle Background

A goal of the aerospace engineering community is to develop more efficient and reliable methods to transport payloads into orbit. The demand for higher rocket performance has led to the critical assessment of rocket engine subsystems with the intent of minimizing losses. Numerous studies have focused on the exhaust nozzle, part of the propulsion subsystem on a rocket, with the goal of creating the most efficient single-stage-to-orbit (SSTO) rocket possible. The nozzle's function is to harness energy made available by the combustion of propellant and to turn that energy into thrust.

When propellant is ejected into the combustion chamber and ignited, pressure is created and the only escape for particles is through the nozzle. The nozzle begins as a converging section where the combustion chamber ends. In this converging section, particles are accelerated subsonically until the flow reaches the throat. The throat is the part of the nozzle with the smallest cross-sectional area. In the throat, the flow is "choked"; i.e. the maximum mass flow rate is obtained for given set of upstream conditions. The flow transitions through a Mach number of unity as it passes through the throat. After flowing through the throat, the propellant particles enter the divergent section of the nozzle, which is a focus of modern nozzle study. In this section, the pressurized flow coming out of the throat expands and is accelerated to supersonic velocities as the flow area increases toward the exit plane. Throughout the expansion and acceleration of the exhaust gas in the divergent section of the nozzle the static pressure of the gas decreases. The exit pressure of the exhaust gas is determined by the ratio of the exit area of the nozzle to the throat area. Nozzle efficiency is affected by a number of factors, including viscous losses in the internal boundary layer, flow separation, and flow direction and pressure at



the exit. In an idealized nozzle, maximum efficiency is achieved when the gas is expanded isentropically to exactly the same pressure as the ambient pressure just beyond the exit plane of the nozzle. However, ambient pressure is a function of altitude. Engineers are challenged to design nozzles that enable the exhaust gas to expand perfectly over a range of altitudes.

Conventional nozzles, which refer to any nozzle with a single, continuous contour between the throat and the exit, are designed to be optimally expanded at one mid-range altitude.

Consequently, these nozzles are over-expanded at low altitudes, since they produce an exit pressure less than ambient pressure, and under-expanded at high altitudes, since they produce an exit pressure greater than ambient in these conditions [1].

In the over-expanded case, the exhaust plume separates from the wall inside of the nozzle rather than at the nozzle lip, which occurs at the design altitude. When a nozzle is highly over-expanded, a flow separation phenomenon can occur which creates dangerous side loads. Side loads are caused by the interactions between the boundary layer of the separated flow and internal shocks. Changes in the turbulent velocity profile found in the separated region can result in unsteady shock behavior [1] in which a shock can alternate between free shock separation (FSS) and restricted shock separation (RSS). The transition from FSS to RSS and vice versa can result in sudden changes in the pressure distribution on certain sections of the nozzle wall. These unpredictable lateral forces have the strength to destroy a nozzle [2], and are therefore an important consideration when designing the contour of a nozzle.

In the under-expanded case, the exhaust gas continues to expand after it leaves the nozzle. Unlike over-expansion, under-expansion is not known to produce any dangerous phenomena like side loads. Since energy is released after the gas leaves the nozzle, it cannot be

harnessed and converted to thrust. Thus, under-expansion results in a considerable decrease in engine efficiency at altitudes above the design altitude [3].

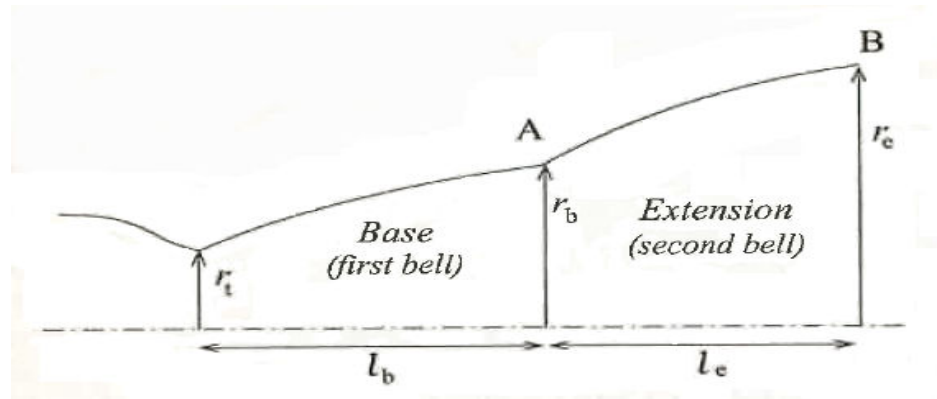


Figure 1: A Dual-Bell Nozzle [Copyright ©Nasuti, F., Onofri, M., & Martelli, E., 2005 [4]]

Dual-bell nozzles have been explored as a possible solution to maximizing efficiency at high altitude while avoiding dangerous side loads at low altitudes. A dual-bell nozzle differs from a conventional nozzle in that it has two distinct contours as opposed to one between the throat and exit. A dual-bell nozzle consists of a base contour that is separated from the extension contour by an inflection in the wall (see Figure 1). The effective cross sectional “exit” area of the base nozzle is the area at the wall inflection. This area can be manipulated such that an effective exit pressure for this section is matched to a relatively low-altitude pressure condition. The inflection acts as a separation point and the separated flow is contained in the additional axisymmetric area given by the extension contour. By controlling the separated flow, side loads can be mitigated at low altitudes. As the rocket’s altitude increases, the flow re-attaches to the wall of the extension due to decreasing ambient pressure. The exit area of the extension section of the nozzle is sized for high altitude operation, thereby reducing efficiency losses due to under-expansion. The dual-bell nozzle is an altitude adaptive nozzle by having a wall inflection that allows one nozzle to be matched to two different ambient pressures [2].

### 2.1.1 Advanced Nozzles

Nozzles constrain the flow of exhaust gases, transforming the energy from an expanding gas traveling at high speeds into thrust. Nozzles can be divided into two primary categories: Thrust Optimized Contour (TOC) and conical contour nozzles. The profile of a conical contour nozzle is defined by the half angle size. The method to create a TOC nozzle starts with the method of characteristics, which produces a bell shaped nozzle that follows streamlines within the flow field of an expanding gas [5]. Throughout the nozzle, the gas follows the contours of the walls, expanding through small expansion waves. However, the rate at which the flow area is increasing decreases throughout the bell curve of the nozzle, which is done in order to ensure a uniform, directed flow field at the exit plane to maximize thrust. The decreasing rate of change of the area causes small compression waves to propagate within the flow in the form of mild oblique shocks. The idealized method of characteristics insures the mutual cancellation of these oblique shock waves and oblique expansion waves, and thereby minimizes the energy loss. Ideal bell-shaped nozzles are impractical because they are usually too long (and therefore too heavy) for most vehicles [5].

Compressed versions of the TOC nozzle, called Truncated Ideal Contour (TIC) nozzles, were designed in order to increase the performance of different vehicles above that produced by a conical contour. The length of these nozzles is specified as a fraction of the length of a conical nozzle with a  $15^\circ$  half angle. A contour can be created once the length is chosen by using methods including the Rao method of characteristics, or by using a Rao parabolic approximation for a bell-shaped contour. The latter is called a Thrust Optimized Parabolic (TOP) nozzle, which increases the thrust potential of a rocket while reducing the length [5].

The Rao method of characteristics uses the method of characteristics to design nozzles. A kernel flow, flow in the initial expansion region of the nozzle, is generated with the method of characteristics for a wide variety of flow angles [1]. Next, the curvature of the throat is defined and a nozzle curve is generated using other given parameters such as the area ratio and the length of the nozzle. The contour is created by picking points on the flow field that result in a smooth, theoretically shockless flow back to the throat. This process is rather complex, and the resulting thrust optimized contour can only be defined by a coordinate list. Rao decided to approximate this contour from the inflection point to the nozzle exit with a parabola.

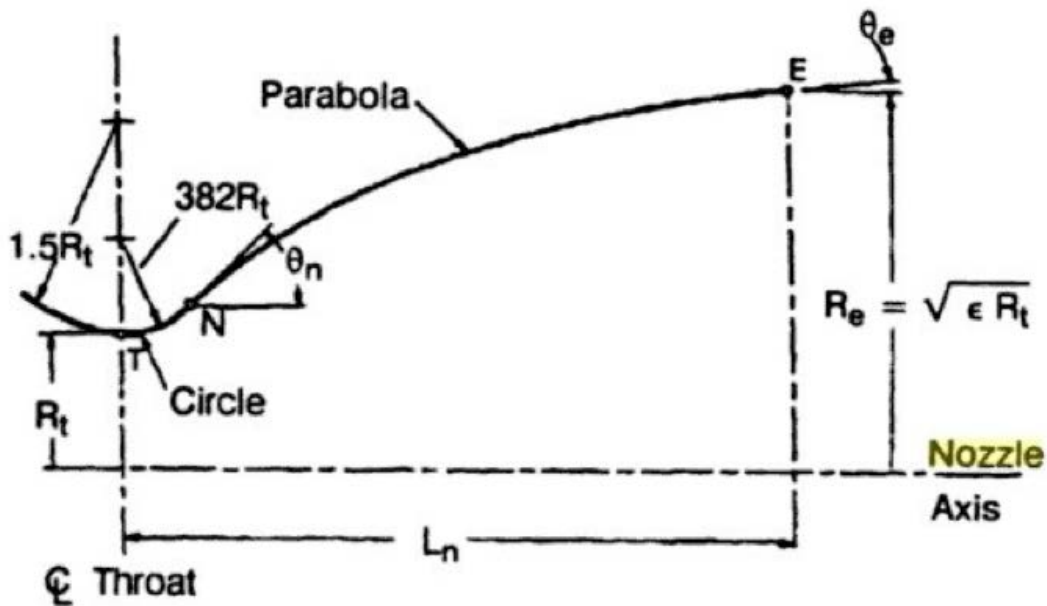


Figure 2: Rao Parabolic Contour [Copyright Kulhanek 2012[6]]

Several problems have been identified with truncated contour nozzles, including a tendency for flow separation to occur when operating at off-design conditions [7]. Flow separation can occur in a TOP nozzle during the startup transient at sea level by the appearance of a shock wave within the nozzle. The shock wave starts at the transition point from the circular curve of the throat to the parabolic curve at the rest of the nozzle [8]. The shockwave within the

nozzle creates free shock separation (FSS) or restricted shock separation (RSS), which causes dangerous side loading on the structure as well as hurting efficiency of the nozzle. In FSS, (Figure 3a), the flow separates completely from the nozzle wall and continues as a free jet; this occurs in over-expanded nozzles [8]. RSS (Figure 3b) causes the flow to separate as well, but it reattaches to the nozzle wall downstream. This creates a separation bubble where a pocket of flow is trapped within the nozzle. RSS is particularly harmful to a rocket due to the generation of side loading from the shock separation and the potential of overheating caused by shockwave interaction with the nozzle wall.

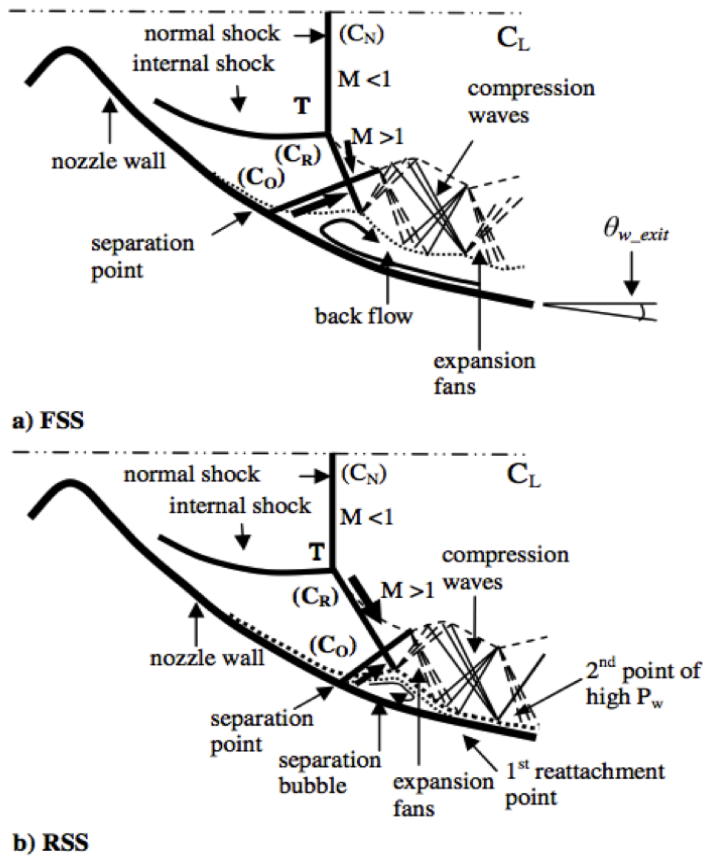


Figure 3: FSS vs. RSS within a conventional nozzle [Copyright © Hagemann and Frey 2008 [8]]

TOC nozzles are commonly used in rocketry and TOP nozzles were used on the Space Shuttle Main Engine and RS-68 engine, and have experienced RSS and FSS during their use [8].

The design of a rocket nozzle is important because it dictates the performance of an engine, which eventually determines the payload. TOP nozzles are a compressed, simplified version of an ideal bell-nozzle created through the method of characteristics and experience FSS and RSS when operating at off-design conditions. Another drawback for all of the different contoured nozzles is that they are optimized for performance at one ambient pressure condition, which correlates with one altitude. A number of altitude compensating nozzle concepts, such as the dual-bell nozzle, have been proposed to achieve better performance over the entire flight of a SSTO rocket.

### **2.1.2 Dual-Bell Nozzle History**

The dual-bell concept was first introduced in literature in 1949 by F. Cowles and C. Foster, and the design was patented in the 1960s by Rocketdyne [9]. Research activity was revived in the 1990s, in part due to the development of modern CFD capabilities. Tests at Rocketdyne conducted by Horn and Fisher and in Europe by the Future European Space Transportation Investigations Programme (FESTIP) at the European Space Agency (ESA) confirmed the feasibility of this nozzle design [9].

Horn and Fisher tested four contour combinations to find the extension contour that provided the most favorable flow transition characteristics and high altitude performance when compared to the performance of two baseline contours. In their testing, a 16:1 expansion ratio Rao optimized contour was used as the base contour for each test nozzle. The extension contours that were tested were selected based on the pressure gradients that were produced, since this gradient affects overall performance as well as flow transition characteristics. They tested conical and Rao contours, which both produce a negative pressure gradient, a “constant pressure” contour that produced no pressure gradient, and an overturned contour, which

produced a positive pressure gradient. They concluded that a constant pressure contour extension provided the most beneficial combination of flow characteristics over the course of a SSTO flight. However, they also demonstrated that real dual-bell nozzles fall short of the theoretical optimum due to losses sustained from aspiration drag, earlier-than-ideal flow separation, and a non-optimal contour for high altitude flight. Even with these additional losses, Horn and Fisher found that a dual-bell nozzle could provide enough thrust to carry 12.1% more payload than a conventional nozzle of the same area ratio [9].

P. Goel and R. Jensen performed the first numerical analysis of dual-bell nozzles, which was published in 1995 [10]. Throughout the 2000s, several numerical and experimental studies of dual-bell nozzles were conducted in the United States and Europe [2]. Modern studies typically focus on optimizing particular design parameters of the dual-bell concept, such as relative length of the extended section [9] and the ideal contour for the extended section [3].

### **2.1.3 Nozzle Comparisons**

Conical contour nozzles are the most simple and, historically, the most commonly used nozzle profile. These nozzles are characterized by a uniform profile from the throat to the exit plane. They are simple in design and the least demanding to manufacture, but they have far from ideal flow characteristics. The flow field is 2-D at the exit plane because of the constant, sloped contour. This reduces the nozzle's overall efficiency because the exhaust gas exits the nozzle with a normal velocity component. In comparison, the exhaust gas in the ideal plume has only an axial velocity component, resulting in an exhaust jet where all the momentum flux produces useful thrust [1].

TIC nozzles are designed to produce a virtually unidirectional exhaust profile. The walls of this contour curve near the throat region, but become nearly straight in the flow direction

towards the exit plane. To fully achieve the goal of unidirectional exhaust flow (i.e. an ideal contour nozzle), the length of the nozzle must be equal to approximately 50 times the radius of the throat. If this length was shortened and the flow forced to straighten out more rapidly, then the exhaust speed of the gas, as well as the overall efficiency, would be lower. While a nozzle of these dimensions would eliminate the losses due to non-axial flow divergence, its weight would be impractical for flight. Thus, the truncated ideal contour nozzle is optimized to provide the most unidirectional flow possible for a given constraint, such as expansion ratio, while constraining the overall size and mass [1].

TOC nozzles are very similar in shape to truncated ideal contour nozzles: they are curved near the throat and become increasingly straight in the flow direction. The main differences are that a thrust optimized contour nozzle is curved more sharply near the throat, which corresponds to a greater initial expansion of the flow, and it has a higher wall angle that turns the flow more suddenly [1].

TOP nozzles are a skewed parabolic approximation of TIC nozzles. A geometric discontinuity where the circular arc of the throat meets the parabolic arc produces an internal shock that increases the wall pressure at the exit plane. The TIC nozzle is slightly more efficient than a TOP nozzle, but the slightly higher wall pressure of the latter at exit offers a significant overall advantage in that it can help avoid destructive side loads that are the result of highly over-expanded nozzles at low altitudes [1].



**Table 1: Comparison of Nozzle Contour Types**

Nozzle Name	Acronym	Key Features
Conical	N/A	Straight walls from throat to exit Incomplete flow turning
Truncated Ideal Contour	TIC	Curved walls near throat transition to nearly straight walls near the exit Virtually complete flow turning Shortened version of the method of characteristics
Thrust Optimized Contour	TOC	Curved walls near throat transition to nearly straight walls near the exit More sudden transition than TIC Virtually complete flow turning
Thrust Optimized Parabolic (Rao)	TOP	Parabolic approximation of TIC Higher wall pressure at exit reduces risk of side loads

A dual-bell nozzle has three characteristic geometric features: an inner base nozzle contour, a wall inflection, and an outer extension nozzle contour. At low altitudes, exhaust gases expand in the base nozzle and separate at the inflection point, making the area at the inflection point the effective exit area during this mode of operation. By having controlled, axisymmetric flow separation, side loads are less of an issue than in conventional nozzles because the separation point cannot fluctuate when the nozzle is under-expanded. As the rocket altitude increases, ambient pressure decreases and the exhaust gases need a larger expansion ratio to match, or approach, the ambient conditions. During this operational phase, the flow is attached to the wall of the extension nozzle, and the whole exit area of the nozzle is used. Because of this second section of the nozzle, the flow is not as under-expanded as it would be for a conventional nozzle with the same area ratio as the base nozzle contour. Thus, the dual-bell nozzle achieves improved high altitude performance over single-bell nozzles [2]. Additionally, dual-bell nozzles

have the unique benefit among altitude compensating nozzles of having no moving parts. The controlled flow separation and mid-flight change in effective exit area is achieved only through the geometry of the wall inflection. The extendable nozzle is another altitude compensating nozzle that, similar to the dual-bell nozzle, uses varying effective exit area to improve flow characteristics over a variety of ambient pressures. Unlike the dual-bell, though, the extendable nozzle utilizes a deployable extension section that is actuated to move down over the base nozzle and form the second contour of a dual-bell-like shape at a specific ambient pressure. The disadvantage of an extendable nozzle is the additional weight and complexity that accompanies the moving section of the nozzle. This makes the dual-bell nozzle a top contender among altitude compensating nozzles because that translates to increased reliability, easier manufacturing, and lower weight [2].

## **2.2 Application**

The dual-bell nozzle for this project is being designed for a cube-satellite (CubeSat) launch vehicle called Nanolaunch 1200. Several NASA centers and the Department of Defense (DoD) as well as eleven universities support the project, which is being overseen by Dr. Jonathon Jones from the Marshall Space Flight Center. The purpose of the Nanolaunch 1200 is to place a 3-U (standard volume) CubeSat into low Earth orbit (LEO) for \$1.2 million, with the goal to bring this cost down to \$250,000 within the next decade [11]. In order to accomplish this goal, the contributors to Nanolaunch are both working together and competing against one another in order to minimize the cost of the launch vehicle. A large part of this process involves using commercial off the shelf (COTS) hardware combined with 3-D printing, also called additive manufacturing. Nanolaunch 1200 is composed of four stages using a Black Brandt sounding rocket for the first stage, a Nihka second stage, and two upper stages which are currently under

development [11]. The dual-bell nozzle in this project is being designed for possible future use on the first stage. The Black Brandt sounding rocket uses the VC Mk 1 motor (Magellan Aerospace/ Bristol Aerospace Ltd. of Canada), has an exit plane diameter of 17 inches, and is 210 inches tall [12]. The motor uses solid propellant, has an average chamber pressure of 1500 psi, and will be fired to propel the vehicle up to 20 km [11].

Nanolaunch 1200 will be valuable for DoD and commercial customers for a number of reasons. The DoD applications mainly involve the need to acquire information or set up a satellite while in a hostile territory. Currently, CubeSats are launched as secondary payloads on large rockets with large and expensive primary missions, and consequently are limited to the main missions' constraints and schedules. Nanolaunch will be useful because CubeSats will not need to wait for an upcoming launch to complete their missions [11]. Commercial customers will benefit from Nanolaunch by receiving affordable access to LEO and having ridesharing constraints removed from the CubeSats. They will be able to have an onboard propulsion system and fewer restrictions as to when and where they launch.

The dual-bell nozzle being designed for this project is a proof of concept design to show that the dual-bell contour can effectively delay flow separation through the flight of the Black Brandt and increase the overall performance of the engine. This nozzle could help Nanolaunch accomplish its goal to reduce costs by improving the specific impulse ( $I_{sp}$ ) of the first stage motor averaged over its ascent trajectory.

## **2.3 Schlieren Imaging**

Schlieren imaging, named after the German word for “streak,” is an optical technique for studying inhomogeneous media. Robert Hooke developed the foundations of this technique in the 17<sup>th</sup> century. It was not until the 19<sup>th</sup> century that the technique was significantly advanced by

J. B. Leon Foucault, who introduced a knife-edge cutoff as part of optical testing. Around the same time, August Toepler reinvented Hooke's technique, introduced the name "schlieren," and made the first major developments of practical apparatus for schlieren imaging. He was also the first to see the motion of shock waves using his schlieren technique. Since then, schlieren techniques have been further developed for various applications, including aeronautical systems development and supersonic flows [13].

### 2.3.1 Optical Principles

Schlieren imaging uses the property that light travels non-uniformly through density-inhomogeneous media to allow one to visualize density gradients in flows. The refractive index for gases is related to density by

$$n - 1 = k\rho \quad 1$$

where  $n$  is the refractive index,  $k$  is the Gladstone-Dale coefficient for the gas, and  $\rho$  is the density of the gas [13]. Since the refractive index changes in proportion to density, the light path is angled away from its original direction based on the density gradient of the media. These deflections are generally small, but can be focused through a lens and made visible to an observer. The ray deflection angle is given by

$$\varepsilon_x = \frac{L}{n_0} \frac{\partial n}{\partial x}, \quad \varepsilon_y = \frac{L}{n_0} \frac{\partial n}{\partial y} \quad 2$$

where  $L$  is the length along the optical axis  $z$  and  $n_0$  is the index of refraction of the surrounding medium. The light is deflected by this angle in both directions (positive and negative) from the original direction. This is for gradients of refraction in the  $x$ - $y$  plane with the  $z$ -axis being the direction of propagation of undisturbed rays [13].

A very simple point source schlieren imaging system consists of a light source, two lenses with a test section between them containing the schlieren object (object of interest for

visualization), a knife edge, and a screen to capture the schlieren image. The first lens collimates the light from the source and the second refocuses the beam onto the screen after the schlieren objects refract the beam. The knife edge is placed at the focus of the second lens. Without the knife edge, every beam of light directed one way would correspond to another one directed exactly opposite, cancelling out the effect. The knife edge blocks half of the beams so that the effect of the refraction can be seen on the screen [13].

### **2.3.2 Applications to Flow Regimes**

In his 1877 experiments to prove that waves from sparks were supersonic, Ernst Mach used schlieren photography, starting a long history of applying schlieren imaging to viewing high-speed phenomena [13]. Schlieren systems are considered the standard for high-speed wind tunnel flow imaging, making it a perfect optical technique for this project. Information about the location and shape of shock waves, the location of boundary-layer separation, and areas of wave interference can be seen qualitatively using a schlieren system. In some circumstances, some quantitative data may be gleaned from schlieren visualizations [13]. In cold-flow testing of scaled-down dual-bell nozzles by Nürnberger-Génin and Stark [14] and Stark et al. [15], schlieren imaging was used to observe the transition behavior and flow evolution between the two nozzle contours. In addition, Stark et al. used schlieren images to determine the transition duration and the angle of tilt of the Mach disk in the nozzle [15].

### 2.3.3 Schlieren vs. Shadowgraph Techniques

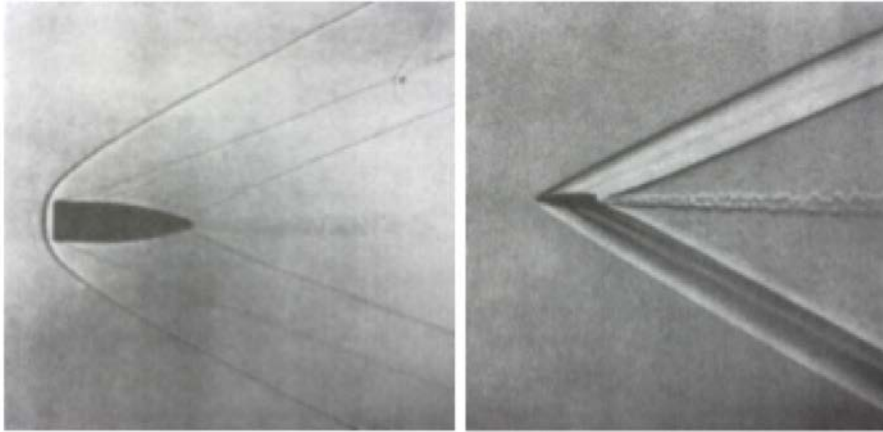


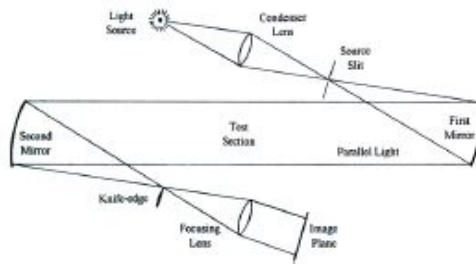
Figure 4: A shadowgram (left) and a schlieren image (right) [Copyright © Settles 2001 [13]]

Shadowgraph imaging is very similar to schlieren imaging and is based on the same principle of refraction through inhomogeneous media. There are several key differences however; most notably, the fact that shadowgrams are just shadows, whereas schlieren images are focused optical images. Shadowgraph methods do not require a knife-edge cutoff, and the apparatus to produce shadowgrams is simpler and easier to use. The light intensity variations in a schlieren image represent the light deflection angle, while in a shadowgram ray displacement due to the deflection angle causes the light intensity variations (Figure 4).

Shadowgrams are generally less sensitive to smaller density gradients than schlieren images, but are useful when visualizing turbulent flows and shock waves. However, when the disturbances are weaker overall, schlieren images accentuate detail of the flow around the schlieren object and have the added benefit of a one-to-one ratio between image size and object size [13].

### 2.3.4 Schlieren System Types

The simple point light source schlieren system discussed above under Optical Principles (2.3.1) is an example of a simple-lens type system. In addition, there are various lens-and-mirror type systems and a variety of large-field systems.



**Figure 5: Conventional Z-type system [Copyright © Settles 2001 [13]]**

In the historical development of schlieren systems, lens-and-mirror systems were developed after the success of Foucault's knife-edge experiments. The most popular of these systems is the Z-type system, which employs two mirrors that are tilted in opposite directions. The schlieren object lies between the two mirrors (Figure 5). One of the advantages of this type of system is that having a larger than the mathematically required minimum distance between the two mirrors to accommodate the test section does not affect the image; therefore the optical system will not constrain the test section size. In addition, when set up correctly, the two mirrors cancel out some aberration effects. Other mirror-lens systems include the single-mirror coincident system, the off-axis single-mirror system, and multi-pass systems [13].

## 2.4 Computational Fluid Dynamics

### 2.4.1 Flow Regimes

When performing fluid analyses, flows can be separated into three categories: subsonic, transonic, and supersonic (and in some cases, hypersonic as well). At lower velocities (below Mach 0.7) fluids are conventionally taken to be incompressible as they flow through a channel. As flow speed increases, however, compressibility effects must be considered. Gases can have very large density fluctuations in supersonic flow due to their molecular structure.

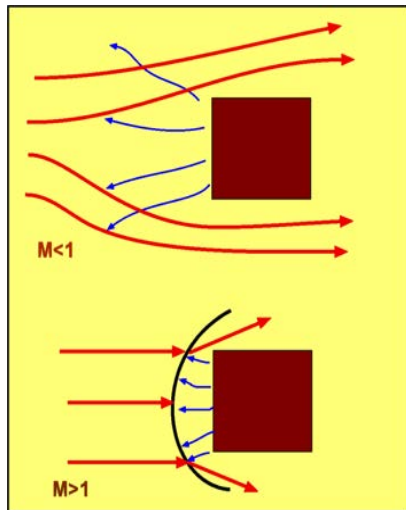


Figure 6: A body placed in incompressible and compressible flow [Copyright © Auld and Srinivas 2006 [16]]

Compressible flows have varying densities. Calculations for compressible regimes are more complex than for incompressible regimes due to density changes, disturbances, shock waves, and expansion fans. This can be seen in Figure 6 as a shock wave forms in front of the disturbance within the supersonic flow. The shockwave results in a different velocity profile after the shock than would exist if the shock did not form. When a supersonic, compressible flow approaches an obstacle, a shock wave forms, resulting in significant changes in the flow properties over very short distances (Figure 6).



## 2.4.2 Turbulence Models

Turbulent flows are unpredictable and difficult to model accurately. Figure 7 shows the differences in boundary layer flow behavior for subsonic and supersonic conditions. While laminar flow along a boundary layer can be considered uniform, turbulent flow behaves erratically in the boundary layer. Computational turbulence models allow for appropriate estimations of these flows, which is important for high-speed applications. These are models that capture the viscous boundary layer by approximately describing the velocity profile.

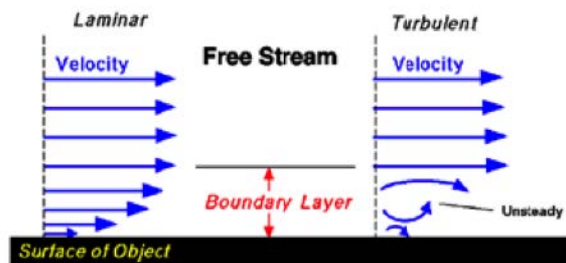


Figure 7: Flow near boundary layer for laminar and turbulent flow [Copyright © NASA Glenn Research center 2000 [17]]

The most common models for aerospace applications are Reynolds-averaged Navier-Stokes (RANS) and Large Eddy Simulation models, which are named for their governing equations. These models are separated into subgroups based on the number of transport equations needed to compute the model [18].

Algebraic or Zero-Equation models are typically no longer used as they rely only on the Navier-Stokes equations. Without the use of additional transport equations, these models are oversimplified for complex geometries. These simpler equations normally do not suffice, but when they are appropriate produce accurate results [18]. One-Equation models require one transport equation to be solved to model the turbulent viscosity. The Goldberg, Baldwin-Barth,

and Spalart-Allmaras are included in this group. Of these, the Spalart-Allmaras is the most commonly used [19].

Two-Equation models require an additional transport equation, but result in more accurate flow models. The most popular two-equation models are the  $\kappa$ -epsilon,  $\kappa$ -omega, and Menter Shear Stress Transport (SST), a combination of the previous two equations [17]. The  $\kappa$ -epsilon model is considered to more accurate in regions farther from walls, while the  $\kappa$ -omega model is typically used along boundary surfaces [19].

Turbulence models are selected based on the complexity of the flow field and the regions of most concern within the flow. For most supersonic flows, these regions are the inlet, outlet, hard surfaces, and/or contours.

### **2.4.3 FEM vs. FVM**

For computer simulation of flows, there are two primary numerical methods used to model fluid mechanics: the Finite Element Method (FEM) and the Finite Volume Method (FVM). For this project, FVM is the better method, as outlined below.

FEM is more commonly used in analysis of solids, but certain Computational Fluid Dynamics (CFD) programs do use FEM, such as COMSOL Multiphysics [20]. Analysis using FEM begins with the definition of a boundary condition problem, created by the researcher. Next, the researcher, with the assistance of a computer program, creates a mesh by dividing the area in question into sub-regions. The solver then analyzes the flow over each element individually. However, each boundary between cells is consistent, which allows the program to combine the results into a contiguous whole. This process is extremely expensive in terms of computing power, as it requires many iterations and a very large number of equations [21]. However, it is possible to model the mesh in a way to reduce the number of equations needed if

high precision is not required [22]. FEM tends to be better suited for either solid modeling or modeling in multiple physical models, such as a problem with large non-linear deformation of a flexible element in a flow field or modeling fluid flows with electrical interaction.

FVM is the most commonly used numerical method for boundary condition problems. One key difference between FEM and FVM is that the flux between elements in FVM is conserved. This makes calculations involving flux (such as many fluid dynamics problems) much easier to handle. The basic process of solving a problem using FVM begins with meshing. Each of these cells is treated as a separate control volume and a set of conservation equations is applied to the flow for that specific cell. These equations are then broken down into algebraic expressions, which can then be solved by a computer program [22].

Having a clear problem statement is crucial to obtaining accurate and consistent results while using either of these methods. Both methods are only useful if the results can be interpreted, which is why most CFD programs have a post-processing visualization tool [22]. In addition, it is possible to solve physically impossible problems with a CFD solver returning physically impossible results. Great care must be taken with any results from a computer program to ensure that they reflect reality.

#### **2.4.4 Turbulence Model Comparisons**

Turbulence is the bane of CFD modeling and of fluid dynamics in general. It is nonlinear and resists linearization in complex flows, leading to chaotic solutions and suboptimal estimations. Despite these difficulties, various models for turbulence have been developed with varying degrees of success. As already mentioned in Section 2.4.3, there are four primary options: the Reynolds Average Navier-Stokes Equations (RANS), Large Eddy Simulation (LES),

Detached Eddy Simulation (DES), and Direct Numerical Simulation (DNS). This project used RANS, detailed in this section.

Direct Numerical Simulation (DNS) directly solves the Navier-Stokes equations for turbulence at all scales [23]. This method is possibly the most accurate model of reality at the cost of extreme complexity. As the Reynolds number increases, the number of equations and computational memory needed rises rapidly. This means that for complex geometries, this method cannot be used within a reasonable timeframe [23]. For these reasons, DNS is not a method that is feasible for primary use in this project.

Large Eddy Simulation (LES) is a simpler method for modeling turbulence than DNS and as such is more widely used. The basic process of LES is the filtering of the Navier-Stokes equations using a low-pass filter [24]. The low-pass filter removes the smallest equations from consideration, greatly simplifying the problem. An accurate simulation for turbulence can be developed in a reasonable amount of time while still returning results that reflect the turbulent flow on a large scale. While this method uses fewer computer resources than DNS, it is still a computer-intensive process that requires further modeling beyond the initial meshing, as each mesh region is broken into smaller regions. Considering this complexity, LES is not the ideal method for this project.

Detached Eddy Simulation (DES) is closely related to LES and RANS: in fact, it can be loosely described as a hybrid of the two systems. In areas where more detail is needed, a method closely resembling LES is used; however, in areas where LES is either not needed or not useable, RANS is used. Effectively, DES is the best of both methods, but this again comes with a large drawback: computational complexity. According to Spalart, a full simulation of a complex body,

such as an aircraft, would require in excess of  $10^{11}$  grid points [25]. This project is limited to less than  $10^7$  grid points in Fluent and as such, DES is beyond the computational resources available.

The precursor and basic model for all of these methods is RANS. For this method, which was first developed in 1883 by Osborne Reynolds [26], the unsteady terms in the Navier-Stokes equations are averaged out. This greatly simplifies the equations and allows them to be solved without a CFD solver. It is possible (if impractical) to solve these equations by hand, given enough time. For this reason, RANS is the best fit for this project. However, there may be certain scenarios where a more detailed solution is required. In these cases, one of the other methods can be used for that specific region, similar to how DES operates. For example, the inflection point and surrounding flow pattern may need a more detailed model of the turbulence for a realistic flow.

**Table 2: Comparison of Turbulence Modeling Systems**

Turbulence Models	Advantages	Disadvantages
DNS	Most detailed system	Extremely complex Very slow
LES	Faster than DNS	Computationally complex
DES	Adjustable	Computationally impractical
RANS	Can be solved by hand	Least amount of details

### **3 Methodology**

The primary focus for this project was testing a dual-bell contour in the supersonic wind tunnel and testing a hypothetical full-scale nozzle using Fluent. These results were then compared to a similar conventional nozzle for each case. In addition, Fluent was used to simulate the flow through the supersonic wind tunnel in order to assess the comparability of Fluent results and wind tunnel results.

#### **3.1 Supersonic Wind Tunnel**

Several previous MQP groups contributed to the development and construction of the supersonic wind tunnel that was used for the project. Three MQP groups between 2009 and 2013 contributed to the design of the wind tunnel, the current version of which was completed during the 2012-2013 academic year. The wind tunnel is an intermittent indraft tunnel. To operate it, the vacuum chamber to which it is attached is pumped down to approximately 50 milliTorr. When the valve that isolates the system from the atmosphere is opened, the vacuum chamber draws in ambient air through the wind tunnel core. The pressure gradient between the near-vacuum conditions on one end of the tunnel and ambient conditions on the other, in combination with the geometry of the tunnel, is sufficient to produce a supersonic Mach number in the test section [27].

The wind tunnel has three components in addition to an air drier. The flange assembly connects the core to the vacuum chamber and supports the weight of the whole system. The core contains the test section, with the geometry necessary to produce a supersonic flow. This section consists of upper and lower contours placed opposite each other and two sheets of clear acrylic that serve as windows into the test section. The contours in the test section are intended to

approximate a 2-D flow. The final component is the valve assembly, which seals the system from the atmosphere. These three components were designed to be modular [27]. Thus, the original core, which was designed to produce a flow with a specific Mach number, can be removed and replaced with another core possessing the desired geometry for the test of interest. For this project, the cores replicate the cross-sections of a dual-bell nozzle and of a conventional TOP nozzle.

### 3.2 Schlieren System

The Design and Construction of a Supersonic Wind Tunnel with Diagnostics MQP [27] designed a schlieren system to visualize the density gradients in their wind tunnel test section. Their setup has been adapted for use in visualizing the density gradients of flow through 2-D approximations of various conventional and dual-bell nozzle contours for this project. They chose and constructed a conventional z-type system for their project which consists of a light source, a condenser lens, a slit, two mirrors, a focusing lens, a knife edge, and a screen (Figure 8) [27].

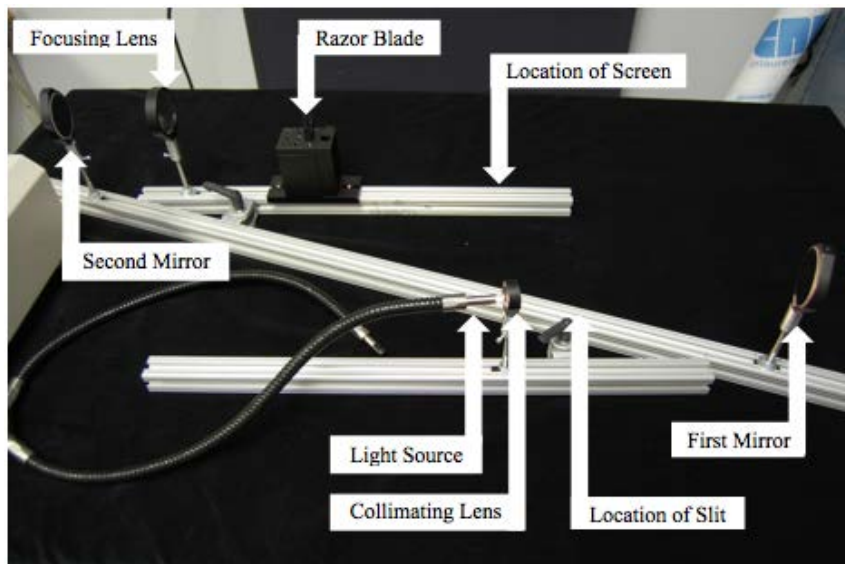


Figure 8: Existing Schlieren setup.

The light source has an adjustable goose-neck support enabling the light to be easily directed towards the condenser lens. It also has a knob to control the light's intensity. The condenser lens serves to collect what ambient light cannot be eliminated as well as light from the light source and distribute it evenly through the rest of the system. The slit, which is 0.36" by 0.072", is oriented vertically to work with a horizontally mounted knife edge. The two mirrors have focal lengths of 200mm, which is sufficiently less than the design distance between them, which prevents them from interfering with each other. The focusing lens, placed within the focal length of the second mirror, reduces the resulting image to a smaller area without compromising its quality. The knife-edge is mounted horizontally on a vernier stage for fine adjustments of its position to adjust image contrast. The screen consists of photo paper held flat on a mounted clipboard. The components of the z-system are discussed by Bugden et al. in Design and Construction of a Supersonic Wind Tunnel with Diagnostics [27].

One of the key advantages of the schlieren setup is its independence from the wind tunnel and vacuum chamber assembly. The schlieren system relies on precise alignment of mirrors and lenses, so it is mounted separately from the wind tunnel and vacuum chamber to minimize potential vibrational effects. The schlieren system is mounted on a custom table constructed of x-channel; two acrylic shelves hold the z-system setup and the light source, and adjustable feet account for floor irregularities [27].

The z-system itself is composed of three pieces of x-channel held together by adjustable locking hinges. The mirrors are mounted on the center piece of x-channel. One side piece holds the condenser lens, and the other holds the focusing lens, knife edge, and screen. Bugden et al. [27] finalized the distance between the two mirrors and the angle of the side x-channels to the



center piece through an optimization process. The final parameters chosen were  $15^\circ$  angles for each of the side rails and a distance of 800mm between the mirrors [27].

Furthermore, Bugden et al. [27] developed a detailed set-up and alignment procedure for use during testing. This reduced the learning curve for using the system with this project.

Adapting the z-system to this MQP was relatively simple. The test sections manufactured for this project are the same dimensions as the ones used last year, so the system does not need to be re-optimized [27].

### **3.3 COMSOL vs. Fluent**

COMSOL and Fluent are two tools that were considered for possible use with the CFD portion of the project. Both are powerful tools for simulation but have different characteristics. Fluent works within the ANSYS (ANSYS, Inc., Canonsburg, PA) simulation software package whereas COMSOL Multiphysics contains a CFD software package. Both can import CAD geometries, and both are able to generate a mesh from the drawings. COMSOL uses finite element discretization [28], which can increase computational time, whereas Fluent uses a finite volume scheme. Both solvers have a variety of turbulence models including the  $\kappa$ - $\epsilon$  and shear stress turbulence models. Georgescu et al. [20] compared the computational fluid dynamics solvers by using both Fluent and COMSOL to model flow over a NACA airfoil. The flow domain contained an equal number of nodes, but due to the difference between finite volume and finite elements, the number of cells was different between the two cases. The case that ran with COMSOL took over 10 hours to converge, whereas Fluent took less than 25 minutes. The results of the study showed that both tools produce similar results, Fluent, however, took less time to converge. S. Kulhanek [6] designed a conventional Rao nozzle contour then modeled its

performance using Fluent. This provided a baseline contour type to use for the baseline nozzle comparison for this project.

Fluent was chosen as the CFD tool used to model the dual-bell nozzle because it is based on a finite volume discretization scheme, which will help minimize computational time as well as capture supersonic flow features such as shockwaves. COMSOL is able to model shockwaves, however, it has a tendency to attempt to smooth them out and blend their effects into the surrounding flow. Fluent uses a two- equation model for turbulent flow based on the shear stress turbulence [22]. This model effectively captures the characteristics of boundary layer flows and separated flows; examining both is the primary focus of this project. Fluent also uses a several scale resolving turbulence models including large eddy and detached eddy simulations (LES and DES respectively). Furthermore, the embedded-LES option (E-LES) enables computation of the LES solution in selected subdomains within unsteady flows and can be coupled with a Reynolds averaged Navier-Stokes model. This form of coupling further decreases computational time while still capturing key flow features.

### **3.4 Thrust Optimized Parabolic Contours**

A TOP nozzle is constructed using three curves (Figure 9): an initial, large circle coming from the combustion chamber to the throat, a smaller circle exiting the throat, and a parabola to extend the approximated bell contour to the exit plane.

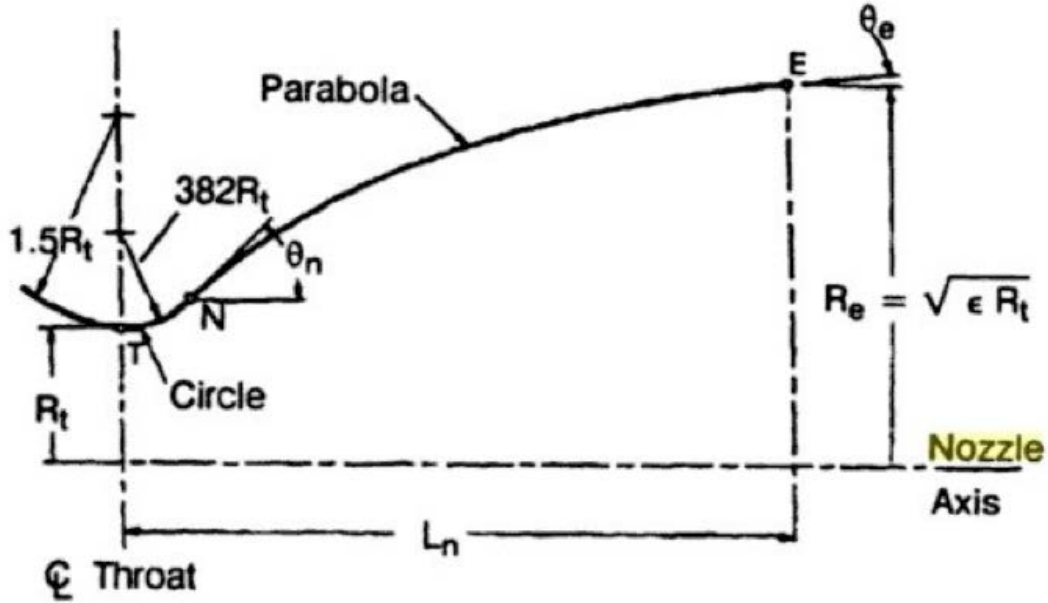


Figure 9: TOP nozzle based on Rao's approximation [Copyright © Kulhanek, 2012 [6]].

A TOP nozzle, using Rao coefficients to define the circular curves entering and exiting the throat, equal to  $1.5R_t$  and  $0.382R_t$ , was used as a baseline nozzle for this project [6]. The curves were modeled using MATLAB (MathWorks, Natick, MA) using the back- and chamber pressures for Nanolaunch 1200 and to facilitate practical implementation of the nozzle in the wind tunnel used to test the dual-bell nozzle [11].

The Rao parabolic nozzle is defined by three curves, the length of the nozzle, and the throat radius. The length of the nozzle is determined by

$$L_n = \frac{K(\sqrt{\epsilon}-1)R_t}{\tan(\theta_e)} \quad 3$$

where  $K$  is a value chosen based on the percent of the length of a conical nozzle with a  $15^\circ$  half angle, the flow deflection angle at the exit,  $\theta_e$ , and the throat radius,  $R_t$ . In order to define the nozzle further, a coordinate system is defined with the axial ( $x$ ) axis passing through the line of symmetry and the radial ( $y$ ) axis going through the center of the throat. The first and second

curves define the entrance and exit of the throat of the nozzle, and are based on circular curves.

The first curve into the nozzle is determined by the equation:

$$x^2 + (y - (R_t + 1.5R_t))^2 = (1.5R_t)^2 \quad 4$$

which can then be solved for y. Note the curve is defining the bottom half of the circle, and therefore is negative.

$$y = -\sqrt{(1.5R_t)^2 - x^2} + 2.5R_t \quad 5$$

The second curve begins at the throat where the derivative of both curves is equal to zero.

The second curve is also a circle defined by the equation:

$$x^2 + (y - (R_t + 0.382R_t))^2 = (0.382R_t)^2 \quad 6$$

which leads to the equation for the second circle:

$$y = -\sqrt{(0.382R_t)^2 - x^2} + 1.382R_t \quad 7$$

In order to ensure a smooth transition from the combustion chamber to the throat, there needs to be continuity between the curve defining the combustion chamber and the entrance to the throat. That is, the derivative for both points needs to be equal:

$$\frac{dy}{dx} = \tan(\theta_1) = \frac{x_1}{\sqrt{(1.5R_t)^2 - x_1^2}} \quad 8$$

where  $\theta_1$  is the angle at the start of the curve ( $x = -0.0184$  m), and  $x_1$  is a function of the throat radius and  $\theta_1$ .

The curve leading from the combustion chamber to the throat curvature begins at  $x_1$ , which equals:

$$x_1 = -1.5R_t \sin(\theta_1) \quad 9$$

The equation of the parabola, curve 3, takes the form

$$x = ay^2 + by + c \quad 10$$

and the coefficients are determined by the derivatives at the point where the circle from the throat meets the beginning of the parabola,  $x_N$ , and the length of the nozzle. To determine  $x_N$ , the angle,  $\theta_N$  needs to be defined, then the derivative of the second curve should be equal to its tangent.

$$\frac{dy}{dx} = \tan(\theta_N) = \frac{x_N}{\sqrt{(0.382R_t)^2 - x^2}} \quad 11$$

This is then solved for  $x_N$ .

$$x_N = 0.382R_t \sin(\theta_N) \quad 12$$

At  $x_N$ , both the derivatives for the parabola and the circle have to be the same and both have to meet. This leads to the following constraints for the coefficients of the parabola.

$$x_N = aR_N^2 + bR_n + c \quad 13$$

$$\frac{dy}{dx} = \tan(\theta_N) = \frac{1}{2aR_N + b} \quad 14$$

To complete the series of equations the exit of the nozzle is examined, where  $x$  is equal to the nozzle's length,  $L_n$ . Ideally, the flow should have been turned as close as possible to horizontal by the exit plane, and the derivative of the parabola evaluated at  $L_n$  is used.

$$\frac{dy}{dx} = \tan(\theta_e) = \frac{1}{2aR_e + b} \quad 15$$

This completes the linear system of equations. In matrix form, the system is

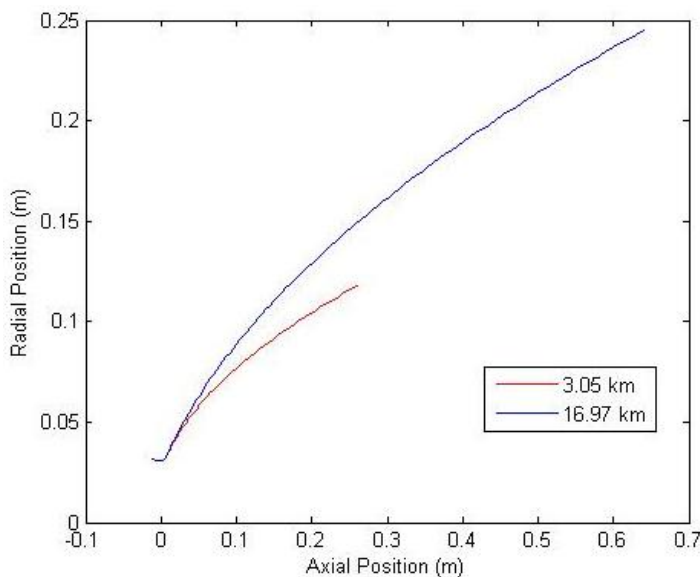
$$\begin{bmatrix} 2R_N & 1 & 0 \\ 2R_e & 1 & 0 \\ R_N^2 & R_N & 1 \end{bmatrix} \begin{bmatrix} a \\ b \\ c \end{bmatrix} = \begin{bmatrix} \frac{1}{\tan(\theta_N)} \\ \frac{1}{\tan(\theta_e)} \\ x_N \end{bmatrix} \quad 16$$

which can then be solved for the coefficients.

### 3.5 Dual-Bell Nozzle Design

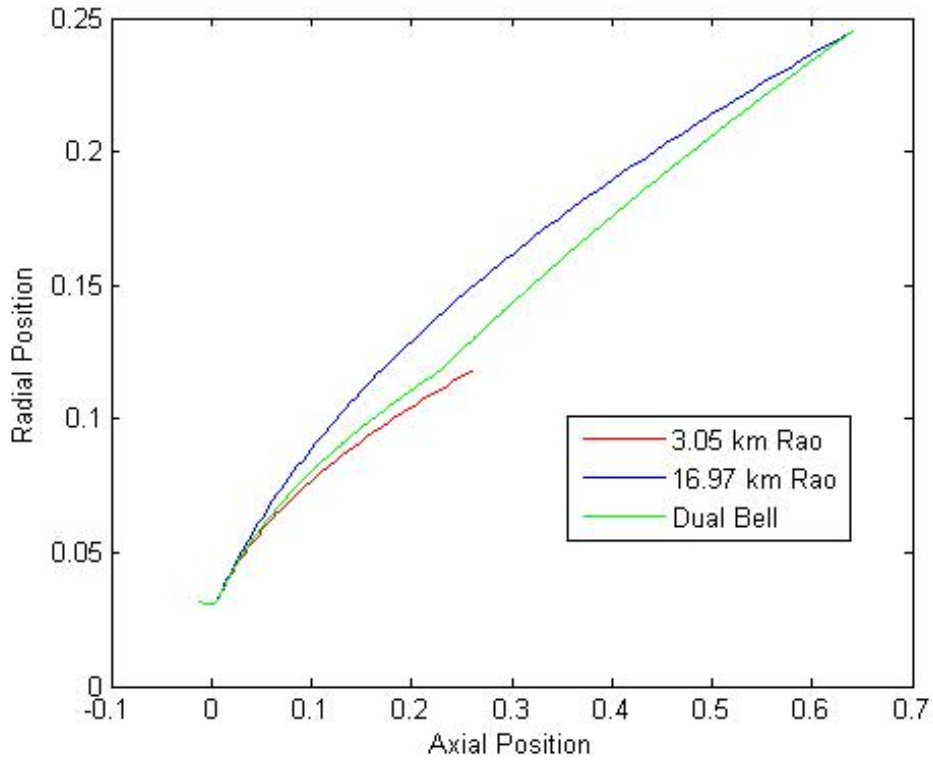
The dual-bell contour design adds a fourth curve to the conventional Rao design by adding a second parabola to connect two Rao that share the same throat area, but are optimized for different altitudes. The second parabola defines the second bell section and connects the two contours thereby achieving a greater expansion ratio.

The dual-bell nozzle was defined similarly to the contour of the Rao nozzle, with the same throat entrance and exit parameters as defined in equations 10 and 12. The parabola coefficients for the first parabola were found using the same method as the Rao contour. Figure 10 shows a Rao nozzle contour optimized for two different altitudes (3.05 km and 16.97 km), corresponding to two different ambient pressures (10.1 psi and 1.5 psi).



**Figure 10: Rao Contours for different altitudes**

A dual-bell nozzle connecting the two Rao nozzles, with an optimized design point for altitudes of 3.05 km and 16.7 km is shown in Figure 11.



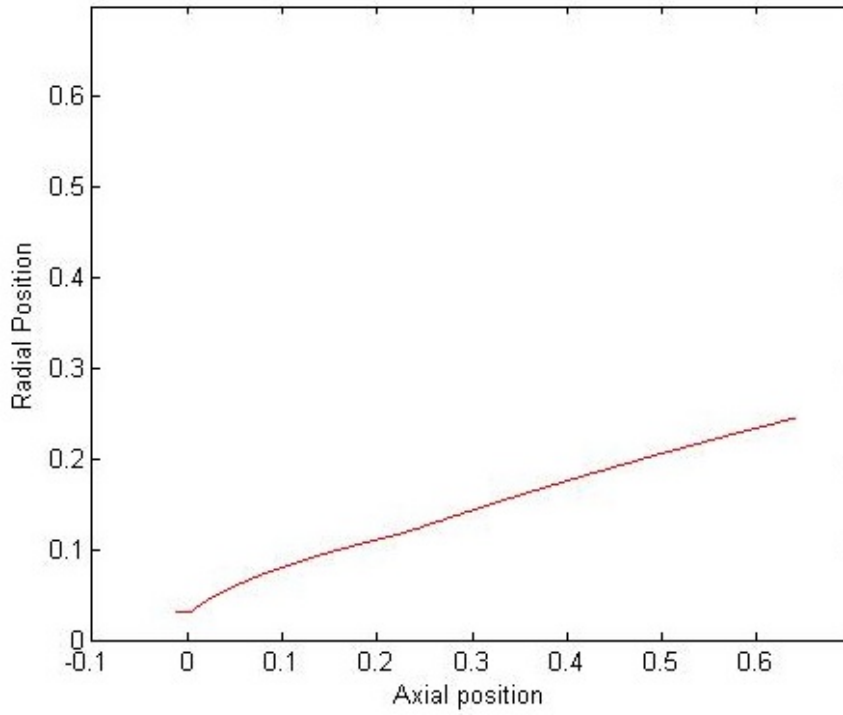
**Figure 11: Dual-bell contour connecting two Rao contours designed for different ambient pressures**

The coefficients of the second parabola were found using the inflection point,  $x=x_M$ , the inflection angle,  $\theta_M$  and the exit angle,  $\theta_e$ . As shown in Figure 11, the distance at  $x_m$  is the distance to the inflection point, and was defined using

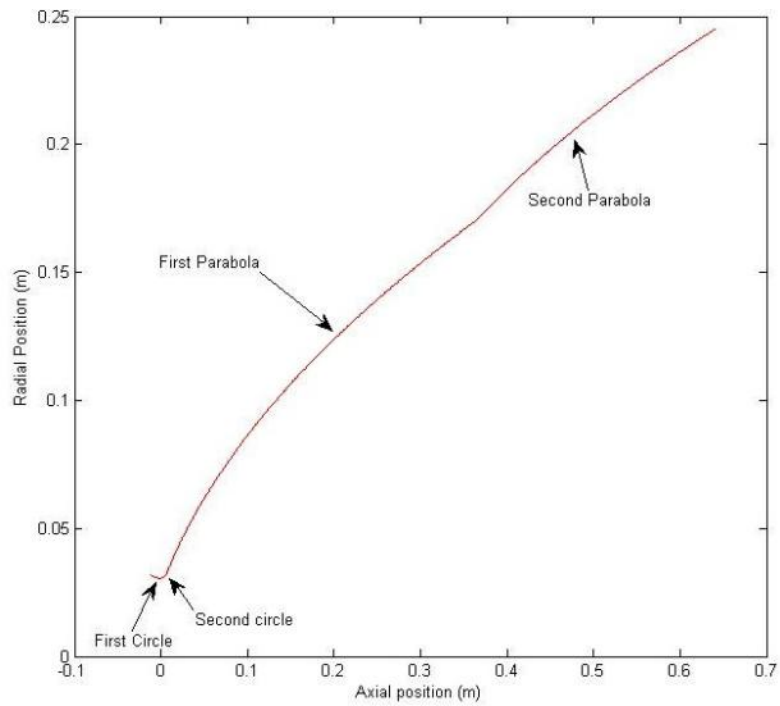
$$L_M = \frac{K_M(\sqrt{\varepsilon}-1)R_t}{\tan(\theta_e)} \quad 17$$

where the K value  $K_M$  was reduced to 0.7 in order to keep the overall nozzle a reasonable length.

Figure 12 shows a normalized dual-bell contour. It has equal sized axes in order to better represent the actual nozzle's shape.



**Figure 12: Dual-bell nozzle with normalized axes**



**Figure 13: Dual-bell nozzle with labeled sections (axes scaled for clarity)**



A parabola defines the second curve, and the coefficients were solved for using the same derivative method used to make the first curve and the Rao contour. The system of equations to solve for the coefficients of the second curve is:

$$\begin{bmatrix} 2R_M & 1 & 0 \\ 2R_e & 1 & 0 \\ R_N^2 & R_N & 1 \end{bmatrix} \begin{bmatrix} a' \\ b' \\ c' \end{bmatrix} = \begin{bmatrix} \frac{1}{\tan(\theta_M)} \\ \frac{1}{\tan(\theta_e)} \\ x_M \end{bmatrix} \quad 18$$

where  $a'$ ,  $b'$  and  $c'$  are the coefficients of the second curve. The full system definition is provided in Appendix D.

## **4 Experimental Procedures**

### **4.1 Setup and Experiments**

#### **4.1.1 Alignment and Focusing**

The eight components of the schlieren system must be in specific locations with respect to the other components in order to use it (Figure 8). The components are arranged in three segments of the z-type system. The first segment begins at the light source, includes the collimating lens and the slit, and ends at the first mirror. The second segment extends from the first mirror to the second mirror, and is referred to as the test section of the schlieren system. The third segment begins at the second mirror, includes the razor blade and the focusing lens, and ends at the screen.

In order to obtain the best possible schlieren images, the components of the system must be aligned very precisely. A good image should be circular in shape (if the mirrors are circular), focused, and it should exhibit high contrast without being too dark. The location and orientation of all of the components contribute to having a sufficiently bright image, but the slit has the most direct effect. Placing the slit closer to the collimating lens increases the amount of light that passes through it, and placing it further away from the collimating lens reduces this amount of light. Ideally, the light beam that passes through the slit should be the same diameter as the first mirror to maximize the brightness of the image while reducing light pollution.

The focus of the image is largely controlled by the focusing lens, which is the last optical component that the light beam passes through before being projected on the screen. Ideally, this lens should capture all of the light that passes by the razor blade. Thus, the optimal place for the focusing lens is after the razor blade and anywhere within two focal lengths of the second mirror.

If this lens is placed further than two times the focal length of the second mirror, then light would be directed onto the screen without being focused. This results in an unfocused image as well as significant light pollution.

Finally, having high contrast is critical to obtaining useful images, and this quality is largely controlled by the height of the razor blade. The focused light beam takes the shape of the vertical slit that it passed through in the first segment, and thus the horizontal razor blade is ideal for cutting off a portion of the light beam. The higher the razor blade, the more of the light beam (which consists of both parallel and refracted light) gets cut off. The effect of this is that the highest contrast images are also very dark, so a middle ground between brightness and contrast must be determined while adjusting the height of the razor blade.

#### **4.1.2 Updates to Existing Schlieren System**

In order to obtain the best possible schlieren results, significant changes were made to the existing schlieren system. The first change that was made was to add ball and socket mounts to both mirrors between the mirror mount and the conversion piece that connects to the post. This change allowed for easier alignment of the surfaces of the two mirrors with one another. However, these mounts on the mirrors necessitated machining new posts for all of the components to account for the height added to the mirrors and to keep the focal points of all components on the same plane. The posts were made out of 4-inch long steel bolts that were machined to the proper size using a lathe.

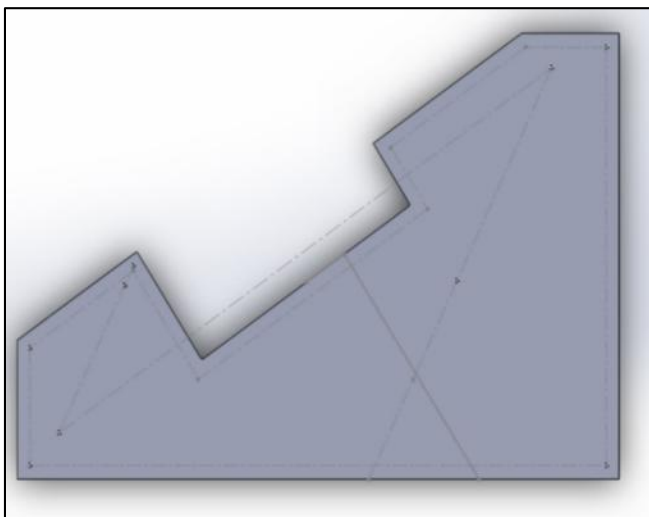
Next, specific components had to be improved. A bracket was machined to hold the light source gooseneck in a specific location. The bracket is a cylindrical piece of aluminum with a hole bored out along its length such that the end of the gooseneck can be inserted into the bracket and then secured using a setscrew. The bracket is held up to the appropriate height by a threaded

aluminum post. By securing the light source, the proper alignment is much easier to achieve and the system is much more resilient to minor disturbances than it was when the gooseneck was a freestanding component.

The screen and the slit elements of the system also required improvement. These components were originally made of materials that were not ideal for this application, so new parts were made using opaque, white acrylic. Both the screen and slit were designed to be freestanding so that their positions can be individually optimized based on the final alignment. For the screen, the acrylic was sanded with a fine grit sandpaper to get a matte finish. This is ideal because light pollution could reflect off a glossy screen and interfere with the image captured by the camera. For the slit, the small section of a metal eraser shield previously used was kept, but it was mounted on a piece of acrylic rather than construction paper so that the only light that passes this component passes through the slit.

The system has an optimal alignment, and once that alignment is achieved, there is no advantage to the ability to move individual components and having movable components puts the system at risk for being misaligned in the future. Therefore it was determined that the system would have to be removed from the original x-channel base and reconfigured using a solid aluminum plate as the base. This decision was based on the difficulty of achieving a proper alignment on the x-channel base. Once all of the new components were incorporated into the system, the three segments of x-channel were detached from each other so that a new optimization exercise could be carried out to determine the ideal distances and angles in the system. This optimization exercise is detailed below in the Section 4.1.3, “Optimization and Specific Setup.” After the alignment was optimized, the distances between components and the angles between segments were used to design the optical plate.

The optical plate is a complex shape that was machined from a 36" x 24" x 1/4" plate of aluminum. The geometry is a result of the alignment needed to obtain a schlieren image and the physical constraints of the wind tunnel and vacuum chamber. The design for the layout of the holes was made using SolidWorks (Dassault Systemes SolidWorks Corporation, Waltham, MA) computer aided design software. Only holes for the posts that hold the light source gooseneck, collimating lens, the two mirrors, and the focusing lens were machined into the plate. It was determined that keeping the slit, razor blade, and screen free-standing would allow for finer adjustment of the most sensitive component locations. Additionally, holes were placed at the corners of the optical plate so that it could be raised or lowered as needed for use with the wind tunnel. All the holes are size 1/4"-20. After the SolidWorks design was complete, it was converted into a design that could be read and produced by a machine using Esprit computer aided machining software. Finally, the optical plate was manufactured using a CNC milling machine located in the WPI Washburn shop. The plate did not fit on the schlieren table that was produced by a previous MQP group, but a suitably larger table was found.



**Figure 14: Solid model of optical plate**

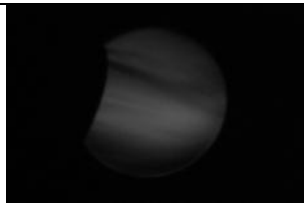
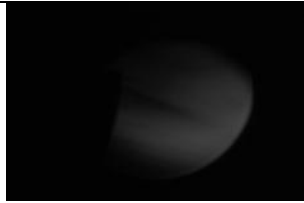
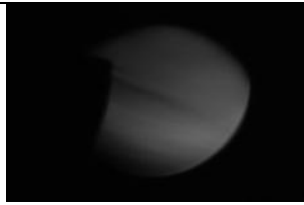
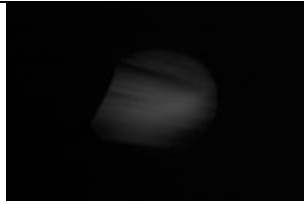
### 4.1.3 Optimization and Specific Setup


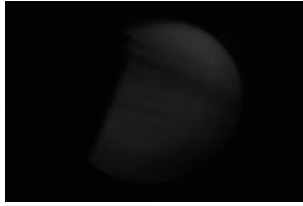
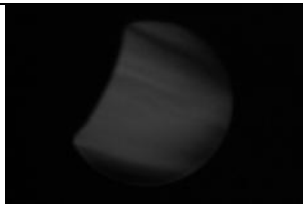
The first step to optimizing the system alignment was to align the two parallel segments of the z-system. For the first of these, the segment with the light source, the components were adjusted to concentrate the light hitting the first mirror. This both channels as much light as possible through the test section (resulting in brighter images), and reduces light pollution. For the other parallel segment, the section with the screen, the adjustments focused around the razor blade, as its position needs to be precise in order to produce a schlieren image. The razor is placed just behind the second mirror's focal point and raised up so that it cuts off more than half of the light beam. After the razor was positioned, the focusing lens was adjusted such that all of the light that passes the razor blade is captured within the lens. Finally, the screen was adjusted along the optical axis with respect to the focusing lens until a clear image appeared.

After the lengths of the parallel segments of the system were determined, the length of the second segment (the test section) as well as the angle between the segments was varied so as to maximize image quality. To determine the best arrangement, an optimization experiment was conducted. Test section lengths of 80 cm, 90 cm, and 100 cm were tested, as well as angles of 15°, 20°, 30°, and 40°. Certain configurations were eliminated because they did not allot enough physical space for the wind tunnel, which at its widest requires at least 12 cm of space in the second segment without interfering with the components in either the first or third segments.

Table 3 summarizes the results obtained by imaging a heat gun using a number of different configurations which vary the test section length and angle while keeping the test section normal to the wind tunnel.

**Table 3: Summary of Results from Optimization Exercise**

Trial	Test Section Length (cm)	Angle (°)	Space for Wind Tunnel Width (cm)	Photographic Results	Comments
1	80	15	9.49	N/A	Too Small to fit wind tunnel
2	80	20	11.40	N/A	Too Small to fit wind tunnel
3	80	30	16.78		Good contrast, wind tunnel will fit, but with less clearance than other configurations, good focus
4	90	15	19.49		Non-circular image, moderate contrast
5	90	20	21.40		Non-circular image, low contrast
6	90	30	26.78		Very good contrast, allows enough space for wind tunnel, good focus

7	100	15	29.49		Non-circular image, blurry focus, low contrast
8	100	20	31.40		Lens height had to be adjusted, good contrast, leaves room for wind tunnel, focus slightly blurry
9	100	30	36.78		Lens height had to be adjusted, good contrast, leaves room for wind tunnel, focus slightly blurry

Based on the results of the optimization, the following configuration provided the best resulting images and thus it was the basis for the design of the optical plate:

**Table 4: Optimal Configuration for Schlieren System**

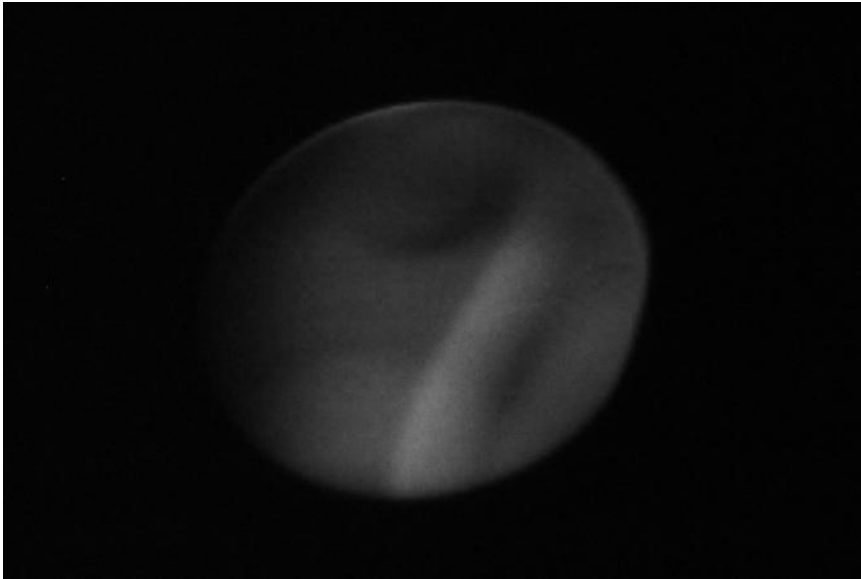
Components	Distance (cm)	Angle from test section (°)
Light to Collimating Lens	3	30
Collimating Lens to Slit	4	
Slit to First Mirror	18.5	
First Mirror to Second Mirror	90	N/A
Second Mirror to Razor	24	30
Razor to Focusing Lens	8.5	
Focusing Lens to Screen	15	



#### **4.1.4 System Validation Experiments**

To validate the chosen configuration, a number of phenomena were imaged using the system in its optimal configuration. The phenomena create density gradients in the surrounding air either through heating or by creating a relatively fast jet of gas (adjacent to still air) using a can of compressed air. Combinations of phenomena were also imaged. These images were modified using Windows Live Photo Gallery software (Microsoft Corporation, Redmond, WA) to adjust the brightness and contrast of the images as necessary. During modification, the brightness was increased slightly because the best images, which are obtained with the razor blade blocking half of the refracted light, tend to be very dark. Increasing the brightness makes the flow structures easier to see. For the same reason, the contrast of the images was increased slightly. Both of these modification processes are suitable for schlieren images because they change properties of the whole image rather than only a part of it. Therefore, the flow properties that can be discerned in the image are not altered through the image modification, but simply made easier to see. Image enhancement that changes the appearance of the flow with respect to the whole image as opposed to changing the whole image itself is not suitable for qualitative analysis of schlieren images.

## *Candle*



**Figure 15: Schlieren image of a candle flame**

Figure 15 shows the top of a candle flame where the density gradients produced by the uneven heating of air in the test section transition from smooth, gradual gradients to more random and sudden gradients in the air further above the candle. In the schlieren system, the image appears inverted on the screen, but for ease of analysis, all photos in this paper have been rotated to reflect the orientation of the phenomena as it was being imaged.

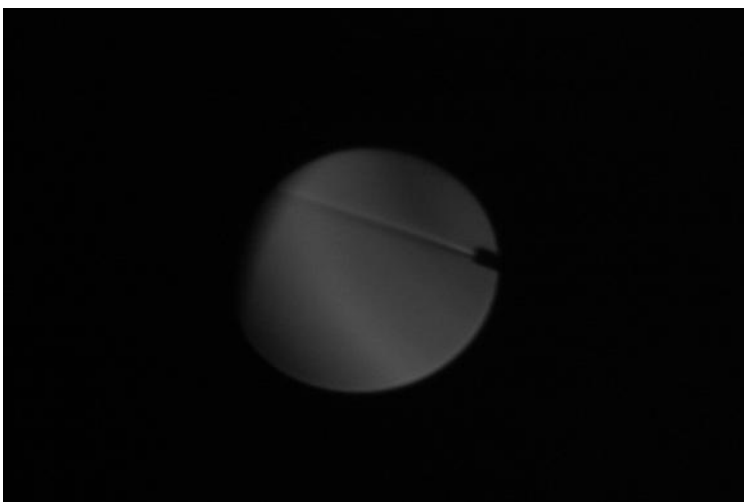
### *Heat Gun*



**Figure 16: Schlieren image of a heat gun**

The lip of the heat gun obstructs part of the light beam in the test section, thus producing a non-circular image. The heat gun not only produces density gradients that can be viewed with a schlieren system, but it also produces streak-like regions of similar density gradients, as can be seen in Figure 16.

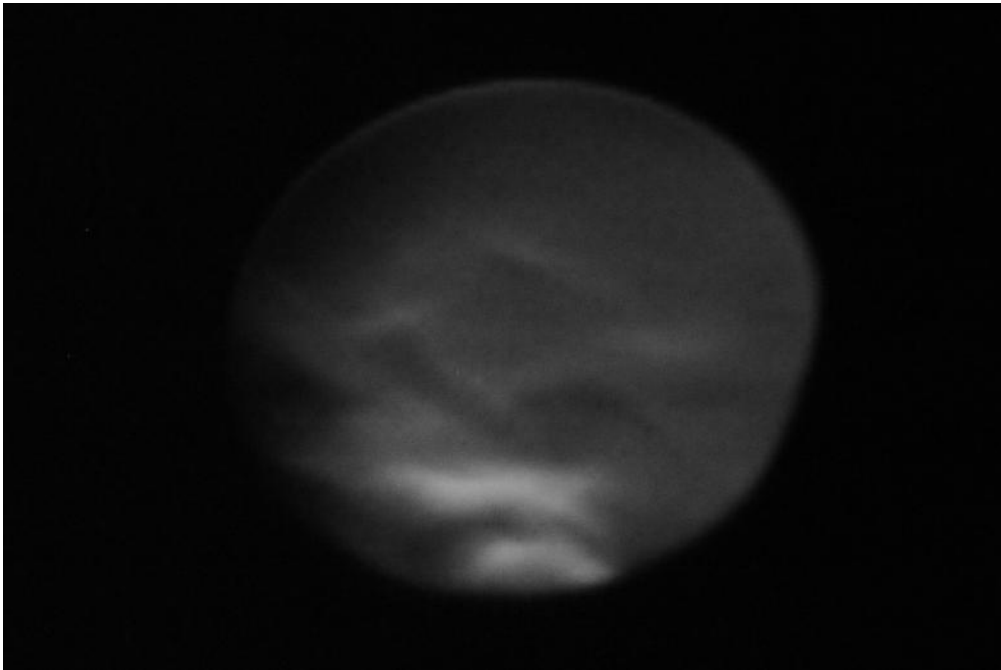
### *Compressed Air*



**Figure 17: Schlieren Image of a Jet of Air**

The compressed air produces a density gradient due to its velocity rather than temperature, as with the other phenomena in this study. The density gradients that will be observed in the wind tunnel will similarly be produced by the high velocity flow of air. The velocity of the flow is not imaged, but the differences in densities that are produced by the different relative velocities in the test section are what produce the dark and light areas in the image.

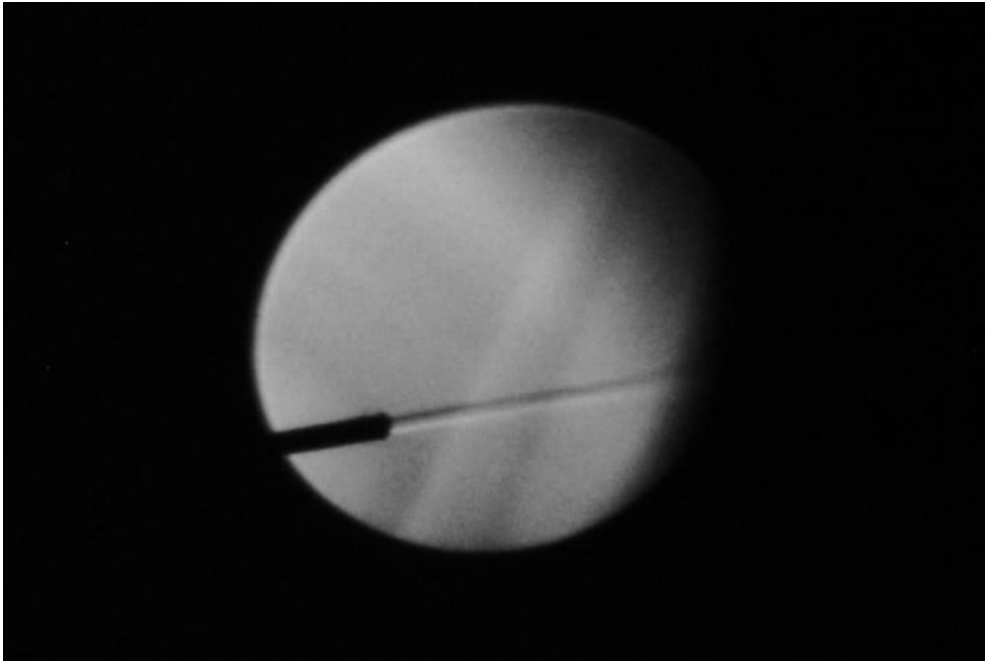
***Interference of candle and compressed air***



**Figure 18: Schlieren image of the interference between a candle flame and a jet of air**

Figure 18 shows the region directly above the flame of a candle where the density gradients would normally transition from being smooth and gradual to more erratic. This transition is further facilitated by directing a flow of high velocity air at the same region, thus producing the sudden and rapid gradients indicated by the distinct light and dark areas in the figure.

### *Non-interference of candle and compressed air*



**Figure 19: Schlieren image of non-interference between a candle flame and a jet of air**

Figure 19 shows two phenomena that are both in the test section of the schlieren system, yet not interfering with each other because they are placed approximately 15 inches away from one another in this image. This image demonstrates that the system has the sensitivity to detect density gradients anywhere along the length of the test section.

## **4.2 Manufacturing Test Nozzles**

New contours for the supersonic wind tunnel designed by a previous MQP group [27] for use with the vacuum chamber were created to test the viability of the dual-bell nozzle contour, and to compare the flow structures with those found in a conventional TOP nozzle design. The nozzle contour designs were scaled to fit the dimensional constraints of the existing test section.

### 4.2.1 CAD Nozzle Modeling

The previous MQP group [27] provided the SolidWorks CAD models for the basis of this project's supersonic wind tunnel test section design. The parts from the previous test section were adapted to this project's nozzle designs. The previous test section had a single piece that served as both the nozzle contours as well as the brackets connecting to end plates and acrylic windows (Figure 20). Last year's group started designing a new configuration for the test section, in which the contours would be separated from the brackets, so that the contours could be removed and replaced with different contours while using the same brackets (Figure 21). The contour is only connected to this bracket via three bolts, and the entire piece is within the O-ring seal to prevent leaks from arising due to the separation of these two pieces. This year's project finished designing and constructing this new test section design, which allows the wind tunnel to be more modular. The nozzle contours, designed for the first stage of the Nanolaunch vehicle, must be scaled down to fit the wind tunnel test section size. The contours for the Fluent analysis and actual application are on the order of half a meter to a meter in scale, while the test section is on the order of inches. In addition to the required dimensional scaling, the contour was also modified to adapt an axisymmetric flow channel (i.e. the nozzle) to the 2-D rectangular geometry inherent to the test section.

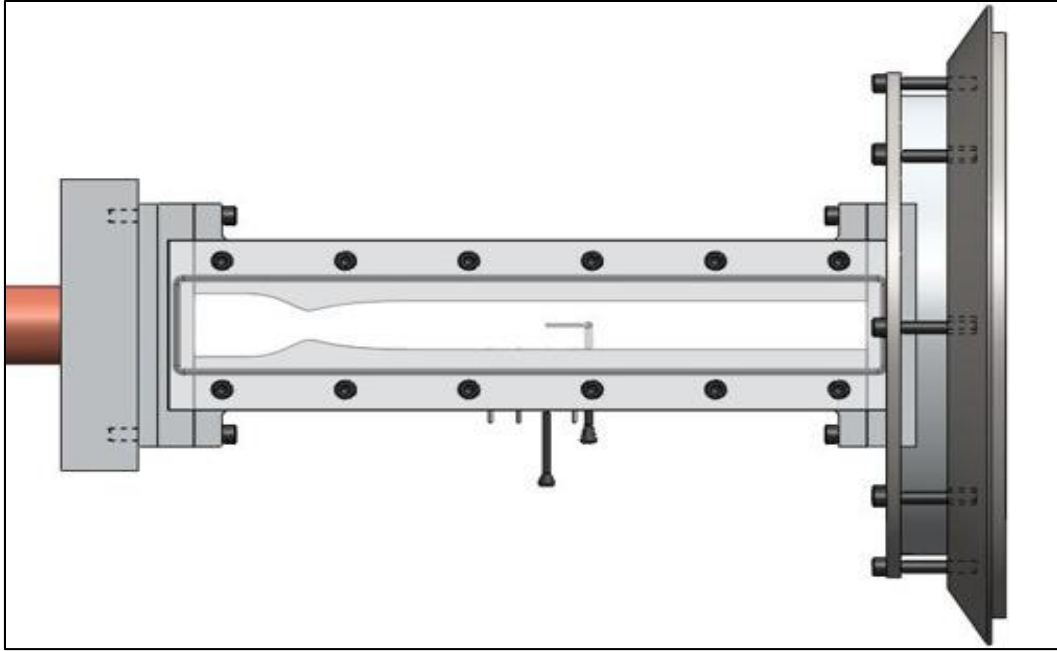


Figure 20: SSWT CAD model from the 2013 MQP [27]

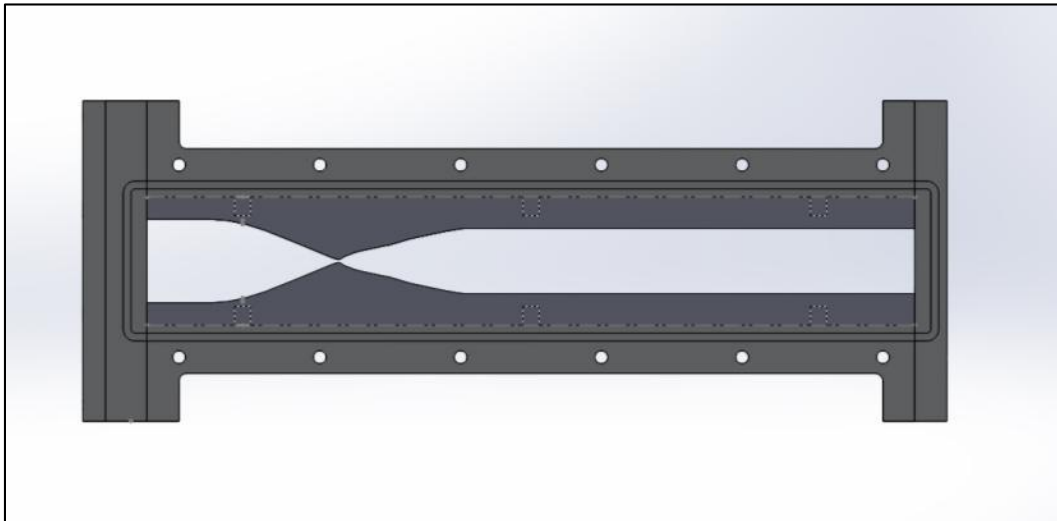


Figure 21: CAD model of new set-up with dual-bell contours

## 4.2.2 Manufacturing Constraints

The largest constraint in designing and manufacturing the nozzle contours was the small size of the wind tunnel test section. The size of the throat is governed by the design Mach number for the contour, but due to available machining capabilities, there is a limit to how

accurate the throat can be machined. The size of the test section itself limits how large the exit area can be, which changes how the throat area affects the overall nozzle design. This means that the area ratio may not be the same as it is for the original Fluent design. The manufactured contour was also limited in length in order to be able to use the same test section configuration as the previous MQP [27]. However, the assembly and disassembly of the wind tunnel test section was greatly simplified with the new parts. One set of contours can be replaced with another without any modification of other parts of the wind tunnel test section.

### **4.2.3 Manufacturing Processes**

Our test setup is based on work done by previous MQP groups; however, many components could not be reused for various reasons. The ball valve and mounting flange sections were reused from the supersonic wind tunnel, but most parts in the test section had to be machined for this project.



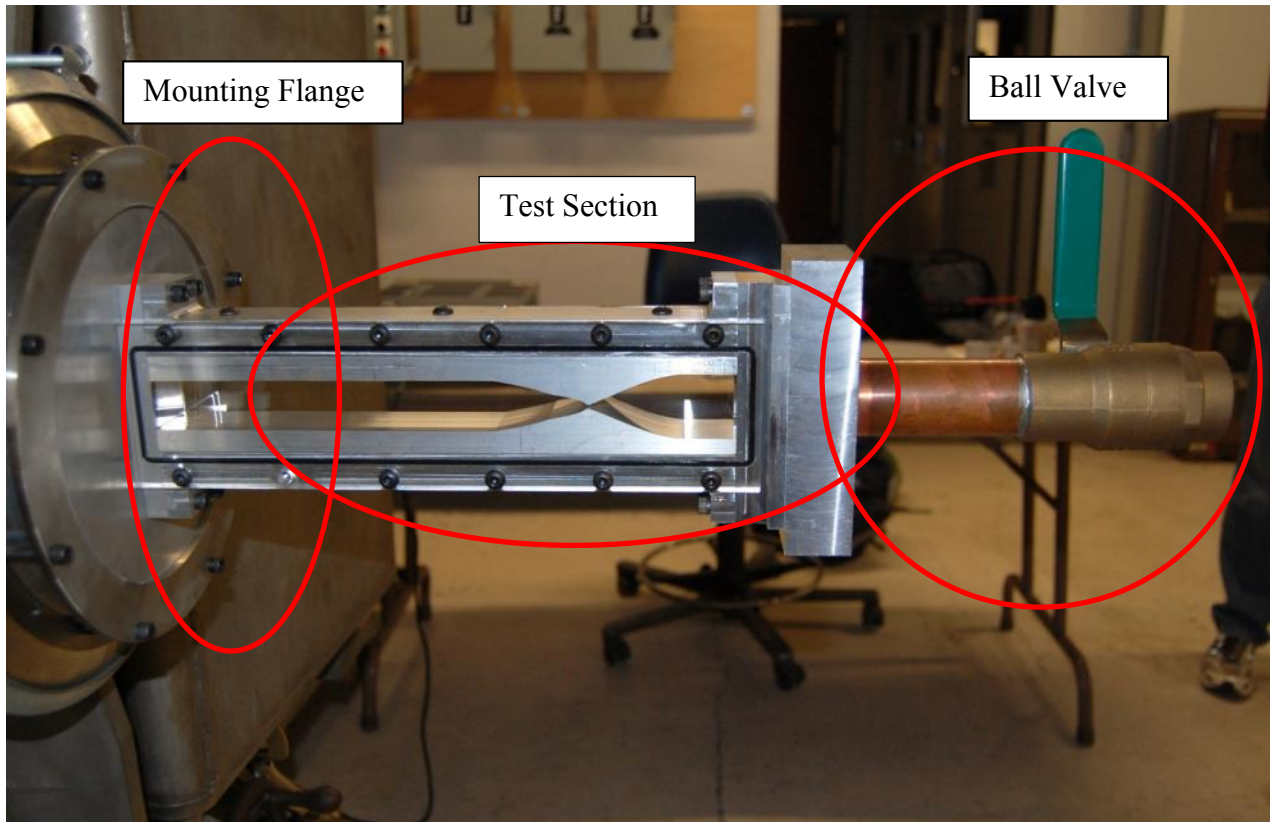
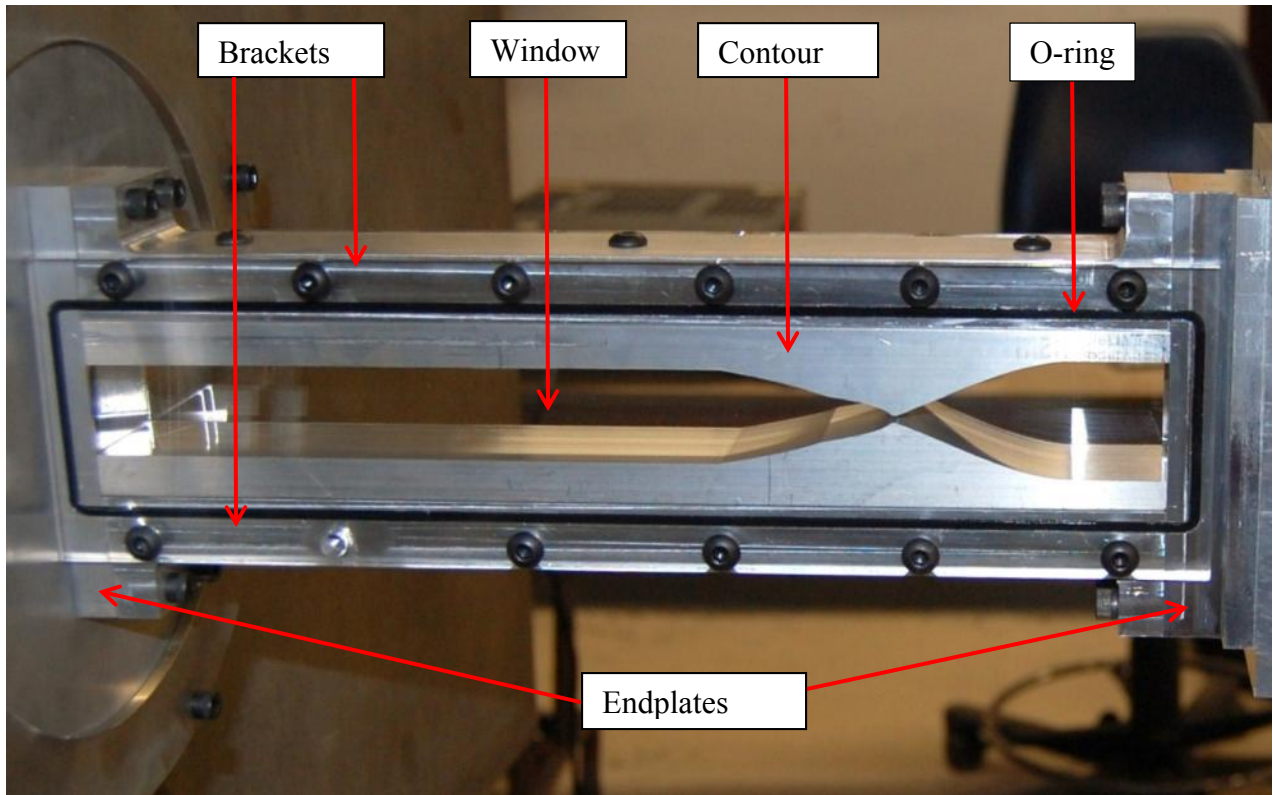


Figure 22: Wind tunnel set-up



**Figure 23: Test section with labeled parts**

### *Brackets*

The purpose of the bracket is to provide structure for the setup; it connects the windows, endplates, and contours via  $\frac{1}{4}$ -20 screws. The brackets were primarily manufactured by the previous MQP group, with the exception of the holes to connect the bracket to the endplate, which were drilled using a .257" drill to provide clearance for  $\frac{1}{4}$ " bolts. Since the brackets were made by a previous group, they determined a number of design parameters for the setup, including the location and size of the O-rings and the locations of the screws that hold the windows on.

### *Endplates*

There are two endplates in the setup: one at the inlet of the test section, which connects to the valve section of the wind tunnel, and one at the outlet, which connects the test section to the

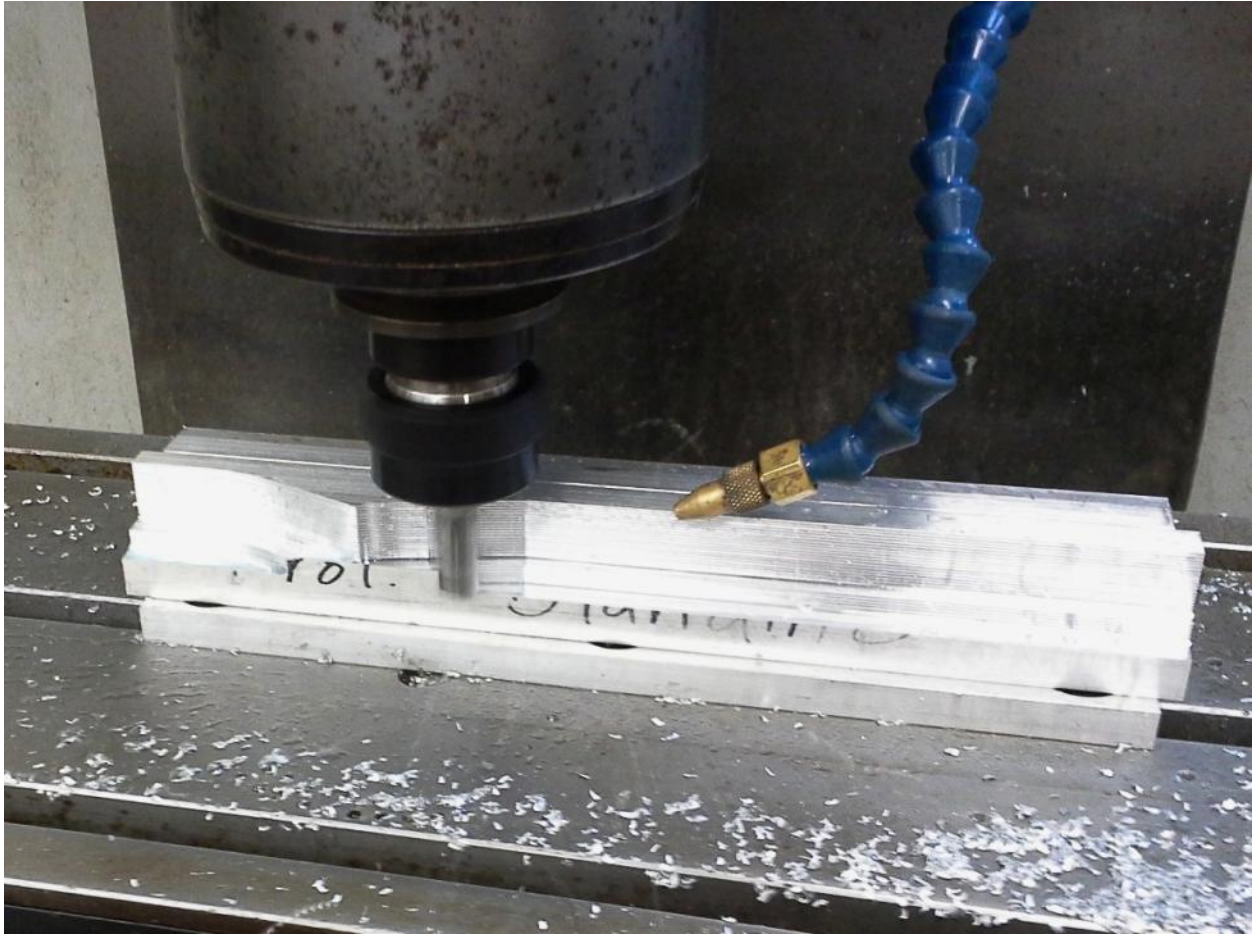
flange. The purpose of the endplates is to transition the channel size, which is 1" x 1.25" in the valve section, 1"x1.5" in the test section, and 1"x1" in the flange. The endplates were manufactured using a CNC machine with a 1/2" end mill, 1/4" ball mill, a .257" drill bit, and a 1/8" end mill.

### *Fixture plate*

While not a part of the final assembly, the manufacturing of the fixture plate was a key step towards machining the contours (Figure 24). The fixture plate is designed to hold the blank from which a contour is made to the machine during the manufacturing process. This part was made on a CNC machine using a 1/2" mill, a 3" face mill, a 33/64" drill bit, a .257" drill, and a 1/4" end mill.



**Figure 24: Fixture plate attached to CNC machine**



**Figure 25: Dual-bell contour during machining process using the fixture plate**

### *Contours*

The geometry of the contours was first created using Matlab, and the resulting curves were imported to SolidWorks. The final design of the nozzle was made using the equation driven curve feature. An attempt was made to use imported numerical points to define the curve, but this method did not produce a high enough resolution. These CAD designs were then transferred into CAM files that could be read by a CNC machine. The contours began as 1" x 1.5" aluminum stock that was cut down to approximately 12.25" in length using a horizontal band saw. These pieces were then milled down to 12" on a CNC machine using a 1/2" end mill. In the same process, a 0.201" drill bit was used to make the three holes that were later used to connect the

blank to the fixture plate and then to connect the completed contour to the bracket in the test setup. With the blanks screwed to the fixture plate, the machining of the contours was accomplished with a CNC machine using a ½” end mill and a 1” end mill. The tolerance of the CNC machine used was 6/1000”.

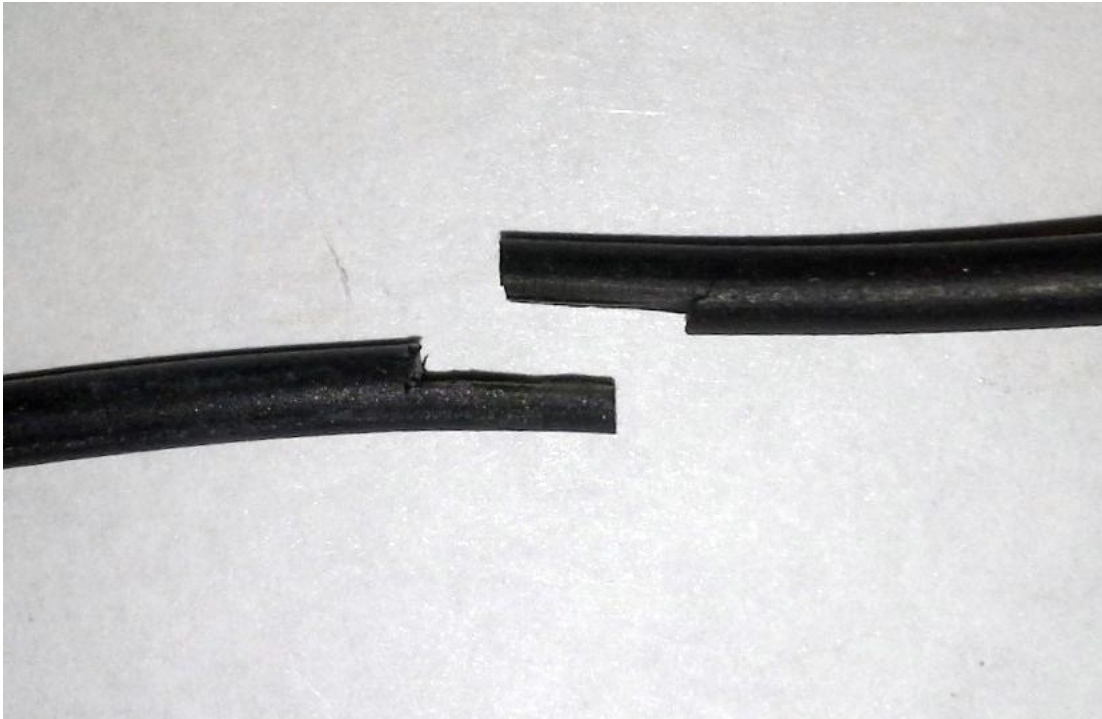
### *Windows*

The windows for the test section were originally made from ¼” clear acrylic. The dimensions and hole pattern were determined using the CAD model of the brackets. Once the design was complete, it was machined using the laser cutter. However, during testing it was discovered that fine, spider cracks formed around the holes in the acrylic when it was screwed down to the brackets. To alleviate this problem, ¼” clear polycarbonate, which is stronger and more resilient under compression than acrylic, was selected as the material to be used for the final design. The same CAD model was used to produce the polycarbonate windows, but they could not be produced on the laser cutter. Polycarbonate absorbs infrared radiation, so using a laser would result in poor edge fidelity, discoloration, and possibly burning of the material. Instead, the windows were machined using a CNC mill.

### *O-rings*

The O-rings were made using 0.1” diameter Buna-N (nitrile) O-ring stock and Loctite 404 super glue to splice the ends together. Because the super glue becomes very hard when dry, the joining surfaces at the ends of the O-ring stock were cut such that no cross section would be entirely hardened super glue, which would impede the compression of the O-ring and cause a leak (Figure 26). The O-ring stock was cut using a razor blade. Once the stock was cut to size and the ends cut to form a half-lap joint, a small amount of super glue was applied to one of the

joining surfaces. The joining surfaces were then brought together and held for approximately ten seconds until the glue dried.



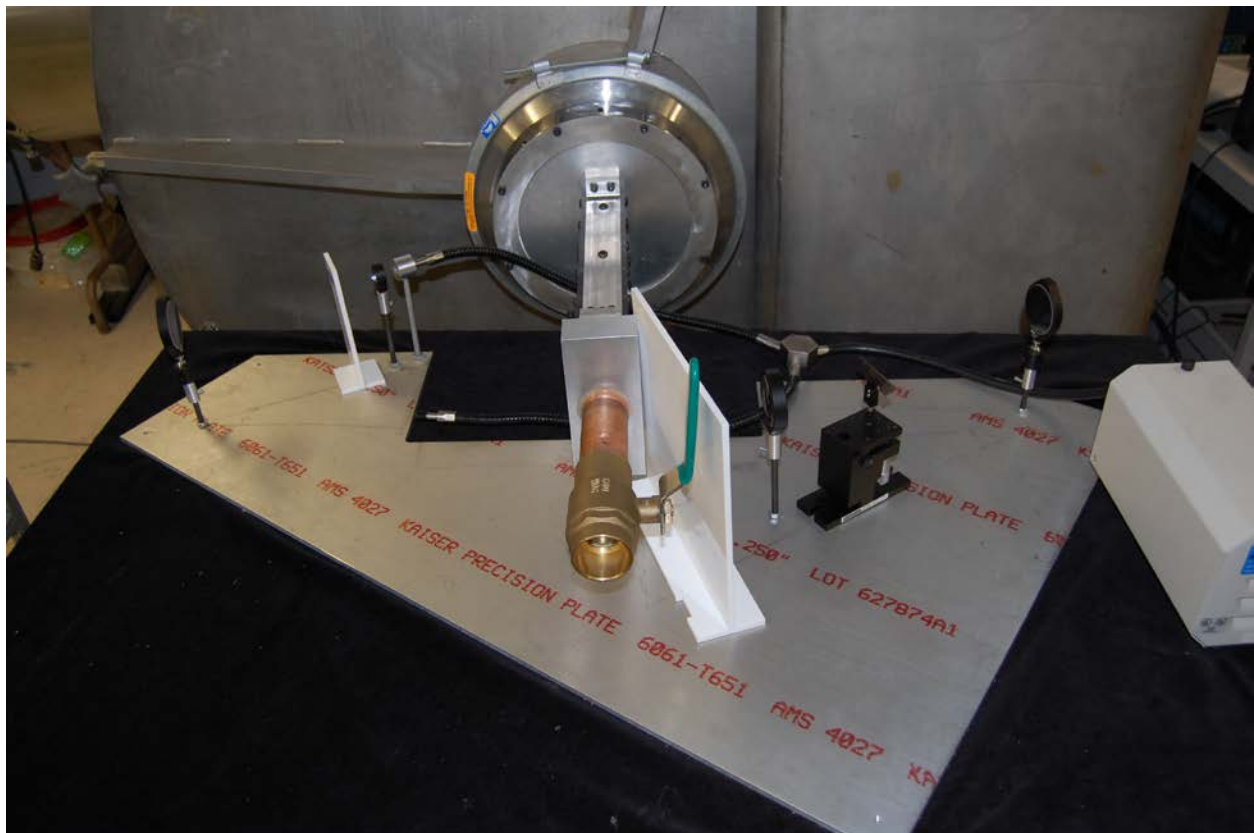
**Figure 26: Lap joint used for O-ring joining surfaces**

### **4.3 Testing Nozzles in Supersonic Wind Tunnel**

Once the new supersonic wind tunnel test sections and the improvements to the schlieren system were completed, the entire system was tested to see the effects of different contours on the flow. The schlieren system had been tested with a candle and a jet of compressed air to ensure that it worked properly, but the wind tunnel set-up could only be tested when connected to vacuum chamber. Both the dual-bell and Rao nozzle contours were tested to see how the flow structures differed between the two nozzle types and compared to the ANSYS Fluent simulations.

### 4.3.1 Test Set-Up

The test section is connected to the vacuum chamber via a mounting flange, and there is a ball valve at the other end of the test section, which is opened to start the test. The schlieren system sits on a table under the wind tunnel test section, with the optical elements mounted so they are centered on a plane that intersects the test section. The entire set-up can be seen in Figure 27. The schlieren system plate can be shifted on the table to focus on different areas of the test section.



**Figure 27: Test Setup**

The first tests run with the wind tunnel test section were to ensure that the set-up was working correctly. Leaks are a major concern for this project, because they prevent the vacuum chamber from pumping down. The first time the vacuum chamber was pumped down with the

new supersonic test section, leaks were immediately noticeable by a distinct hissing sound. Applying vacuum grease to the O-rings helped prevent some of the leaking; however, a small leak was still present, located between the brackets and the end plates of the test section assembly. This was sealed with silicone caulk. To ensure a solid seal, the brackets and end plates were disassembled and cleaned thoroughly before applying caulk to the entire face. The sealant was chosen to be airtight, but removable with a solvent so that the system could remain modular and allow for other contours to be tested. After applying the adhesive, the test section assembly was sufficiently sealed for testing.

Once the system was sealed enough for the vacuum chamber to pump down, the actual tests of the contours began. Each test begins by ensuring the vacuum chamber is pumped down, aligning the schlieren system so that the section of interest is in the field of view. One person captures schlieren images of the flow throughout the test. The image capturing starts when the valve is opened, and ends when the pressure in the vacuum chamber reaches atmospheric. Tests were conducted at various points along the length of the test section to see how the flow differed in and downstream of the nozzle.

### **4.3.2 Interpretation of Images**

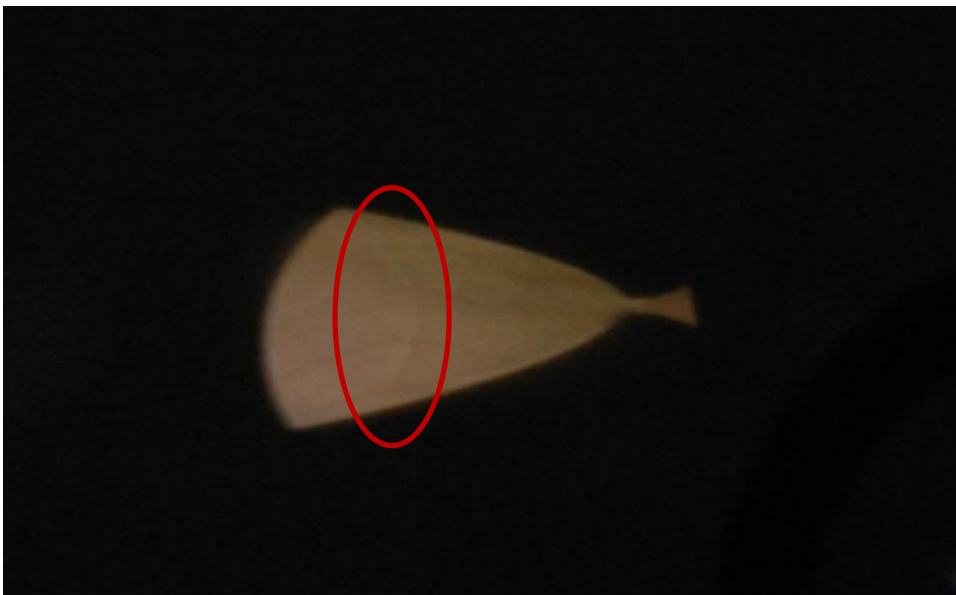
Images were taken throughout the duration of each test at a single location along the test contour. Multiple tests were conducted with both the dual-bell and Rao contours to image the flow at various points within and downstream of the nozzle (i.e. into the test section of the wind tunnel). The schlieren images were analyzed to determine the flow structures in the test section. Schlieren images show density gradients in a flow, so sharp changes in density appeared as dark lines in the schlieren images, while areas of constant pressure appeared bright. Examining the images over the course of one test shows how the flow changes as the back pressure increases



throughout the test. Multiple tests were conducted with each set of contours to confirm the repeatability of the flow structures captured with the schlieren images. The flow structures revealed in the images were compared to structures simulated with ANSYS Fluent to assess similarities and differences.

### 4.3.3 Rao Image Analysis

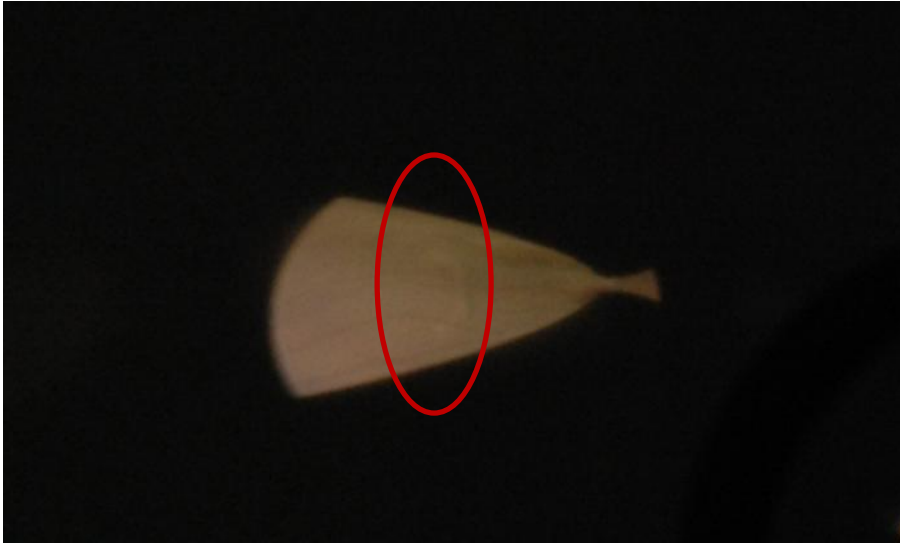
In several tests using the Rao contours, two flow features were imaged: A normal shock, and a series of boundary layer flow structures. A normal shock, which appeared in the nozzle immediately at the beginning of the test, consisted of a thin, dark curved line followed by a light region. This shock moved upstream as the backpressure increased. The normal shock was only visible for approximately the first thirty second of the test. During this time, it moved upstream through the nozzle.



**Figure 28: Normal shock with Rao Contours**

As the normal shock moved upstream through the nozzle and approached the throat at the beginning of the test, it began to assume a more angular geometry as opposed to curved shape.

The leading edge of the shock remained normal to the flow, but the tips became parallel to the nozzle contour. Very shortly after taking on this angled form, the normal shock dissipated.



**Figure 29: Normal Shock with Angled Shape in Rao Contours**

Immediately following the dissipation of the normal shock, a series of boundary layer flow structures began to appear. Each of these structures consisted of a dark streak, which indicates a rapid change in density, followed by a small, nearly circular light region, which indicates a negligible change in density in that region.



**Figure 30: Early Development of Boundary Layer Structures**

The first boundary layer structures that formed were relatively spread out. As the test went on and the back pressure increased, the structures moved upstream towards the throat.

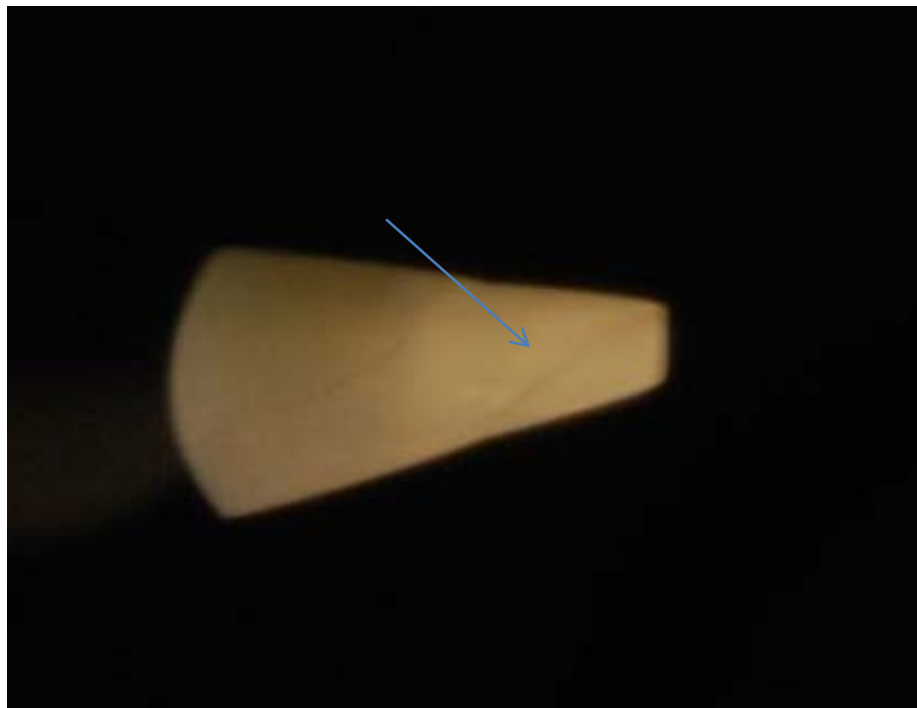


**Figure 31: Advanced Development of Boundary Layer Structures**

Towards the end of the test, the structures became very closely spaced as they continued to move towards the throat. Eventually, the structures combined into a single bright streak that was bounded by dark regions on either side. Shortly thereafter, the structure dissipated as the throat unchoked and the flow became subsonic. From this point on, no more flow structures were detected using the schlieren optical system.

#### **4.3.4 Dual-Bell Image Analysis**

In the schlieren images from the dual-bell tests, the flow structures seen are similar to those from the Rao nozzle tests. During the tests, in regions both near the throat and near the end of the nozzle, there were dark lines that travel towards the throat and are followed by round lighter regions near the boundary that also travel toward the throat and follow each other more closely as the test progresses.



**Figure 32: Shock structure at inflection point**

For the dual-bell case, the dark lines, corresponding to shock structures, form at the inflection point (Figure 32). This test was focused on the sections of the nozzle further downstream in order to see the behavior in the vicinity of the inflection point



**Figure 33: Boundary layer flow features**

As the test continues the first round lighter region forms at the inflection point along the boundary directly downstream of the shock. The beginning of the lighter region's formation can be seen in Figure 32, and the fully developed flow feature can be seen in Figure 33. Also visible are more of these boundary layer features, which continue develop at the inflection point and further towards the downstream end of the nozzle throughout the test. These flow features travel upstream toward the throat, following the shock.



**Figure 34: Throat region shock and boundary feature**

Figure 34 shows the shock and boundary layer feature closer to the throat in a test run that focused on the throat region. As the test continues, the shock is swallowed and the boundary features become closer together as they travel towards the throat. This phenomenon can be seen in Figure 35. At some point in the test, all of the remaining boundary flow features are swallowed by the throat as pressure differential decreases. Eventually the throat unchokes and the flow becomes subsonic for the remainder of the test.



**Figure 35: Series of boundary flow features**

## 5 Numerical Simulation

### 5.1 Mesh Generation

#### 5.1.1 Full-Scale Nozzles

The mesh for both the dual-bell and the Rao contours was generated using the ANSYS Workbench mesh generator. The meshed region covers the nozzle and a significant downstream area. The area downstream of the exit enables the solver to fully develop the flow within the nozzle, and enables visualization of different flow structures, such as Mach diamonds and expansion or compression waves that occur downstream of the exit plane. Figure 36 shows the fully defined Rao nozzle contour with the downstream section.

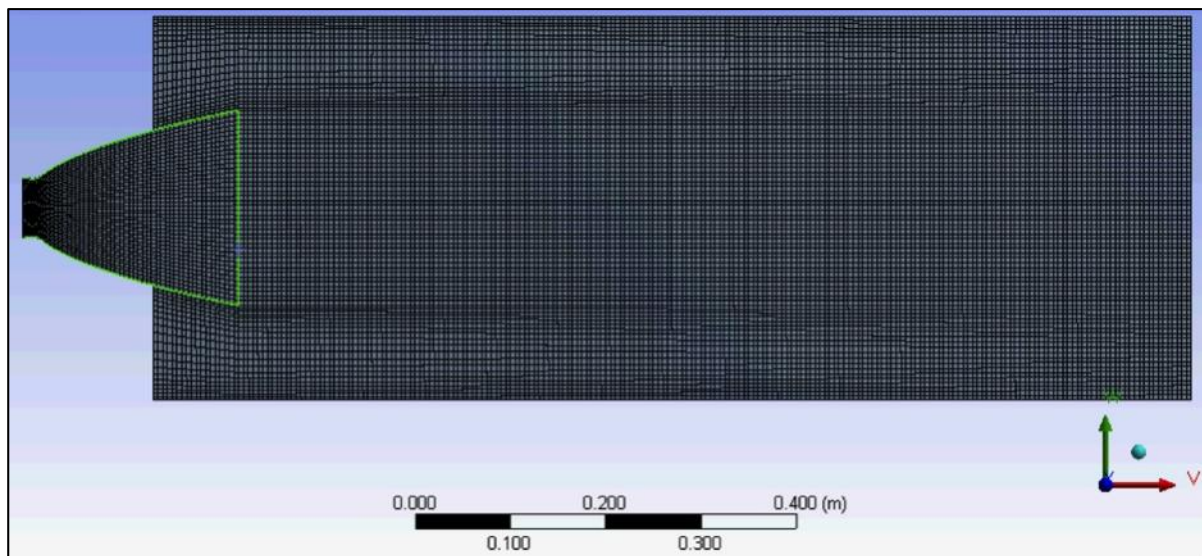


Figure 36: Rao nozzle mesh with downstream section

This mesh is dependent on properly labeling and joining edges within the “geometry” option within Workbench. While checking the imported geometry from SolidWorks, label the inlet, outlet, nozzle walls and nozzle exit plane by inserting a “named selection” on each of those

areas. This informs Fluent where to define boundaries and makes defining the boundary conditions much simpler. Furthermore, the line defining the nozzle’s exit plane needs to be joined to the interior of the body. The line the exit plane defines an imaginary surface that can be used for post processing the results to find the mass flow rate, velocity, and other important parameters. In order for the edge along the nozzle exit plane to be considered an imaginary surface, or, in Fluent’s terminology, an interior surface, the nozzle needs to be connected to the outer mesh. This is achieved by going to the tools option while editing the geometry, selecting “connect,” and applying it to those edges.

In order to define the size and relative orthogonality of the mesh, one opens the mesh editor and then inserts sizing information in the different locations according to the settings described in Table 5.

**Table 5: Edge sizing definitions for mesh generation of Rao Nozzle**

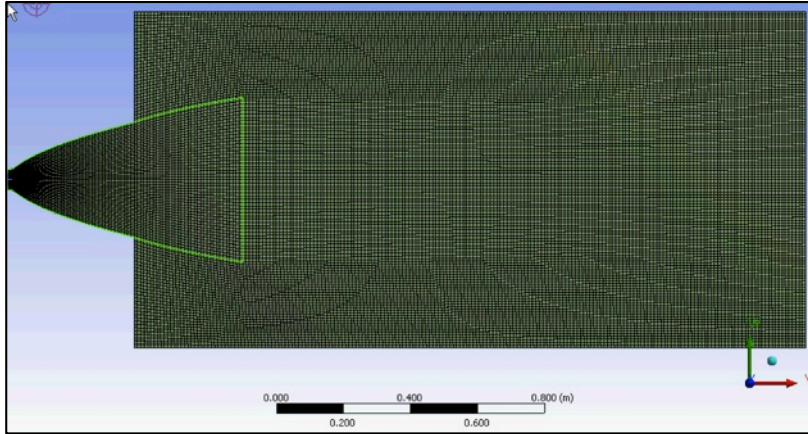
Component	Definition type	Characteristic Cell Height	Behavior
Inlet	Element size	5.00e-3 m	Soft
Nozzle outlet	Element size	5.00e-3 m	Hard
Nozzle walls	Element Size	5.00e-3 m	Soft
Outlet, right side	Element size	5.00e-3 m	Hard
Outlet, Top	Element size	5.00e-3 m	Hard
Outlet, Bottom	Element size	5.00e-3 m	Hard

The last step to ensure a reasonable quality of mesh is to insert mapped face meshing. A “good” mesh is made out of square cells of equal size, and the “mapped face meshing” control forces the mesh into quadrilateral sections using the defined boundaries as the starting point. Mapped faced meshing was added to both the nozzle and the downstream section separately and the mesh was ready to be generated.



The mesh for the dual-bell nozzle was generated in a similar manner as that of the Rao nozzle, with the only changes being in the edge sizing and the size of the downstream section.

Figure 37 is an image of the meshed used for modeling the dual-bell contour.



**Figure 37: Dual bell nozzle mesh with downstream section**

The mesh naming and settings for the dual-bell nozzles are outlined in Table 6.

**Table 6: Edge sizing definitions for mesh generation of dual-bell nozzle**

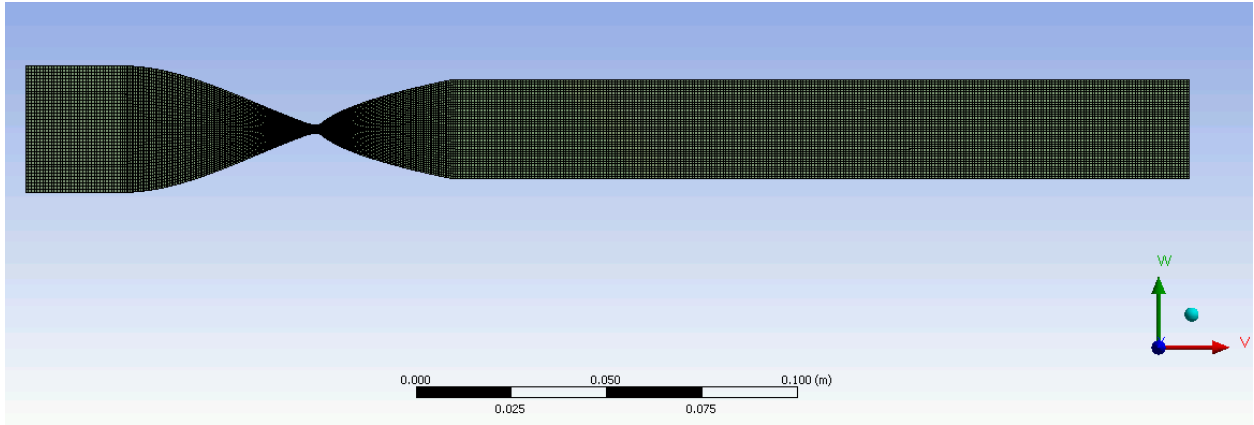
Component	Definition type	Characteristic Cell Height	Behavior
Inlet	Element size	5.00e-3 m	Soft
Nozzle outlet	Element size	1.00e-2 m	Hard
Nozzle walls	Element Size	1.00e-2 m	Hard
Outlet, right side	Element size	1.00e-2 m	Soft
Outlet, left side	Element size	1.00e-2 m	Hard
Outlet, Top	Element size	1.00e-2 m	Hard
Outlet, Bottom	Element size	1.00e-2 m	Hard

This sizing is twice that used for the Rao nozzle; however, the number of computational cells for the Rao nozzle is less than that of the dual-bell because the dual-bell nozzle is larger than the Rao.

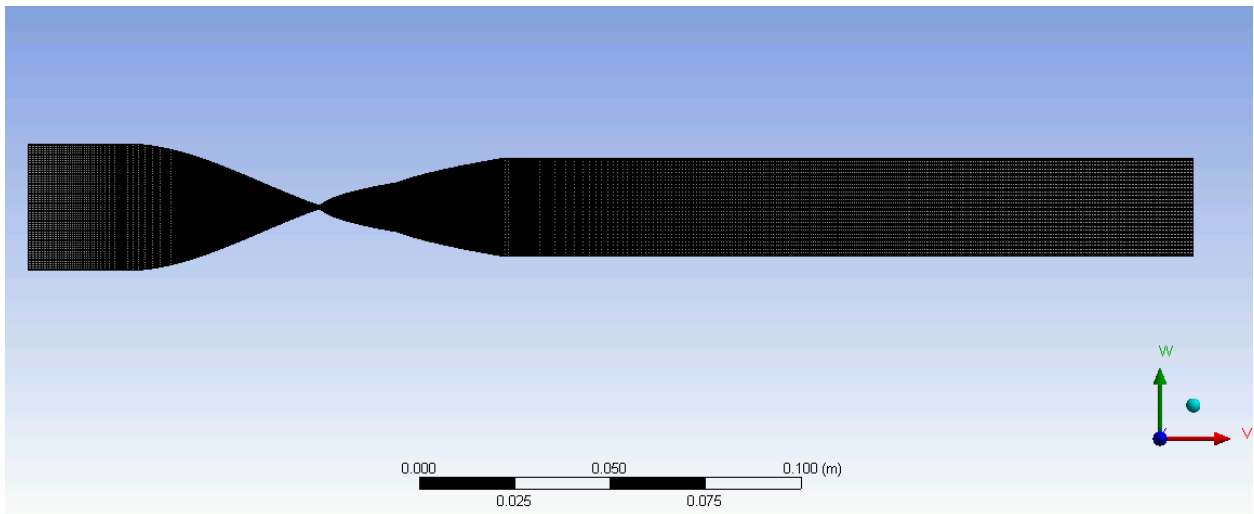
The convergence and accuracy of a computational fluid dynamics problem is in large part dependent on the quality of the mesh. A high quality mesh for a finite volume problem is composed of equal sized square cells. However, a curved geometry cannot directly be divided into squares. Due to this, the quality of the mesh is determined by its orthogonality, quantified in terms of a numeric value between 0 (bad) and 1 (good) that determines how close to rectangular boxes it is. The orthogonality quality is based off of the entirety of the mesh, and for the Rao nozzle's mesh, it is 0.78 and it is 0.73 for the dual-bell nozzle. These values are acceptable considering the curves that form each nozzle. The largest aspect ratio of the mesh is another numeric parameter for determining mesh quality. It quantifies the mesh's largest deviation from a square cell as a ratio of the large edge to small edge. The maximum aspect ratio for the Rao contour and the dual-bell contour are 3.95 and 1.01 respectively. Overall, the quality of the mesh is decent, and was not a concern for the solution.

### **5.1.2 Wind Tunnel Nozzles**

For testing of the wind tunnel in Fluent, the mesh generation was considerably simpler than the full-scale simulations. One major difference between the full-scale testing and the wind tunnel testing is elimination of the downstream section for the wind tunnel. This decision was made to reduce computational time as well as simplify the problem. The flow inside the vacuum chamber is also of little interest to this project and as such, was neglected. The full mesh for each wind tunnel contour can be seen below in Figure 38 and Figure 39.



**Figure 38: Rao Wind Tunnel Contour Mesh**



**Figure 39: Dual-Bell Wind Tunnel Contour Mesh**

The details of the parameters set for these meshes are detailed in Table 7 (Rao) and Table 8 (dual-bell). Due to the complexity of the dual-bell contour, each section of the contour has been color-coded in Table 8. The contour schematic is shown in Figure 40. Overall, the Rao mesh has larger cells than the dual-bell mesh. The primary reasons for this are the inflection point and the smaller throat area in the dual-bell contour. For the dual-bell nozzle, the mesh used for the Rao contours would not provide enough fidelity for modeling the geometric features. This would suppress the flow features that are expected, leading to inaccurate results.

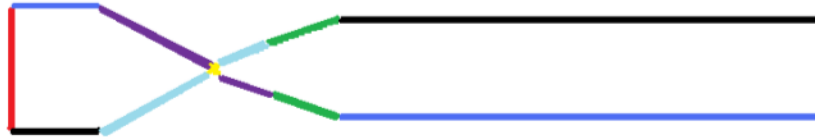
**Table 7: Edge Sizing Definitions for the Rao Wind Tunnel Contour Mesh**

Component	Definition type	Size Parameter/Number of Divisions	Behavior
Inlet	Number of Elements	40	Soft
Outlet	Number of Elements	40	Soft
Top and Bottom Straight Walls before nozzle	Element Size	7.5e-4	Hard
Entry Cubic Curve (curve before throat)	Element Size	5e-4	Hard
Throat (both curves)	Element Size	1e-4	Soft
Top and Bottom Straight Walls after nozzle	Element Size	7.5e-4	Hard
Nozzle	Element Size	5e-4	Soft

**Table 8: Edge Sizing Definitions for the Dual-Bell Wind Tunnel Contour Mesh**

Component (Color on Figure 40)	Definition type	Size Parameter	Bias Factor	Bias Type	Behavior
Inlet (● Red)	Number of Divisions	65	N/A	N/A	Hard
Outlet (● Orange)	Number of Divisions	65	N/A	N/A	Hard
Second Curve of Nozzle (● Green)	Element Size	2.5e-4	N/A	N/A	Soft
First Straight Top, Straight Bottom Back (● Blue)	Element Size	5e-4	3	_____	Hard
Inlet Top, First Nozzle Bottom (● Purple)	Element Size	2.5e-4	2.5	_____	Hard
Inlet Bottom, First Nozzle Curve Top (● Light Blue)	Element Size	2.5e-4	2.5	_____	Hard
Throat Bottom, Throat Top (● Yellow)	Element Size	1e-4	N/A	N/A	Hard
Throat Top, Throat Bottom (● Yellow)	Element Size	1e-4	N/A	N/A	Hard
First Straight Bottom,	Element Size	5e-4	3	_____	Hard

Straight Top ● Black)					
--------------------------	--	--	--	--	--



**Figure 40: Key for Table 8**

One key feature to note about the dual-bell wind tunnel contour mesh is the bias (the variation of size of cells within a specified region), created in order to improve the orthogonality of the mesh. The bias factors were chosen to maximize compatibility across disparate meshing regions. For example, there is a small bias toward the nozzle on the exit straight sections (black and blue lines in Figure 40). This has two significant benefits: first, there is not a large difference between mesh cell sizes between regions, which can create issues in Fluent and reduce orthogonality; second, the bias allows for a coarser mesh in the area closer to the exit of the wind tunnel, where less resolution is acceptable. One limitation of the ANSYS Meshing tool is that the bias function has some strange effects. This is why there is a crossover pattern; if the top and bottom edges are selected with a bias, the biases will oppose each other. An example of this is shown in Figure 40.

The final statistics for each mesh are detailed in Table 9, shown below.

**Table 9: Statistics for Wind Tunnel Contour Meshes**

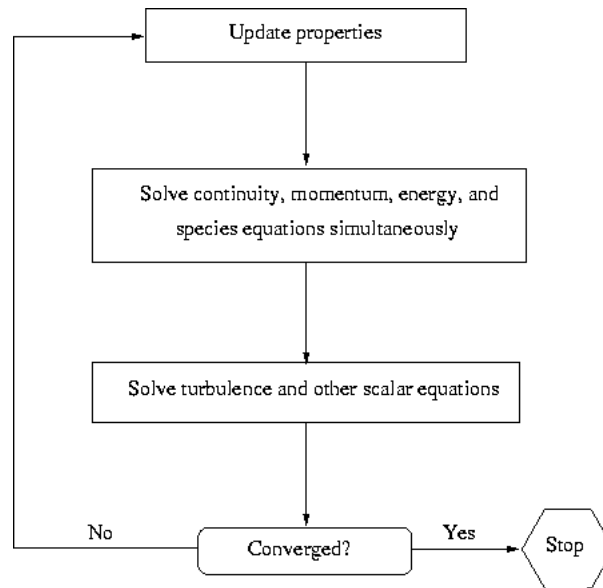
	Rao Wind Tunnel Contour Mesh	Dual-Bell Wind Tunnel Contour Mesh
Number of Nodes	20254	55572
Number of Elements	19720	54665

Orthogonality	.7766	.7492
Maximum Aspect Ratio	.7338	.7343

## 5.2 Fluent Solvers

Fluent consists of two numerical methods: a pressure-based solver and a density-based solver. Both methods use a finite-volume discretization method. The pressure-based solver is applicable for low speed incompressible flows, while the density-based solver is capable of calculating compressible flows. Flow through a rocket nozzle is highly compressible and can include shock structures, which requires the density-based approach. This was the focus throughout this project.

The density-based solver uses the momentum equations to calculate the velocity field, the continuity equation to obtain the density field, and the equation of state to produce the pressure field. Fluent solves the governing integral equations for conservation of mass, momentum, and energy. Additional properties, including turbulence, can be added to the simulation when appropriate. The governing equations are solved using the following iteration loop to meet convergence criteria.



**Figure 41: Fluent method of solving governing equations [Copyright © Fluent Inc., 2006]**

The governing equations can be solved using an explicit or a coupled-implicit method. The explicit method solves a given variable using only values already known at that step in the iteration. This means that the unknown values in each cell can be solved one at a time. A coupled-implicit method solves for an unknown variable in the cell using both existing and unknown values from surrounding cells; the equations must be solved simultaneously for this method. The coupled-implicit method is better suited for this application because of its ability to solve for several unknown parameters simultaneously.

Once the solution is in progress, several parameters can be monitored. For each iteration, residual sums of the variables are calculated; this serves to track convergence. Residuals approach zero as the solution converges.

### **5.3 Benchmark Results**

A hot-fire nozzle test for a solid rocket booster involves many complex variables, including combusting reactants, un-combusted and partially combusted particles mixing with the flow, non-ideal gas behavior, and significant heat transfer effects. A test involving the use of a



“cold” gas (room temperature) to flow through the nozzle is often performed before a hot fire test in order to test the nozzle’s shape and resulting flow patterns [29]. The Fluent simulations were constructed to model cold flow tests in order to reduce computational time by reducing the complexity of the solver. Each case was set up assuming that the operating gas behaved as an ideal gas and that it was air. The  $\kappa$ -epsilon turbulence model was selected for the simulations due to the focus on the flow structures within the nozzle. As stated in section 2.4.2, the  $\kappa$ -epsilon model is a two-equation turbulence model and it is commonly used for nozzle analysis. A final simplification applied to both the full-scale Rao and dual-bell nozzle cases in particular was to work mostly with relative pressure ratios rather than the expected pressures within a real nozzle due to convergence difficulties using the actual pressures. This involved using atmospheric pressure for the chamber pressure and blowing down to low pressures according to a predefined pressure ratio expected to be found during the flight scheme. Four different types of cases were examined including: a full-scale Rao nozzle, a full-scale dual-bell nozzle, and a wind tunnel 2-D approximation comparison case for both the Rao and dual-bell nozzles.

### **5.3.1 2-D Simulation of a Conventional Contour**

The contour plots below represent 2-D axisymmetric flow through a conventional Rao nozzle. The Rao nozzle was designed to perfectly expand from  $10^7$  Pa to  $10^5$  Pa (1 atm), a pressure ratio of roughly 100. These cold flow tests were performed with chamber pressures of one atmosphere instead of  $10^7$  Pa for simplicity. Ambient pressures included vacuum, 6.6 Pa (pressure ratio of 15,350), 100 Pa (pressure ratio of 1013.25), 10,000 Pa (pressure ratio of 10.13), 25,000 Pa (pressure ratio of 4.05), 50,000 Pa (pressure ratio of 2.026), and 75,000 (pressure ratio of 1.35).

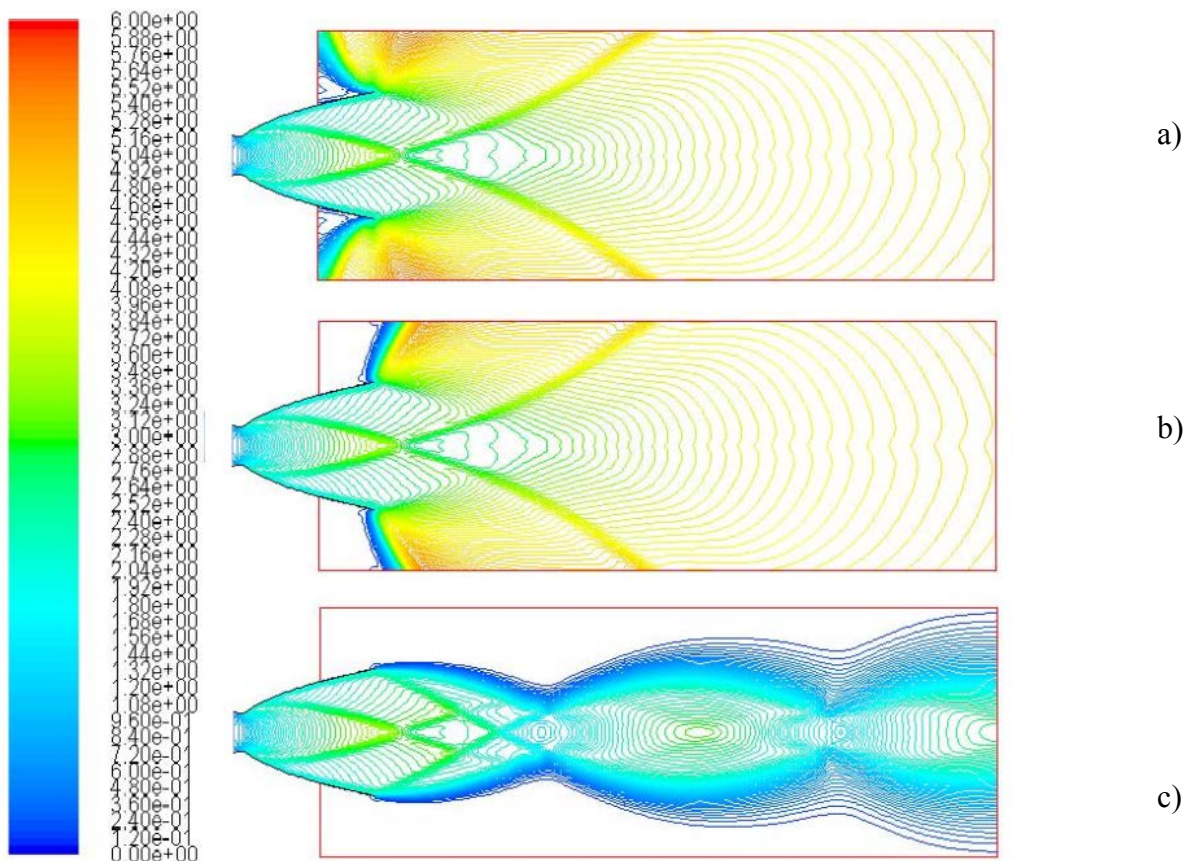
Each case used the same setup parameters with the exception of back pressure to ensure comparable results. The  $\kappa$ -epsilon turbulence model was used with the standard wall treatment and no additional heating effects. The inlet to the nozzle and the ambient exit section downstream of the nozzle were set as a “pressure inlet” and a “pressure outlet” respectively. Thus, the desired chamber and ambient pressures could be set. The nozzle exit plane was not defined as a pressure outlet because the pressure at that plane is not a preset value and changes depending on the location of any shocks or flow disturbances. All cases used a constant temperature of 300 K on all boundaries.

Convergence criteria for the Rao nozzle cases were set to  $1 \times 10^{-3}$ . When the residual values all fell below  $1 \times 10^{-3}$  the solution was considered converged. The Courant number is a dimensionless ratio of the average velocity multiplied by the time step divided by the grid size in a mesh cell. In the case of a fixed mesh, it determines the time step size. It was varied throughout the iterative solution process. For these cases, increasing the Courant number roughly every 10,000 iterations (from about 0.5 to 5 in increments of 0.5) helped the solution converge. Increasing the Courant number in this manner turns low frequency error into high frequency error, leading to a decrease in residual values.

Fluent’s post processing has the capability to calculate several flux values including mass flow rate. The mass flow rate was measured at the nozzle inlet and exit as well as the ambient exit section for all six converged cases. The resulting mass flow rate was roughly 14.13 kg/s for all three planes in each case with a maximum difference of 0.04%.

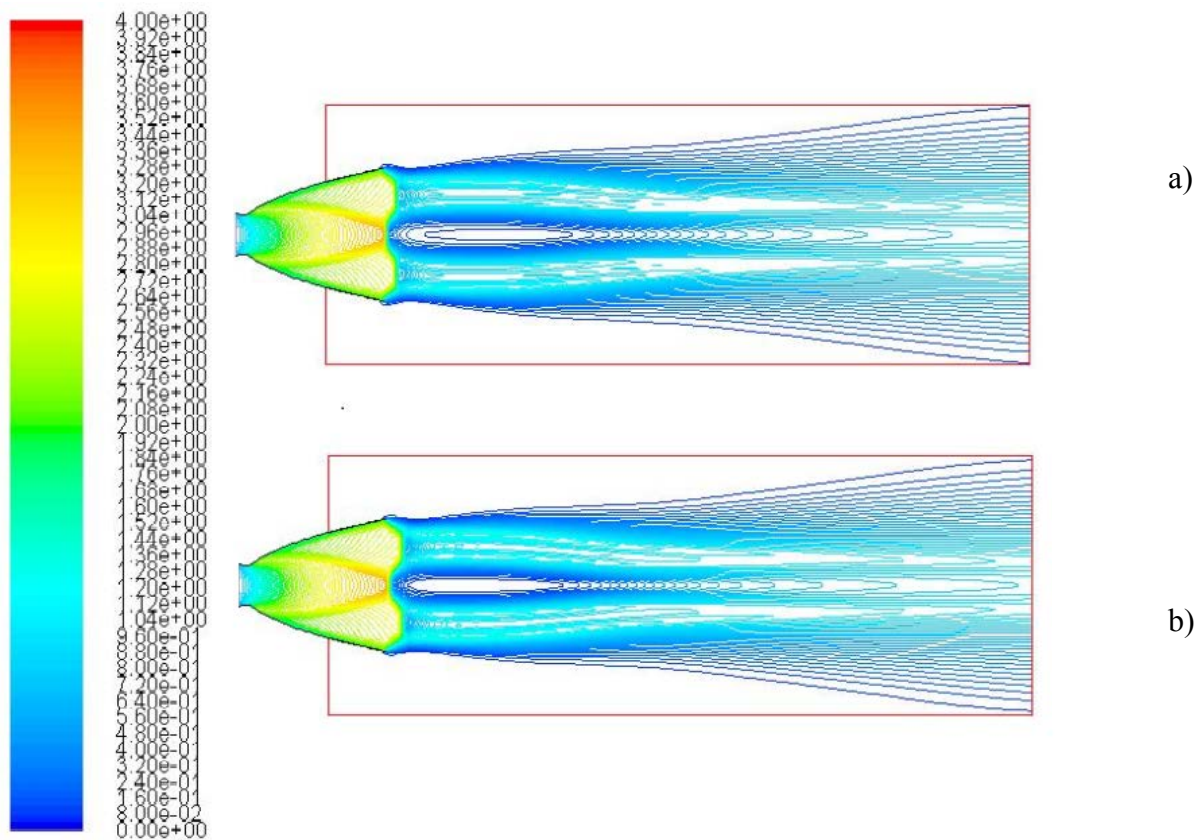
The first two cases, shown in Figure 42a and Figure 42b, are under-expanded as predicted. Both are supersonic throughout the nozzle and show expansion fans above and below the nozzle exit plane. The Mach number and severity of expansion at the exit decrease as the

pressure ratio decreases (from Figure 42a to Figure 42b). Figure 42c shows an over-expanded flow structure. Oblique shocks form at the exit plane of the nozzle, forcing the flow inward. The flow then shows expansion fans followed by more oblique shocks as it moves downstream. Earlier in the iteration process, the flow expanded too quickly towards the ambient boundaries. This produced regions with a Mach number in excess of 100. As the solution progressed, this error was phased out and the correct flow structure was achieved. The ambient pressure boundary in all Rao cases is seen to have the non-physical effect of reflecting the waves, so this error points to an ambient region that is too close to the nozzle exit. Selecting a “non-reflecting boundary” option in Fluent is not compatible with pressure ratios this high and accordingly was not chosen.



**Figure 42: Rao Mach contours with chamber pressures of 101325 Pa (1 atm) and back pressures of a) 6.6 Pa, b) 100 Pa, c) 10,000 Pa**

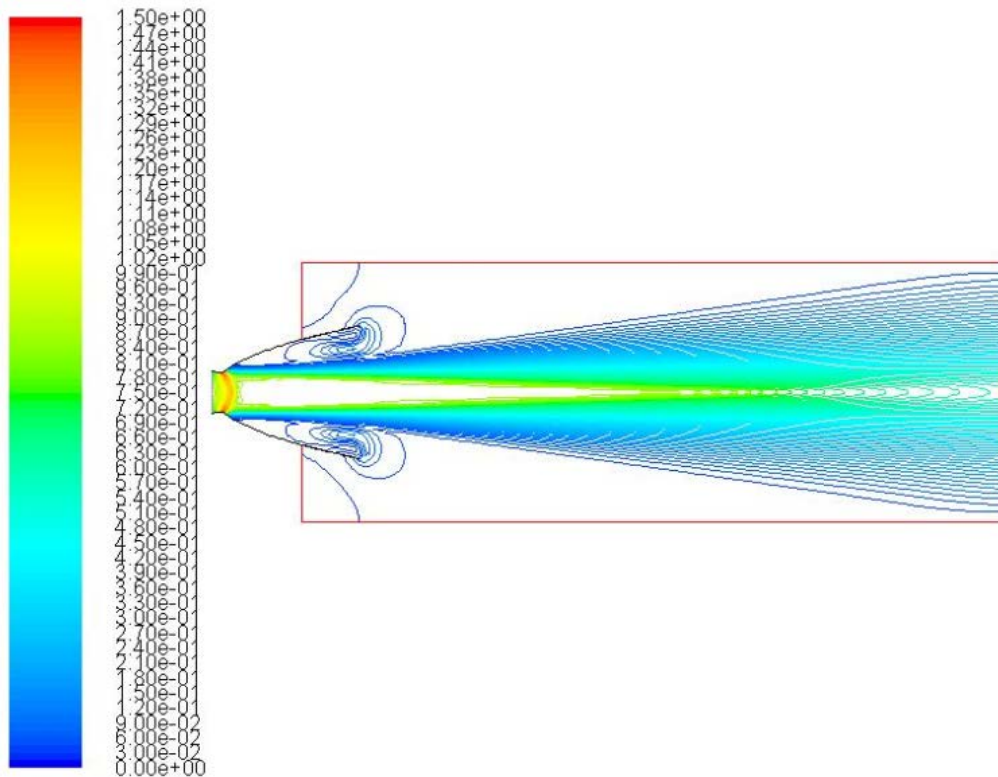
The two cases in Figure 43 are over-expanded with pressure ratios of 4.05 and 2.026 respectively. The nature of an over-expanded flow is that it does not expand outward (upward and downward in the figure) but rather turns inward. With this said, flow conditions at the ambient boundary were not an issue for these two cases as they were for the cases in Figure 43. Both contour plots show two normal shocks at the exit plane with a bubble of subsonic flow downstream. The shocks are initiated at the top and bottom edges of the nozzle and propagate inward. The presence of these shocks is believable because the flow is over-expanded but not critically over-expanded, so the flow is still supersonic throughout the nozzle.



**Figure 43: Rao Mach contours with chamber pressures of 101325 Pa and back pressures of a) 25,000 Pa and b) 50,000 Pa**

The contour plot shown in Figure 44 is a critically over-expanded case. One would see this type of flow much closer to sea-level than vacuum, depending on the nozzle design of

course. This would correspond a time close to the end of a test using the Supersonic Wind Tunnel, when the pressure inside and outside of the vacuum chamber were nearly equal. The flow in this case is subsonic throughout the nozzle with the exception of a small region (deep red) right at the throat. In addition, the flow does not expand out wider than the height of the throat until well downstream of the nozzle exit; this is drastically different than the flow pattern seen in the five previous cases. The final key feature to take note of is the presence of tip vortices forming at the top and bottom of the nozzle exit. In these regions, the flow is swirling back towards the nozzle and not contributing to any thrust produced by the nozzle.



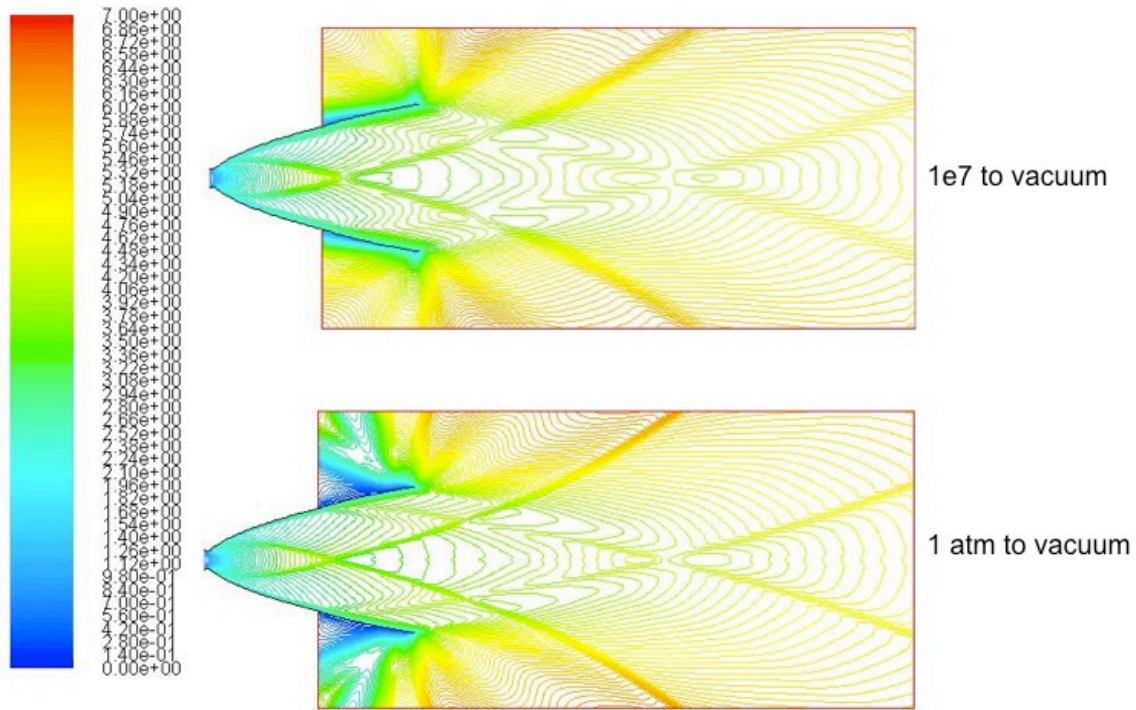
**Figure 44: Rao Mach contour with a chamber pressure of 1 atm and a back pressure of 75,000 Pa**

### 5.3.2 2-D Simulation of a Dual-Bell Contour

The dual-bell nozzle was designed for isentropic expansion with pressure ratios of 150 and 1000 for the first and second bells respectively. The modeled cases represent 2-D, axisymmetric model of the dual-bell nozzle. The designed pressures were meant to start with a chamber pressure of  $10^7$  Pa and drop to ambient pressures of 69718 Pa and 10329 Pa, however, as discussed earlier, in order to simplify the problem and ensure convergence, the chamber pressure was reduced to atmospheric. Consequently, the pressure ratios ranging from 4 to 1000 were used to examine the performance of the dual-bell nozzle. The ambient pressures for the design points were a primary focus, and the ambient pressure corresponding to the two contours were 675.5 Pa and 101.325 Pa for the first and second bell respectively (assuming a 1 atmosphere chamber pressure). Pressure ratios of 4, 10, 20, 50, 100 and infinity were also examined for comparison and validation.

All of the cases used the same general settings in order to keep them as comparable as possible. The inlet and outlet were specified as a “pressure inlet” and a pressure outlet” respectively. The dual-bell cases convergence criteria were set to  $5 \times 10^{-3}$  for all of the residuals, leading to a maximum of 1% to 2% difference between the inflow and out flow mass-flow and heat transfer rates.

Two cases converged with the ambient pressure set to zero; the difference between the two was that one case started with the predicted chamber pressure of  $10^7$  Pa (1500 psi) and temperature of 1100 K whereas the other had an atmospheric chamber pressure (101325 Pa) and a chamber temperature of 300 K. The pressure outlet boundary condition for both cases was a “non-reflecting boundary,” which forces the pressure along the outlet to represent the far field downstream pressure. The Courant number was selected to be 0.1 for both cases.



**Figure 45: Dual-bell Mach contours. Top design pressure to 35.7 Pa; bottom atmospheric pressure to 35.7 Pa**

The top contour in Figure 45 shows the Mach contour of the 107 Pa chamber pressure case and the middle Mach contour of Figure 45 shows the Mach contour of the atmospheric chamber case. A significant difference between the two cases is that the expansion waves at the exit do not turn the flow a complete 180° for the atmospheric case. Note that both of the cases have extremely high Mach numbers approaching the downstream boundary, and that the flow continues to accelerate after leaving the nozzle. For the 10<sup>7</sup> Pa chamber pressure case, the Mach number around the edges of the model approaches 7 whereas it approaches 6.1 along the edge of the atmospheric case. One possible cause could be that the continuum assumption begins to break down around the exit of the boundary. Fluent uses a Navier-Stokes based solver coupled with continuity and the energy equation to be applicable, all of which rely the assumption that there are enough molecules in any mesh cell such that the average behavior of them can be considered the overall behavior of the fluid. In a vacuum, there are very few gas particles, and

the continuum assumption governing Fluent's solver breaks down. In order to check if continuum held, the Knudsen number was checked. The Knudsen number is defined as

$$Kn = \frac{\lambda}{l_c} \quad 19$$

where  $l_c$  is a characteristic length for the domain, and was chosen to be the throat radius. The mean free path,  $\lambda$ , was calculated by [30]

$$\lambda = \frac{k_B T}{\sqrt{2} \pi d_{mc}^2 P} \quad 20$$

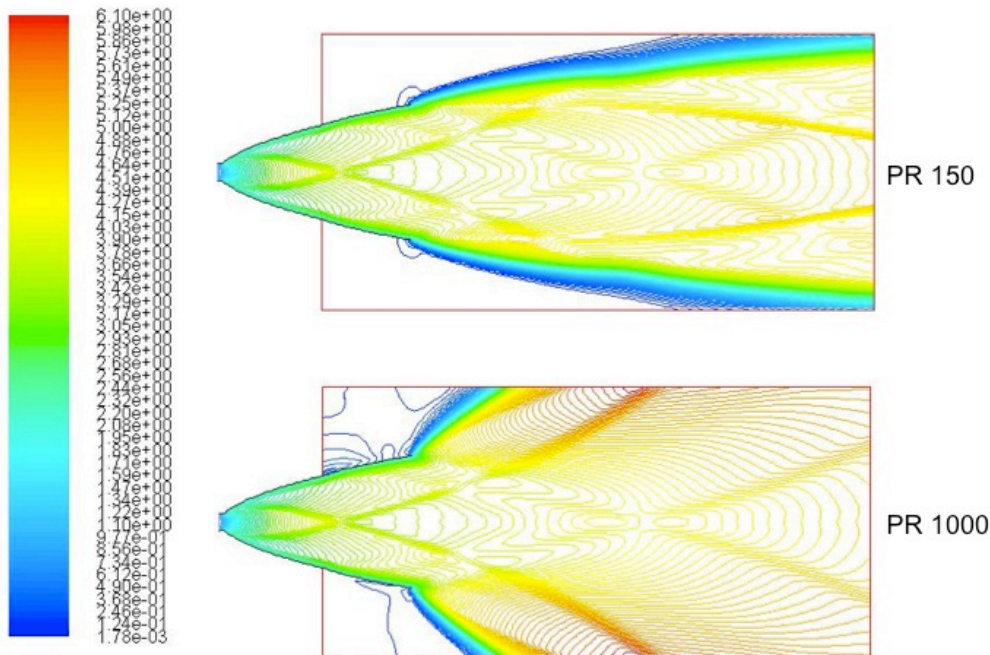
The mean free path was calculated with the Boltzmann constant,  $k_b=1.3806 \times 10^{-23}$  J/K, the static temperature and pressure, T and P respectively, and the average diameter of a nitrogen molecule,  $d_{mc}$ . The pressure around the edge of the outlet boundary for the  $10^7$  Pa case was 35.7 Pa, and the temperature was 33 K. The average diameter of an air molecule was 3 Å [5], which lead to a Knudsen number of 0.00111. The outlet pressure for the atmospheric chamber pressure case was 70 Pa, and the temperature was 46 K, leading to a Knudsen number of 0.00074. Generally, continuum holds if the Knudsen number is under 0.01, therefore the continuum assumption is valid. These two cases had the lowest ambient pressures, and were used as a general check for all of them to ensure continuum held. The Knudsen numbers for all of the remaining cases was below  $10^{-4}$ , therefore the continuum assumption was valid for all of the dual-bell cases.

The solver and boundary conditions setup and approach to the solution for all of the cases without an infinite pressure ratio were the same. The inlet total pressure was set to 101325 Pa and the inlet supersonic gage pressure (static pressure) was set to 80000 Pa due to its proximity to the throat of the nozzle. The outlet gage pressures were set based off of the desired pressure ratio for each case. The turbulent viscosity ratio is the ratio of the turbulent to laminar viscosity specified on the boundary. The downstream section is supposed to represent the far-field



conditions, therefore the ratio was changed to 1 instead of kept at 10. The reference location was the inlet with all of the unchanged until after the solution converged.

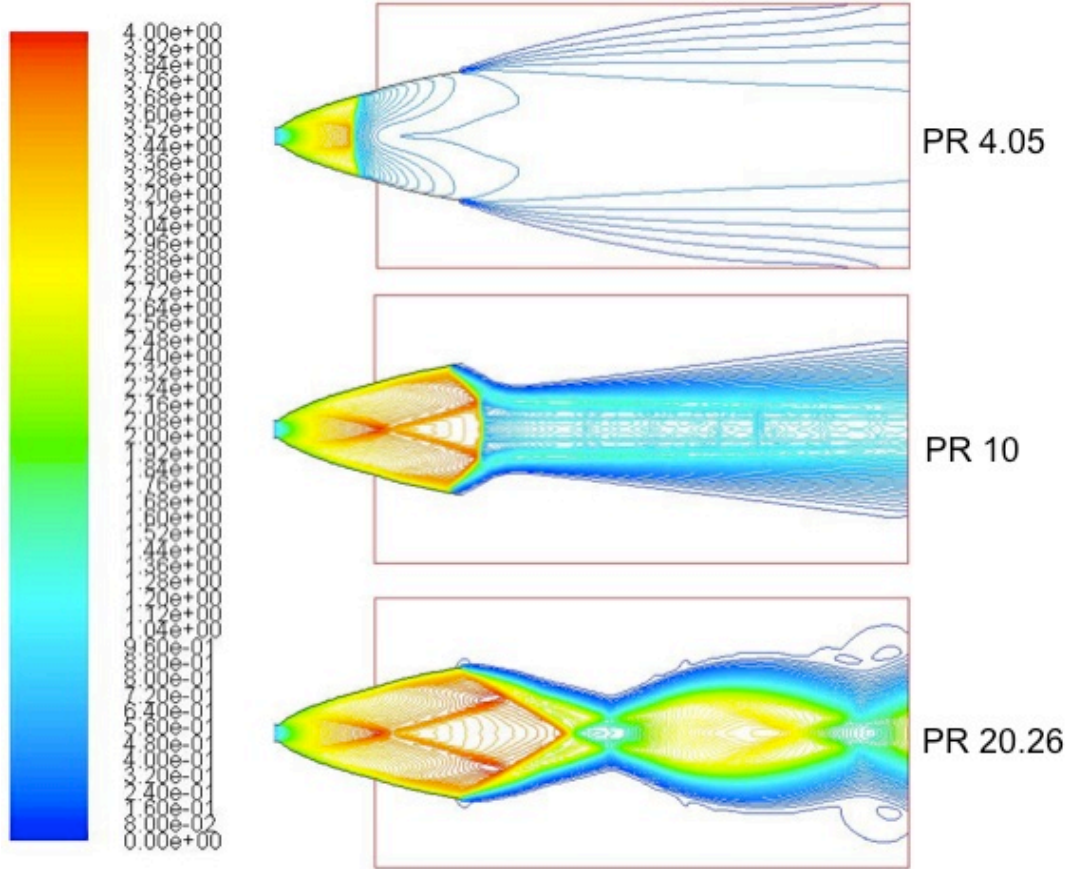
Each case initiated iterations using a Courant number of 0.1 and a first-order upwind scheme until the solution converged. Then, without reinitializing the solution, the scheme was changed to second-order upwind, leaving the Courant number the same, and the calculation was continued. If the residuals remained almost constant for over 15000 iterations, the courant number was increased. Increasing the courant number increased the time step, and would not negatively affect the solution because the finite volume scheme that Fluent uses is implicit [22]. Allowing the first-order solution to converge provided the solver with a better initial guess of the solution than just using the original inlet and outlet boundary conditions, and helped prevent deterioration of the solution along the outermost edges of the downstream boundary in all but one case.



**Figure 46: Dual-bell Mach contours for design point pressure ratios of 150 (top) and 1000 (bottom)**

The design points for the dual-bell nozzle, where perfectly expanded flow is expected for each, were both over-expanded. The top Mach contour in Figure 46 shows the dual-bell nozzle Mach contour with a pressure ratio of 150 and the bottom shows the Mach contour for the pressure ratio of 1000. Apart from the free stream separation, FSS, formation stemming from the throat, another very mild flow feature appears to come off the wall from the beginning of the second bell. FSS is the flow phenomena in parabolic nozzles where a shock stems from the throat and exits the nozzle without reattaching to the nozzle wall. The waves cross one another downstream of the nozzle and meet the right side of the boundary. Both cases have expansion waves at the exit of the nozzle, meaning they are under-expanded. The first case should be over-expanded in the first bell with a pressure ratio of 150, and perfectly expanded in the second bell with a pressure ratio of 1000. The over-expansion in both cases could be caused by boundary layers preventing full expansion of the flow until after it reaches the exit. A result of this is that the average pressure over the nozzle exit plane would be higher than the expected 101.3 Pa. The mass-averaged pressure over the nozzle's exit for both cases is 1150 Pa. Furthermore, the full plume from the nozzle is not seen in the downstream section, which suggests that future work could involve modeling the same case with a larger downstream section.

Three over-expanded cases, shown in Figure 47, converged with pressure ratios between 4 and 50. The case with smallest pressure ratio that converged had an ambient pressure of 25000 Pa, which is equivalent to a pressure ratio of 4.05. All of the cases that converged had varied levels of FSS starting just after the throat. The shocks never re-attach to the nozzle walls, which is important in order to avoid shock heating and side loads. The over-expanded cases show how oblique shocks regress into the nozzle becoming a normal shock at the exit plane and eventually moving back towards the throat.



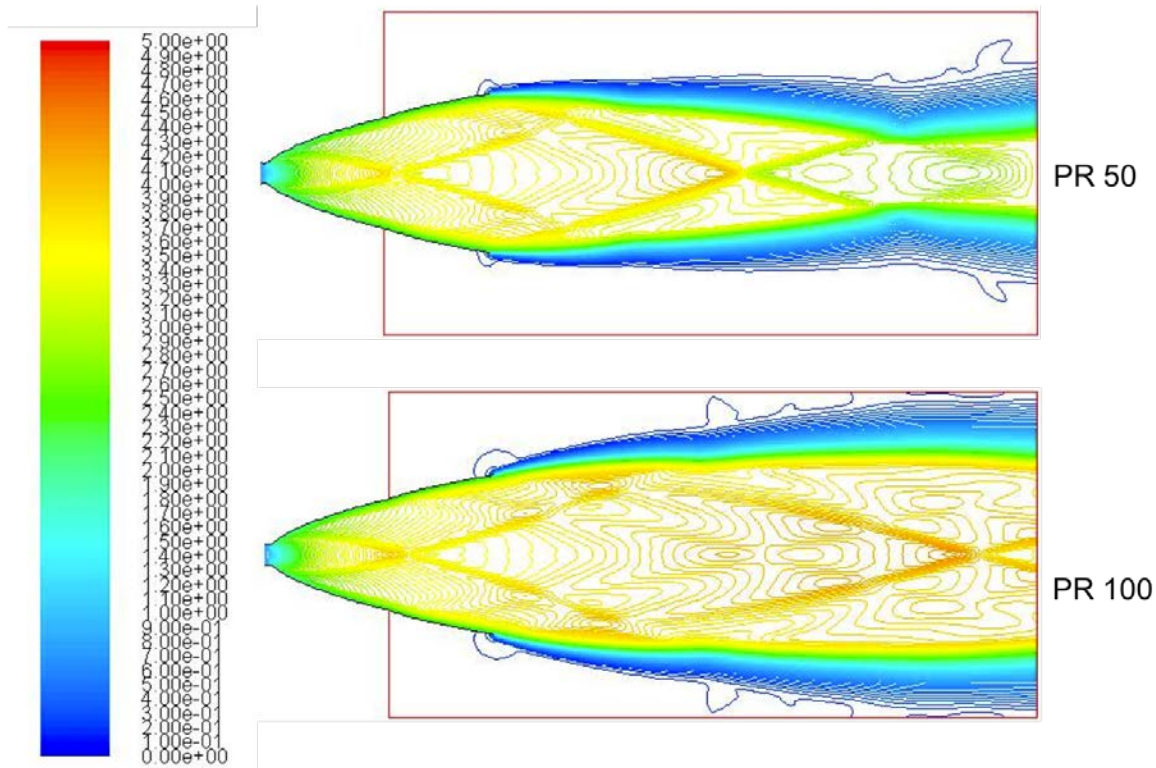
**Figure 47: Dual-bell Mach contours for pressure ratios of 4.05, 10, and 20.26 in order from top to bottom**

Figure 47 shows three over-expanded dual-bell nozzle Mach contours for pressure ratios between 4.05 through 20.26. The largest Mach number among the three cases is 3.98, which is reached with a pressure ratio of 20.26. The maximum Mach number for the critically over-expanded case, the top of Figure 47, is about 3.5 and occurs for a pressure ratio of 4.05. The flow remains supersonic at the throat and about three quarters of the way down the first bell before being slowed by a normal shock. The flow becomes subsonic after the shock and remains subsonic throughout the flow up to the exit boundary. With this pressure ratio, a normal shock is expected where the radius of the nozzle is equal to about 6.1 cm, or about 5.5 cm axially downstream of the nozzle throat, well before the start of the second bell (Appendix E). The

shock is located a little further down the nozzle, most likely due to boundary layer effects preventing full expansion until further downstream.

In contrast to the previous case, the middle image in Figure 47 shows the Mach contour for a pressure ratio of 10, where a normal shock is located just beyond the exit plane of the nozzle. Furthermore, the flow separates just before the end of the nozzle forming to small oblique shocks that connect to the normal shock. The maximum Mach number for the pressure ratio of 10 is 3.8, and is reached just upstream of the shock and where the oblique shocks from the FSS meet along the centerline of the nozzle.

Two oblique shocks originating at the edge of the nozzle connect downstream of the exit in the Mach contours for the 20.26 pressure ratio case in the bottom of Figure 47. The shocks slightly over-compress the flow, causing a rebounding expansion fan leading to another oblique shock after the initial connection, creating a Mach diamond. This is a realistic and expected effect, and the maximum Mach number in the second diamond, about 2, is significantly less than that coming out of the nozzle, about 4. If there were a larger downstream section, the Mach diamonds would theoretically get weaker and weaker until they disappear.



**Figure 48: Dual-bell Mach contours for pressure ratios of 50 (top) and 100 (bottom)**

The top image in Figure 48 shows the case where the pressure ratio was set to 50. Oblique shocks originate at the edge of the nozzle at a very slight angle from horizontal, barely compressing the flow. The beginning of a Mach diamond formation appears to form after the oblique shocks meet downstream of the nozzle. However, the downstream section ends before a full diamond could form. The lower contour in Figure 48 was the case where the pressure ratio was 100. This case is slightly under-expanded in the first bell, as can be seen from the flow features starting at the inflection point.

### **5.3.3 2-D Simulation of Rao Wind Tunnel Contours**

During Fluent evaluation of the wind tunnel contours, the Rao cases and the dual-bell cases were tested in the same way. Each of these evaluations was two-dimension, but was not axisymmetric; the flow was bounded on the top and bottom by walls. The convergence criteria

were kept as the Fluent standard:  $1e-3$  for all residual values. In addition, the same mesh for each case was used throughout the testing. The only equations active were the energy equation and the standard k-epsilon turbulence model. Included in the turbulence models is the no-slip condition for walls. The fluid equation of state was the standard ideal-gas model for air included with Fluent. The inlet pressure was set to 101325 Pa (1 atm), while the exit pressure was varied. During testing, the Courant number was changed to accelerate convergence. Every case started with a Courant number between 0.5 and 1.0, which was raised with each subsequent iteration period. The standard iteration period was 15000 or 30000 iterations for the dual-bell and Rao cases respectively. All other factors were held constant throughout testing.

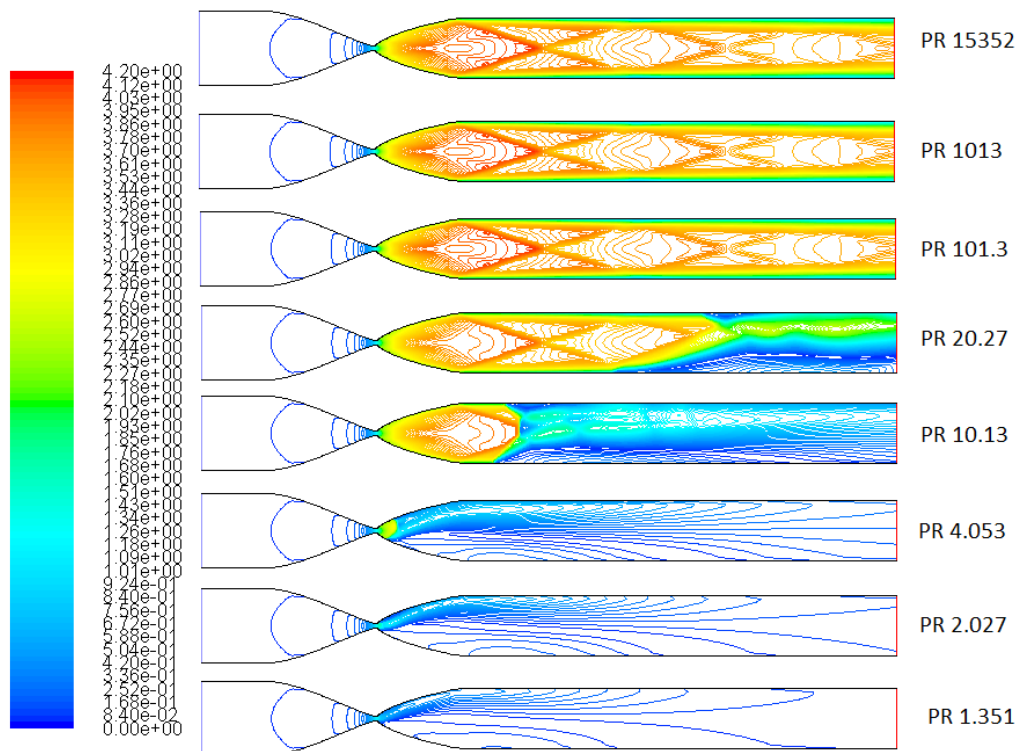
There were certain cases that would not converge in a reasonable amount of time or returned anomalous results. For these cases, a slightly different procedure was followed. First, the test was run with first-order solutions to get a general idea of the flow pattern. Once that solution was achieved, the flow equations were changed to second-order solutions to get a more detailed image of the flow. This saved a considerable amount of computational time and lead to more accurate results.

For the Rao nozzle testing, a variety of back pressures were chosen to create a time-lapse series of snapshots of the flow field through the contours. As the flow passes through the wind tunnel, the back pressure rises, which changes the pressure ratio. After consideration of critical points (e.g. the design back pressure, the design pressure for the inflection point, the back pressure for unchoked flow), a pseudo-logarithmic scale was chosen for the back pressures over the range of back pressures present during testing. These values are listed in

Table 10 below.

**Table 10: Summary of Convergence and Mass Flow Error for Rao Wind Tunnel Contour Cases**

Back Pressure (Pa)	Number of Iterations to Convergence	Percentage Error in Mass Flow Rate
6.6	13440	0.381%
100	13420	0.452%
1000	13640	0.462%
5000	16600	1.901%
10,000	59120	1.420%
25,000	31360	0.049%
50,000	28440	5.225%
75,000	31340	0.874%



**Figure 49: Comparison of Mach Contours at Varying Back Pressures in Rao Nozzle Wind Tunnel Contour**

The flow structures are very similar between the cases with the pressure ratios of 15352, 1013, and 101.3, as can be seen in Figure 49. This is to be expected, as the flow is nowhere near the pressure ratio (approximately 1.9) at which it would become unchoked. The flow is supersonic all the way to the exit plane of the contour, but there are Mach diamonds extending the length of the nozzle. These structures indicate where the flow reaches its peak Mach number of 4.13. As the flow continues down the post-nozzle section, the boundary layers grow, which in turn slows the flow down to the exit Mach number of 3.6 at the exit plane of the test section. The flow is marginally slower in the case with a back pressure of 100 Pa, but this difference is negligible.

As the wind tunnel test continues to run, more interesting flow features begin to appear. For the case with a pressure ratio of 20.27, an oblique shock pattern appears. It is not a normal shock because the flow does not drop to subsonic speeds after the shock. However, the Mach diamonds do break down at this back pressure as the boundary layer grows more dramatically. While this flow was predicted to be symmetric, it appears to be severely asymmetric. This is most likely due to the shock structure moving up the wind tunnel test section. This motion is also responsible for the mass flow rate discrepancy. For this case, the mass flow rate was off by nearly 2%, which is possibly significant. It is within expected error margins, however.

The shock continues to move up the contour as the back pressure rises. The downstream flow pattern for the pressure ratio of 10.13 is very interesting. After the shock, there is still a small section of supersonic flow, but it is not axisymmetric. This is most likely due to a chaotic turbulence interaction. If the flow could be pictured in motion, it would see-saw back and forth inside of the wind tunnel, but the results show a snapshot. The flow should move up and down in the wind tunnel.



Once the pressure ratio drops to 4.053, the shock has disappeared. The pressure gradient does not allow for a shock beyond this point. However, a small region in the flow becomes supersonic just downstream of the throat. This region ends a quarter of the length downstream of the nozzle. The flow is grossly under-expanded for the final three cases. In fact, all three of these cases are relatively similar. They all show a static image of a flow that should be bouncing back and forth. However, this is contrary to the expectation of symmetric flow. This discrepancy is one that could have a few different causes, including small geometry errors, chaotic turbulence effects, or something within the solver of Fluent.

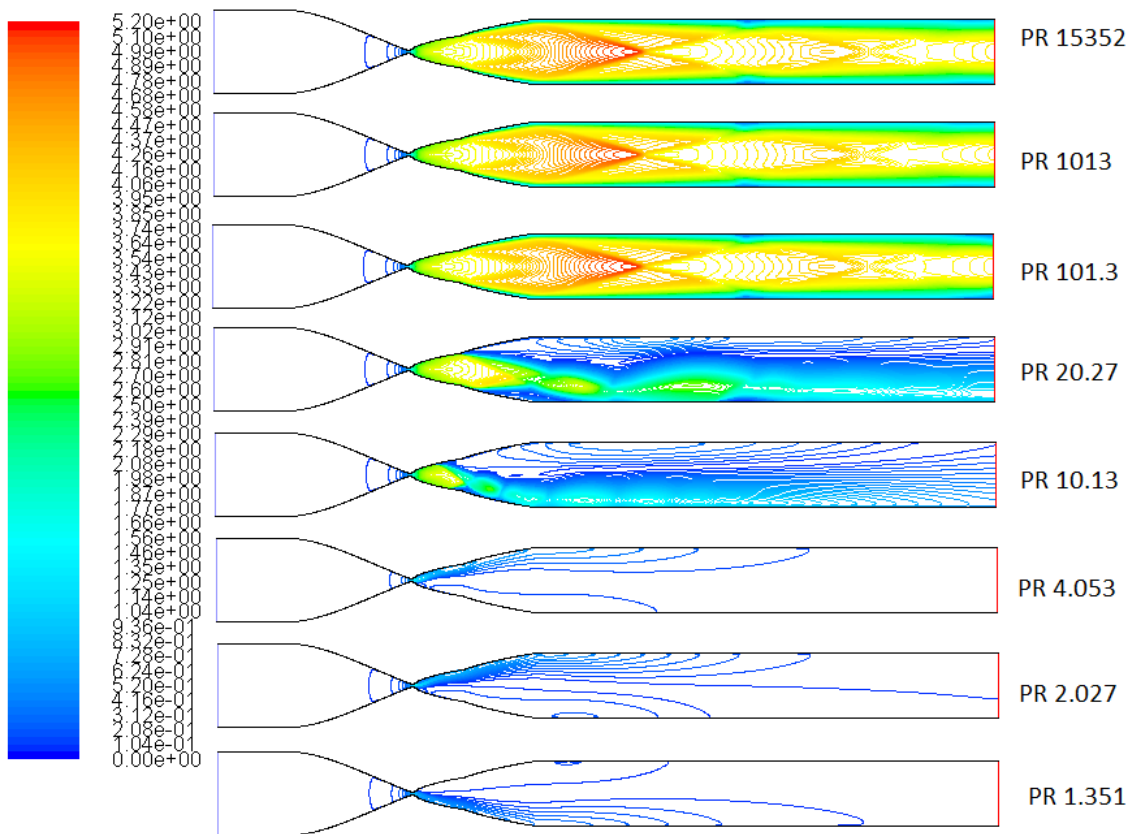
As the back pressure rises, the flow continues to slow down. The maximum Mach number for a pressure ratio of 2.027 is only 1.8, and the flow is not supersonic all the way across the throat. This is somewhat expected, as the critical pressure ratio for choked flow is 1.893, very close to the pressure ratio for this case. In addition, the presence of boundary layers reduces the effective nozzle throat area, increasing the velocity of the flow. The 1.351 case has effectively the same results as the 2.027 case, but with a slower flow. However, the 1.351 case should be unchoked flow. This is most likely due to a Fluent error.

#### **5.3.4 2-D Simulation of Dual-Bell Wind Tunnel Contours**

For the dual-bell nozzle, the same back pressures were used as in the Rao testing cases. This was done to improve comparability between cases. One key note about the dual-bell nozzle is the fact that the nozzle throat is approximately one-half the height of the Rao nozzle. This was done to better simulate the pressure ratios present in the full-scale nozzle. As the exit height of the wind tunnel is fixed, the only option was to reduce the height of the throat. Again, the goal of the dual-bell testing was to create a rough, time-lapse picture of the flow structure as a function of back pressure. Some comparison details between the cases are detailed in Table 11 below.

**Table 11: Summary of Dual-Bell Contour Testing**

Back Pressure (Pa)	Number of Iterations to Convergence	Percentage Error in Mass Flow Rate
6.6	129600	0.079%
100	19980	0.349%
1000	26640	0.315%
5000	44580	2.231%
10,000	108020	0.079%
25,000	44260	0.576%
50,000	154420	0.093%
75,000	154860	0.068%



**Figure 50: Comparison of Mach Contours for the Dual-bell Contours**

The flow structures for the first three back pressures are again very similar. Again, there is a Mach diamond structure that starts just beyond the exit of the nozzle. However, the maximum Mach number is 5.1 for each of these cases. This is to be expected for this case, as the throat area was reduced, resulting in a larger expansion ratio. One interesting feature of these flows is the very small subsonic region about two nozzle lengths downstream of the end of the nozzle. This feature truncates the Mach diamonds. The reason for this structure is unclear, but it could be an artifact of the dual-bell contour as it does not appear in the Rao testing cases. For these pressure ratios, the second bell will be in use; that is, the flow will fully expand into the second bell of the nozzle.

The flow structure in the nozzle begins to break down once the pressure ratio reaches 20. In this flow, there are bubbles of supersonic flow in a narrow jet. This jet is axisymmetric, but due to friction effects, the actual flow is shifted downward. The flow is completely full in the first bell nozzle, but then the flow separates in the second bell.

This flow “breakdown” continues, albeit in a slightly different pattern, as the pressure ratio continues to fall. When the pressure ratio reaches 10, the flow has become over-expanded. At this point, the flow should be free to see-saw in the wind tunnel. As before, the fact that these are snapshots, limit how effectively the images capture what is going on as the pressure changes. One interesting point is the fact that the Mach number remains relatively high at this pressure ratio. The maximum Mach number is approximately 3.8, or almost as fast as the unrestricted flow in the Rao contours. Within the over-expanded flow, there are small Mach diamond-esque structures.

However, when the pressure ratio falls to 4, the Mach pattern breaks down and disappears. In addition, the Mach number falls to less than 2. The flow is even more grossly

over-expanded for this case. The final two test cases are fairly similar to the previous test case. Both flows are non-symmetric and effectively subsonic. The maximum Mach number for the 75000 case is only 1.2 and is only reached in a localized region of the throat. The flows are unchoked; however, the mass flow rates are the same as the choked flow rates. This discrepancy was noted and do impact the results. However, the flow should be very close to choked, lending veracity to the idea that the mass flow rate is off by a small amount.

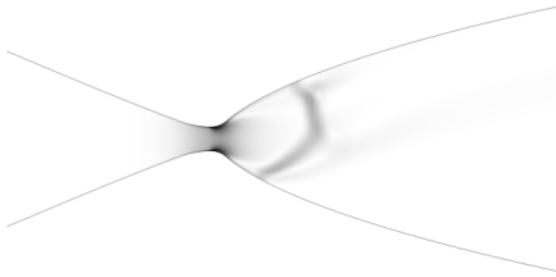
## **6 Analysis and Discussion**

The flow structures imaged in tests using the dual-bell contours are consistent with those obtained through Fluent analysis of the dual-bell wind tunnel contour. Using the CFD-Post subsection of ANSYS Workbench 14.5, a plot of the density gradients was created. As this is what we see in schlieren imaging, these results are directly comparable as qualitative data.

### **6.1 Comparison of CFD and Schlieren Results**

#### **6.1.1 Rao Nozzle Results**

During the initial stages of the test, both images (CFD-generated pressure gradient and schlieren) are very similar, with very small density gradients. This is to be expected as this flow is laminar and undisturbed. As the test progresses, a shock wave moves upstream in the test section, immediately followed by a turbulent flow. This can be seen in Figure 51 and Figure 29. As the test continued, the shock wave progressed upstream in the test section into the nozzle. This can be seen between Figure 51 and Figure 52 (where Figure 52 is chronologically first). Due to the limits of the Fluent testing (the Fluent simulations were not performed at every back pressure), this flow feature was lost in the “time” gap between tests. To create Figure 51, surface plots were created using CFD-Post, an adjunct to the ANSYS Workbench software. Each image had 200 contour levels. The colormap used is the standard inverse grayscale scheme. The range of values for the density gradient were automatically determined by CFD-Post and were left as the full range present in the entire wind tunnel structure, from inlet to outlet flange.



**Figure 51: Fluent "schlieren" image at a pressure ratio of 4.**

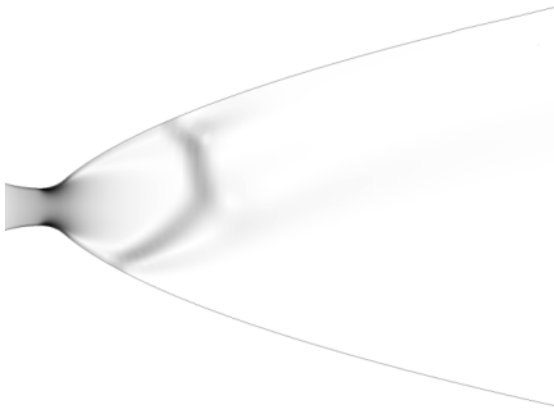


**Figure 52: Shock wave imaged using Fluent "schlieren" settings at a BP of 10.**

Once the shock wave reached the throat of the nozzle, downstream effects became readily apparent. One interesting feature of this shock is the shape. While it is an oblique shock, there is a small section of the shock that is perpendicular to the test section walls. However, the Fluent results show that the oblique shocks angle upstream from the perpendicular section, while the physical testing indicates that the oblique shocks angle downstream. This is possibly due to a flaw in the boundary conditions of the Fluent model at the walls of the test section.

Downstream of the shock, both flows have asymmetric flow features. In the wind tunnel testing, these take the form of bright circular spots, as highlighted in Figure 31. These flow features continue to form after the shock disappears from the schlieren image. The first spot

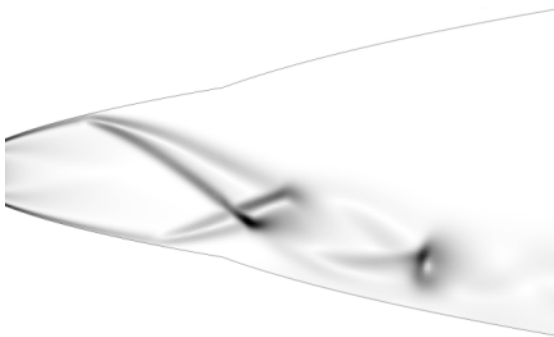
remains relatively steady, but subsequent spots follow a “line” up to immediately behind the first, whereupon they also remain steady. This feature was captured in a preliminary form in the Fluent plots. In Figure 53, there is a bright patch immediately downstream of a shock wave. This appears to be the genesis of the bright circular spots.



**Figure 53: Genesis of the flow features in the Rao test section.**

### **6.1.2 Dual-Bell Results**

The most distinctive result from the dual-bell testing was the imaging of the boundary layer flow features, as seen in Figure 54. These features acted almost identically to the flow features present in the Rao nozzle; that is, each subsequent feature started near the exit of the nozzle and moved upstream to immediately behind the next feature upstream.



**Figure 54: Fluent "schlieren" imaging at a pressure ratio of 10.**

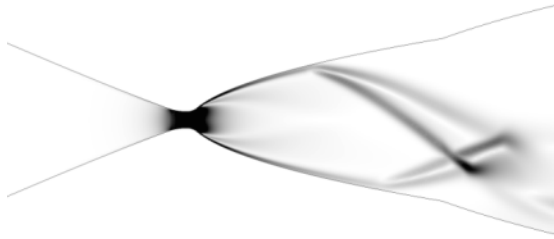
The bright spots were not as clearly imaged in the Fluent testing. In Figure 55, a distinct region of high density gradient is clearly seen along the path of the flow features. However, it is mirrored vertically. With that said, the jet does switch from top to bottom over the course of the Fluent test cases. This is potentially due to a boundary layer effect that was not accounted for in the simulation equations. This “switching” behavior was not seen in the physical experimental results.



**Figure 55: Fluent "schlieren" image at a pressure ratio of 4.**

However, in the broader picture, the flows are very similar. Compare Figure 56 and Figure 34. The primary feature to notice is the sloping dark line sweeping from just downstream of the throat to the inflection point. This shock is also present in the Fluent results. At the next pressure ratio for the Fluent test, the shock had disappeared (see Figure 55), which was also the behavior observed in the experiments.





**Figure 56: Fluent "schlieren" image at a pressure ratio of 10.**

## **6.2 Full-Scale Nozzle Performance Comparison**

In a qualitative comparison, the full-scale conventional nozzle analyzed with Fluent performed similarly to the dual-bell nozzle in terms of the downstream behavior. The design pressure ratio of the conventional contour was 102, and like the dual-bell nozzle, it showed over-expanded behavior at the design pressure ratio, even though perfectly expanded behavior was expected based on isentropic flow relations. The main difference between the two contours can be seen in the internal flow structures. The flow within the conventional contour differed from the dual-bell nozzle in that there was only boundary layer separation within the nozzle. No secondary flow structures formed, and the core flow was smooth as it reached the exit for the design point case. The only extra core structures within the flow occurred in the under-expanded case where an oblique shock from the nozzle's edge met the core flow causing minor disturbances downstream that carried through into the Mach discs.

The average specific impulse, for these cold flow cases, was calculated over a range of back pressures using the mass averaged pressure and velocity from Fluent post-processing over the nozzle's exit plane. The mass averaged values were used instead of area-averaged values because the difference was negligible. Fluent computed the mass averaged pressure and velocity

over the nozzle outlet for both the dual-bell and Rao nozzles. These values were input into the rocket thrust equation to calculate the theoretical thrust produced by each nozzle and the specific impulse was calculated using the thrust and mass flow rate. The thrust,  $T$ , which the nozzle produced was calculated using the ideal thrust equation.

$$T = \dot{m}u_e + (p_e - p_a)A_e \quad 21$$

where  $\dot{m}$  is the mass flow rate,  $u_e$  is the exit velocity,  $A_e$  is the exit area and  $p_e$  and  $p_a$  are the exit pressure and ambient pressure respectively. The specific impulse,  $I_{sp}$ , was calculated by dividing the thrust by the mass flow rate,  $\dot{m}$ , and Earth's gravitational constant,  $g_0$ , for each case and then averaging over the four cases. These calculations assumed a range of pressure ratios from 1.4 to approximately 15000, with a chamber pressure of 1 atm. The temperature was 300K and air (molar mass of 28 kg/kmol) modeled as an ideal gas was the working fluid.

$$I_{sp} = \frac{T}{\dot{m}g_0} \quad 22$$

Table 12 and Table 13 summarize the parameters for the dual-bell and Rao nozzles.

**Table 12: Dual-bell nozzle specific impulse calculation parameters**

PR	Pe (avg) (Pa)	Ve (avg) (m/s)	Thrust (N)	Isp
1000	1147	655	499	70.233
150	1147	656	492.3	69.293
100	1147	656	484.4	68.183
50	1150	655	449.8	63.302
20	1177	653	385.2	53.479
10	3316	587	258.5	36.377
4	24448	216	142	20.124

**Table 13: Rao nozzle specific impulse calculation parameters**

PR	Pe (avg) (Pa)	Ve (avg) (m/s)	Thrust (N)	Isp
15352	4472	593	594.947	85.868
1013	4472	593	594.947	85.868
10	4517	592	298.159	43.033
4	4902	586	-435.784	62.896
2	4839	587	-358.215	51.700
1.4	61632	228	155.661	22.466

The negative thrust values are unrealistic results that were produced by Fluent. Both of the cases with negative thrust values had a normal shock at the end of the nozzle. The algebraic average specific impulse was 64.9 s for the dual-bell contour and 71.6 s for the conventional contour nozzle. The averages were only taking into account the cases that did not have a normal shock in or at the exit plane of the nozzle. The  $I_{sp}$  values were comparing the simulated flow features for each nozzle. The Rao nozzle was optimized for a considerably lower pressure ratio than the dual-bell. The dual-bell contour did not perform as well as the conventional nozzle contour. This could be due to the location of the inflection point on the dual-bell contour, to the optimal pressure ratio for each inflection, to boundary layer growth, or a combination of all three.

### **6.3 Physical Interpretation**

The high contrast structures in both the schlieren images and Fluent wind-tunnel simulations are consistent with expected shock structures in a high speed nozzle. The structures are more developed farther along the flow field in the Fluent simulation than in the schlieren images, likely due to non-orthogonality in the alignment of the optical system with the wind

tunnel test section. The round light regions that appear in the schlieren images and correspond to a similar density gradient in the Fluent simulations are a boundary flow structure of some kind. The dark streaks seen in the schlieren images could potentially represent oblique shocks, the reflections and interference of which result in the small, constant-density regions, which were manifested as the round light regions.

## **7 Conclusion and Recommendations for Future Work**

### **7.1 Conclusion**

This project addressed a common issue in nozzle design and its effect on the efficiency of rocket engine systems. A dual-bell nozzle contour design procedure was developed and used to investigate a possible nozzle that could be implemented on a sounding rocket or other form of a nanosatellite launch vehicle. The contour was adapted for physical testing in a supersonic wind tunnel in conjunction with a schlieren optical system. This system captured images of normal and oblique shock structures and boundary layer flow features in both the Rao and dual-bell nozzles.

Schlieren imaging of flow in the tunnel showed oblique shock structures and boundary layer flow features. Analysis of the dual-bell contour in both configurations was performed using ANSYS Fluent simulations, and similar simulations were run for a conventional contour. This was done to compare flow structures within the proposed dual-bell contour to those of a conventional nozzle contour as well as to compare their performance characteristics. The conventional nozzle contour performed better than the proposed dual-bell contour over a range of backpressures, with an average (cold flow) specific impulse of 71.6 s compared to the dual-bell's 64.9 s. Future investigations should focus on changing the location of the inflection point within the nozzle as well as optimizing the design point pressure ratios. Mach contours generated from the Fluent simulations show similar flow features to the schlieren images from the wind tunnel testing indicating that the Fluent simulations are both valid and robust for this application.

## 7.2 Recommendations for Future Work

The geometry of the dual-bell contour in the wind tunnel produced supersonic speeds but could have been improved through a more perfect sealing process. The O-rings were sealed tightly using vacuum grease but there was a leak from the space in between the endplate and bracket. The silicon used to seal these two pieces did not create a tight enough fit. This leak meant that the vacuum chamber could not be pumped down as far, 17 milliTorr rather than 3 milliTorr, shortening the usable test time. A better sealing process or sealant could ensure a more accurate flow for comparison with CFD results.

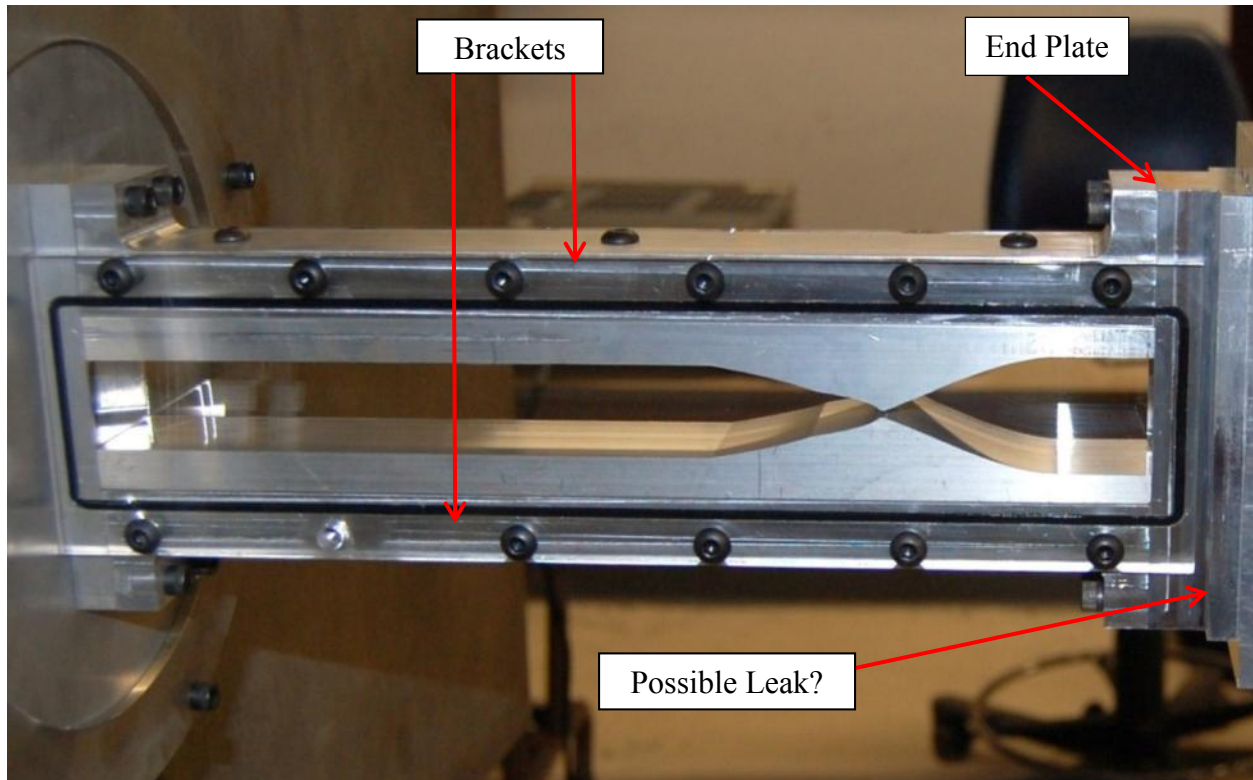


Figure 57: Wind Tunnel with Dual-Bell Contours Installed

This project focused on the presence of an inflection point and two area ratios, but not the location or shape of the inflection. Future testing could compare performance as the inflection

point is moved toward the back of the nozzle. Similarly, a study of the flow structures coming off of differently shaped (sharper or smoother) inflection points could improve performance.

In addition to schlieren images, pressure and velocity data could be gathered. Adding pressure taps with Pitot probes on one side of the contour would allow for pressure measurements along the test section.

This group calculated the wind tunnel run time based on varying throat diameters, but a full back pressure versus run time calculation would facilitate comparison with the CFD results. Knowing the backpressure vs. time (for example by collecting chamber pressure data during a run), schlieren images and numerical data could be precisely aligned, enabling more accurate comparison with Fluent results.

This group performed Fluent simulations using a steady-state (stationary solution) approximation simplifying each case by assuming it corresponded to a single pressure ratio. The next step to improve the simulation accuracy is to run transient cases covering the whole range of expected pressure ratios. These simulations would require a pressure trajectory profile for the rocket's flight. A code detailing backpressure vs. altitude data needs to be added to Fluent through a journal file in order to create a user defined function. This would then be implemented to perform the transient calculation.

A time dependent simulation would enable a better performance comparison between dual-bell and Rao contours throughout every pressure ratio, and a trajectory averaged specific impulse value could be calculated. This case comparison (transient dual-bell compared to transient Rao nozzle with trajectory information) would either validate or disprove whether or not the dual-bell nozzle is effective.

A new Rao contour should be created that is optimized for a higher altitude (the current nozzle is optimized for sea level operations) in order to obtain a more accurate comparison between the dual-bell nozzle and the Rao nozzle performance.



## 8 References

- [1] ÖSTLUND, J. 2002. *Flow Processes in Rocket Engine Nozzles with Focus on Flow Separation and Side-Loads*. Royal Institute of Technology.
- [2] HAGEMANN, G., IMMICH, H., NGUYEN, T. V. & DUMNOV, G. E. 1998. Advanced rocket nozzles. *Journal of Propulsion and Power*, 14,620-634.
- [3] NÜRNBERGER-GENIN, C. & STARK, R. 2009. Flow transition in dual bell nozzles. *Shock Waves*, 19, 265-270.
- [4] NASUTI, F., ONOFRI, M. & MARTELLI, E. 2005. Role of wall shape on the transition in axisymmetric dual-bell nozzles. *Journal of propulsion and power*, 21, 243-250.
- [5] SUTTON, G. 2010. *Rocket Propulsion Elements*, Wiley.
- [6] KULHANEK, S. 2012. *Design, Analysis, and Simulation of Rocket Propulsion System*. Master of Science, University of Kansas.
- [7] VERMA, S. B., STARK, R. & HAIDN, O. 2012. Gas Density Effects on Dual-Bell Transition Behavior. *Journal of Propulsion and Power*, 28, 9.
- [8] HAGEMANN, G. & FREY, M. 2008. Shock pattern in the plume of rocket nozzles: Needs for design consideration *Shock Waves*, 9.
- [9] HORN, M. & FISHER, S. Dual-bell altitude compensating nozzles. NASA Propulsion Engineering Research Center, 1993. 140-147.
- [10] FREY, M. & HAGEMANN, G. 1999. Critical assessment of dual-bell nozzles. *Journal of propulsion and power*, 15, 137-143.
- [11] JONES, J. E. 2013. Nanolaunch 1200. NASA-Marshall Space Flight Center.
- [12] MOORE, T. 2006. Black Brandt Sounding Rocket Returns to Flight. *CPIAC Bulletin* [Online], 32.
- [13] SETTLES, G. S. 2001. *Schlieren and Shadowgraph Techniques: Visualizing Phenomena in Transparent Media*. Heidelberg, Germany: Springer-Verlag Berlin Heidelberg.
- [14] NÜRNBERGER-GÉNIN, C. & STARK, R. 2010. Experimental Study on Flow Transition in Dual-Bell Nozzles. *Journal of Propulsion and Power*, 26, 6.
- [15] STARK, R., BOHM, C., HAIDN, O. J. & ZIMMERMANN, H. 2006. Cold Flow Testing of Dual-Bell Nozzles in Altitude Simulation Chambers. *European Conference for Aerospace Sciences*. DLR, German Aerospace Center.
- [16] AULD & SRINIVAS 2006. A Body Placed in Subsonic and Supersonic Flows. *Aerodynamics for Students*.
- [17] NASA GLENN RESEARCH CENTER 2000. Boundary Layer.
- [18] 2007. *Families of Turbulence Models* [Online]. Available: <http://www.innovative-cfd.com/turbulence-model.html> [Accessed 09/26/2013].
- [19] RUMSEY, C. *Turbulence Modeling Resource* [Online]. Available: <http://turbmodels.larc.nasa.gov/> [Accessed 09/26/2013].
- [20] GEORGESCU, A.-M., GEORGESCU, S.-C., BERNAD, S. & COȘOIU, C. I. 2007. COMSOL Multiphysics Versus Fluent: 2D Numerical Simulation of the Stationary Flow Around a Blade of the Achard Turbine. *3rd Workshop on Vortex Dominated Flows* 52(66), 10.
- [21] AKIN, J. E. 1994. *Finite Elements for Analysis and Design*, San Diego, CA, Academic Press Limited.
- [22] Fluent 2005. Introductory Fluent Notes. In: CENTER, F. U. S. (ed.).

- [23] MOIN, P. & MAHESH, K. 1998. Direct Numerical Simulation: A Tool in Turbulence Research. *Annual Review of Fluid Mechanics*, 40.
- [24] MATHEW, J. 2010. Large Eddy Simulation. *Defence Science Journal*, 60,8.
- [25] SPALART, P. R. 2009. Detached-Eddy Simulation. *Annual Review of Fluid Mechanics*, 24.
- [26] DURBIN, P. P.-R., B. A. 2010. Statistical Theory and Modeling for Turbulent Flow. 2nd ed. Hoboken, NJ, USA: Wiley
- [27] BUGDEN, W., FITTON, K., FOLINAS, G., FOURNIER, N., HOGAN, G., ITO, M., LAMBERT, J., PATEL, N., SHIN, D.-U., WONG, G. & ZIEGLER, E. 2013. Design and Construction of a Supersonic Wind Tunnel with Diagnostics Worcester, Massachusetts: Worcester Polytechnic Institute.
- [28] COMSOL. 2013. *Multiphysics Simulation Software* [Online]. [Accessed September 30, 2013].
- [29] NESMEN, T. (2001). *Fluctuating Pressure Data from 2-D Nozzle Cold Flow Tests (Dual Bell)*. Paper presented at the STD Fluids Workshop 2001, Marshall Space Flight Center
- [30] KRUGER, & VINCENTI. (1965). Introduction to Physical Gas Dynamics. New York, New York: Wiley & Sons INC

## Appendix A: AIAA Paper

# Experimental and Computational Investigation of a Dual-Bell Nozzle

Kate Davis<sup>1</sup>, Elizabeth Fortner<sup>2</sup>, Michael Heard<sup>3</sup>, Hannah McCallum<sup>4</sup>, and Hunter Putzke<sup>5</sup>  
*Worcester Polytechnic Institute, Worcester, Massachusetts, 01609, USA*

The proliferation of earth orbital missions enabled by nanosatellites, of which CubeSats are the most common, has focused increased attention on low-cost, mobile launch systems. Advanced nozzle design can address the demand for higher booster performance, and has resulted in the investigation of alternate nozzle geometry. A dual-bell nozzle represents a novel approach to this problem by utilizing two theoretically ideal design points over the ascent trajectory instead of just one. The primary focus for this project was to investigate the performance of a representative dual-bell nozzle both computationally and experimentally. First, a dual-bell nozzle was designed which could be used on a representative, nanosatellite launch system with design altitudes of 3 km and 17 km. The nozzle contours were modified to facilitate machining, and incorporated in a supersonic wind tunnel. The dual-bell nozzle fabricated for testing in the wind tunnel had a “first contour” expansion ratio of 1:9.85 corresponding to an ideal design pressure ratio of 134. The downstream, “second contour” had an expansion ratio of 1:19.7 corresponding to an ideal design pressure ratio of 374. The conventional nozzle fabricated for testing in the wind tunnel had an expansion ratio of 1:11.3 corresponding to an ideal design pressure ratio of 102. Imaging of flow structures was achieved using a schlieren optical system. In addition, the computational fluid dynamics program ANSYS Fluent was used to model both a hypothetical, full-scale nozzle as well as the scaled version tested in the wind tunnel. Simulations were performed for full-scale, dual-bell nozzles operating at pressure ratios (chamber to ambient) of 20, 50, 100, 150 and 1000. These results were then compared to a similar conventional nozzle for each case. Preliminary schlieren results indicate that the scale wind tunnel dual-bell contours show flow structures consistent with the Fluent results.

### Nomenclature

a,b,c	=	Coefficients of the parabola defining the nozzles
$A$	=	Nozzle exit area
$g_0$	=	Earth’s gravitational constant; 9.8 m/s <sup>2</sup>
$I_{sp}$	=	Specific impulse
$K$	=	Percentage of the length of an equivalent 15% conical nozzle
$L_n$	=	Nozzle length
$\dot{m}$	=	Mass flow rate
$p_a$	=	Ambient pressure
$p_e$	=	Average pressure over the nozzle exit-plane
$R_e$	=	Exit radius
$R_M$	=	Nozzle radius at the inflection point
$R_N$	=	Radius of the nozzle at the connection between the throat and the first parabola

---

<sup>1</sup> Undergraduate student, Mechanical Engineering Department, Aerospace Program, AIAA Student Member

<sup>2</sup> Undergraduate student, Mechanical Engineering Department, Aerospace Program, AIAA Student Member

<sup>3</sup> Undergraduate student, Mechanical Engineering Department, Aerospace Program, AIAA Student Member

<sup>4</sup> Undergraduate student, Mechanical Engineering Department, Aerospace Program, AIAA Student Member

<sup>5</sup> Undergraduate student, Mechanical Engineering Department, Aerospace Program, AIAA Student Member

$R_t$	=	Nozzle radius at the throat
$T$	=	Thrust
$x_M$	=	Axial position of inflection point
$x_N$	=	Axial position of the connection between the throat and the first parabola
$\varepsilon$	=	Nozzle area ratio
$\theta_e$	=	Nozzle exit angle
$\theta_N$	=	Flow angle at the connection between the throat and the first parabola

## I. Introduction

The goal of the aerospace engineering community is to develop more efficient and reliable methods to transport payloads into orbit. The increasing prevalence of nanosatellites and lack of small payload (<10 kg) launch vehicles combined with the demand for higher rocket performance has led to the critical assessment of rocket engine subsystems. Numerous studies have focused on the exhaust nozzle with the goal of creating the most efficient single-stage-to-orbit (SSTO) launch vehicle possible. This investigation focused on designing and comparing the differences between a dual-bell nozzle and a conventional nozzle computationally and experimentally. A dual-bell nozzle utilizes two theoretically ideal design points over the ascent trajectory instead of one by combining two parabolic contours separated by an inflection. The upstream contour corresponds to the lower altitude design point. Conventional nozzles refer to any nozzle with a single, continuous contour between the throat and the exit, and are optimally expanded at only one altitude.

The dual-bell concept was first introduced in literature in 1949 by F. Cowles and C. Foster, and was patented in the 1960s by Rocketdyne<sup>1</sup>. Research activity was revived in the 1990s, in part due to the development of modern CFD capabilities. Tests at Rocketdyne conducted by Horn and Fisher and in Europe by the Future European Space Transportation Investigations Programme (FESTIP) at the European Space Agency (ESA) confirmed the feasibility of this nozzle design<sup>1</sup>. However, they also demonstrated that real dual-bell nozzles fall short of the theoretical optimum due to losses sustained from aspiration drag, earlier-than-ideal flow separation, and a non-optimal contour for high altitude flight. Even with these additional losses, Horn and Fisher found that a dual-bell nozzle could provide enough thrust to carry 12.1% more payload than a conventional nozzle of the same area ratio<sup>1</sup>.

A dual-bell nozzle has three characteristic geometric features: an inner base nozzle contour, a wall inflection, and an outer extension nozzle contour. At low altitudes, exhaust gases expand in the base nozzle and separate at the inflection point, making the area at the inflection point the effective exit area during this mode of operation. By having controlled, axisymmetric flow separation, side loads are less of an issue than in conventional nozzles because the separation point cannot fluctuate when the nozzle is under-expanded. As the rocket altitude increases, ambient pressure decreases and the exhaust gases need a larger expansion ratio to match, or approach, the ambient conditions. During this operational phase, the flow is attached to the wall of the extension nozzle, and the whole exit area of the nozzle is used. Because of this second section of the nozzle, the flow is not as under-expanded as it would be for a conventional nozzle with the same area ratio as the base nozzle contour. Thus, the dual-bell nozzle achieves improved high altitude performance over single-bell nozzles<sup>2</sup>. Additionally, dual-bell nozzles have the unique benefit among altitude compensating nozzles of having no moving parts.

Schlieren imaging, named after the German word for “streak,” is an optical technique for studying inhomogeneous media. August Toepler was the first to see the motion of shock waves using his schlieren technique. Since then, schlieren techniques have been further developed for various applications<sup>3</sup>. Schlieren systems are considered the standard for high-speed wind tunnel flow imaging, making it a perfect optical technique for this project. Information about the location and shape of shock waves, the location of boundary-layer separation, and areas of wave interference can be seen qualitatively using a schlieren system.

The primary focus for this project was testing a dual-bell contour in an indraft supersonic wind tunnel and testing a hypothetical full-scale nozzle using ANSYS Fluent©. These results were then compared to a conventional nozzle for each case. In addition, Fluent was used to simulate the flow through the supersonic wind tunnel in order to assess the comparability of Fluent results and wind tunnel results. The flow seen in the wind tunnel was found to resemble the flow predicted by Fluent, which confirmed the possibility for an improved specific impulse and thereby an improved payload fraction.

## II. Nozzle Design Methodology

The area ratio of both the full-sized conventional nozzle and dual-bell nozzle was determined using the isentropic flow relations. To size the throat of the nozzle, a thrust for the Black Brandt sounding rocket (the intended launch vehicle) was calculated. A chamber pressure of 1500 psi, given by the characteristics of the Black Brandt sounding rocket, a possible first stage for a CubeSat launch vehicle<sup>3</sup>, was used to determine the pressure ratios (stagnation to

ambient) at different altitudes. The pressure ratios were then back-solved to find Mach numbers and area ratios. The value of the ratio of specific heats was assumed to be 1.23 due to the large assumed pressure and the high temperatures expected inside the combustion chamber of the Black Brandt sounding rocket (a potential application for the dual-bell nozzle)<sup>4</sup>. The conventional nozzle was designed with an initial pressure ratio of 102 with a corresponding area ratio of 11.3 corresponding to an optimized altitude at sea level. The conventional nozzle was ideally expanded at sea level in order to have a full-sized, ideal testing case for a cold flow test. In comparison, the dual-bell nozzle design altitudes were calculated from the launch profile in order to have the most realistic possible results. The dual-bell nozzle's area ratio at the inflection point is 15, and the area ratio at the exit is 64.5. The corresponding pressure ratios are 148 and 1000 for the inflection point and exit respectively. The design altitudes for the dual-bell nozzle are 3.05 km and 16.97 km.

### A. Contour Design

The conventional nozzle is defined by three curves, the length of the nozzle, and the throat radius (Figure 1). The length of the nozzle is determined by

$$L_n = \frac{K(\sqrt{\epsilon} - 1)R_t}{\tan(\theta_e)} \quad (1)$$

where  $K$  is a percentage of the length of a  $15^\circ$  half angle ( $\theta_e$ ) conical nozzle with the same area ratio,  $R_t$  is the throat radius, (found to be  $0.0305 \text{ m}$ )<sup>3</sup> and  $\epsilon$  is the area ratio. In order to define the nozzle further, a coordinate system is defined with the axial ( $x$ ) axis passing through the line of symmetry and the radial ( $y$ ) axis centered at the throat. The first and second curves define the entrance and exit of the throat of the nozzle, and are based on circular curves. The third curve is a parabola and takes the form

$$x^2 = ay^2 + by + c \quad (2)$$

The coefficients  $a$ ,  $b$ , and  $c$ , are determined by the derivatives of the contour at the point where the circle from the throat meets the beginning of the parabola,  $x_N$ , and the length of the nozzle,  $L_n$ . To close the system of equations and solve for the parabolic coefficients, the exit of the nozzle is examined, where  $x$  is equal to the nozzle's length,  $L_n$ . In matrix form, the system is

$$\begin{bmatrix} 2R_N & 1 & 0 \\ R_e^2 & R_e & 1 \\ R_N^2 & R_N & 1 \end{bmatrix} \begin{bmatrix} a \\ b \\ c \end{bmatrix} = \begin{bmatrix} \frac{1}{\tan(\theta_N)} \\ L_n \\ x_N \end{bmatrix} \quad (3)$$

which can then be solved for the parabolic coefficients.

The dual-bell contour adds a second parabola that connects two conventional contours that share the same throat but are optimized for different altitudes (Figure 2). The second parabola defines the second bell section and connects the two contours thereby achieving a greater expansion ratio. The system of equations to solve for the coefficients of the second curve is:

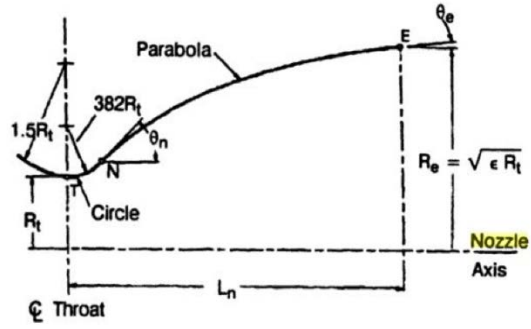


Figure 1: Conventional parabolic nozzle [© Kulhanek, 2012']

The dual-bell nozzle design altitudes were calculated from the launch profile in order to have the most realistic possible results. The dual-bell nozzle's area ratio at the inflection point is 15, and the area ratio at the exit is 64.5. The corresponding pressure ratios are 148 and 1000 for the inflection point and exit respectively. The design altitudes for the dual-bell nozzle are 3.05 km and 16.97 km.

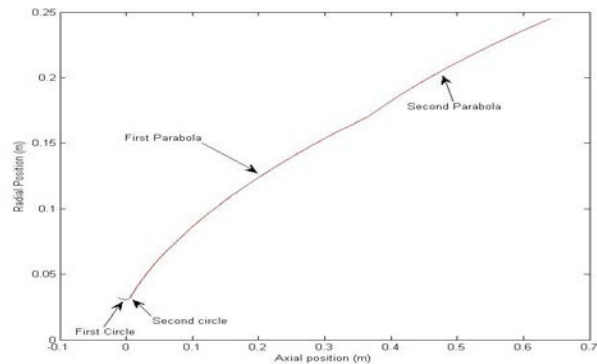


Figure 2: Dual-Bell nozzle with labeled sections (axes scaled for clarity)

$$\begin{bmatrix} 2R_M & 1 & 0 \\ 2R_e & 1 & 0 \\ R_N^2 & R_N & 1 \end{bmatrix} \begin{bmatrix} a' \\ b' \\ c' \end{bmatrix} = \begin{bmatrix} 1 \\ \tan(\theta_M) \\ 1 \\ \tan(\theta_e) \\ x_M \end{bmatrix} \quad (4)$$

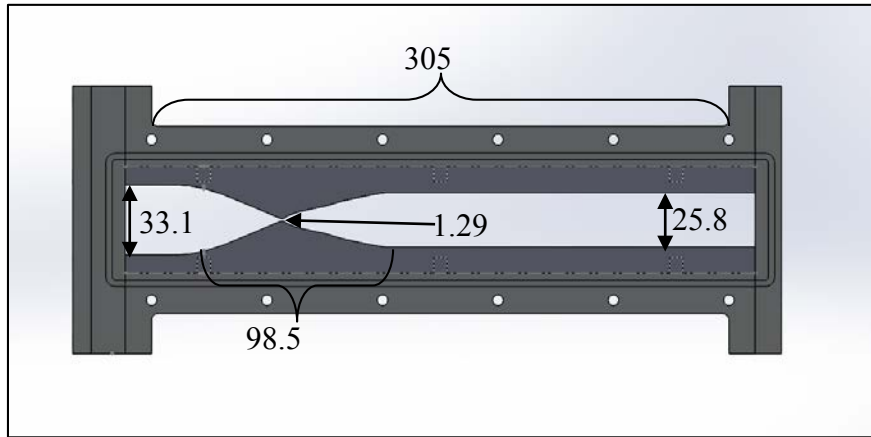
where  $a'$ ,  $b'$  and  $c'$  are the coefficients of the second curve. The final design parameters are listed in Table 1.

**Table 1: Design parameters for the full sized conventional and dual-bell nozzle**

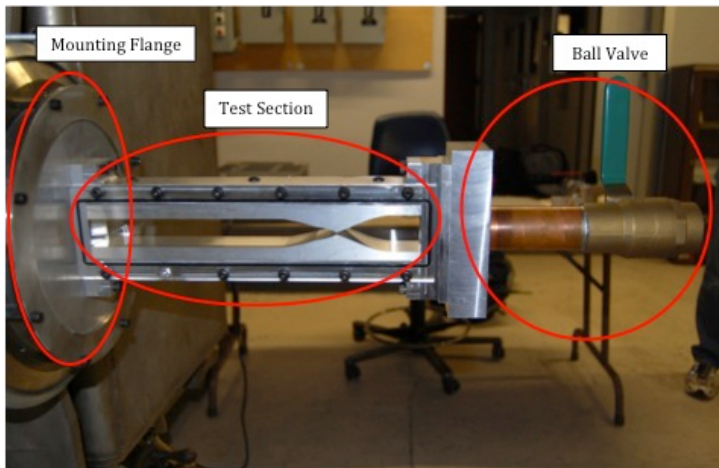
Type of Nozzle	Conventional Nozzle		Dual-Bell Nozzle (First Contour)	Dual-Bell Nozzle (Second Contour)
a	26.0287		10.2859	21.8315
b	-0.5375		0.5084	-4.7223
c	-0.0034		-0.0208	0.5362
Throat Radius (m)	0.0305		0.0305	Shared
Length (m)	0.2150	0.3673	0.2732	
Theta N (degrees)	40.0000	40.0000	20.0000	
Theta e (degrees)	11.9409	14.237	9.5880	
Area Ratio	11.2983	31.4754	64.5603	

### B. Supersonic Wind Tunnel Test Section Design

The nozzle contours, designed for the first stage of a nanosatellite launch vehicle, had to be scaled down to fit the wind tunnel test section. The size of the contours for the Fluent analysis and application are on the order of 0.5 – 1.0 meter in scale, while that of the test section is on the order of inches. In addition to the required dimensional scaling, the contour was also modified to adapt to the 2-D rectangular geometry inherent



**Figure 3: CAD design of the wind tunnel (all dimensions are given in millimeters)**



**Figure 4: Wind tunnel dual-bell test section**

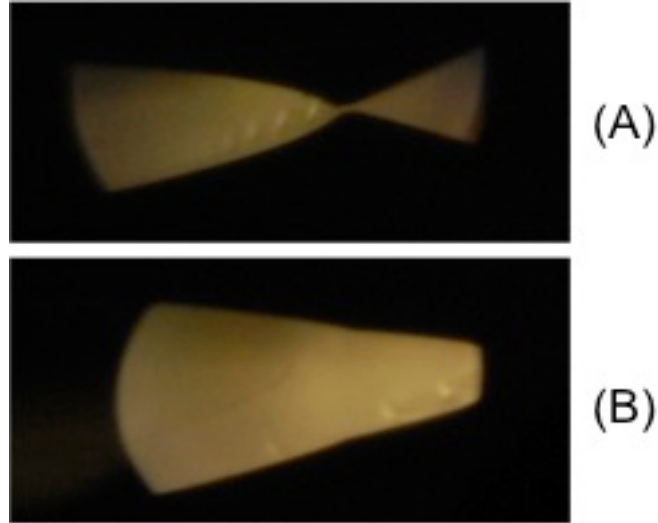
to the test section. Modifying the code developed for the full-size nozzle completed preliminary design. Due to the constraints of the wind tunnel, the exit height of the wind tunnel was fixed to a maximum span of 26 mm. The area ratios of the machined nozzles were modified to be 9.85 and 19.7 for the inflection point and exit of the dual-bell nozzle and 11.3 for the conventional contour. The area ratios of the dual-bell nozzle were changed from their full-scale counterparts in order to keep the throat sizes within machine tolerances. The modified contours were then machined from aluminum blanks.

### III. Wind Tunnel Testing

An indraft wind tunnel test setup was devised to test the nozzle contours that were

simulated with Fluent. The wind tunnel consists of a ball valve, a test section into which contours can be inserted for testing, and a mounting flange that connects the whole system to a vacuum chamber. The valve and flange sections were reused from a previous project group<sup>7</sup>, but the parts in the test section, including the contours, either had to be modified or machined specifically for this project. Two sets of contours were machined: one set with dual-bell geometry, and another set with conventional geometry.

Flow structures in the wind tunnel were visualized using a schlieren-imaging system. Schlieren imaging works on the principle of refraction; parallel rays of light traveling through a homogenous density medium will continue to be parallel, but if parallel rays of light pass through a region where the density of the medium changes, then some of the rays of light will be refracted. In a schlieren imaging system, a series of lenses and mirrors direct parallel rays of light through a test section in which a flow phenomenon occurs. A razor blade cuts off half of the refracted rays of light, enabling a black and white image to be projected on a screen. These images form the qualitative data collected from the imaging system. Schlieren images show the density gradients in the air in the test section of the system: strong gradients appear as dark regions and weak gradients appear as light regions. In order to obtain the best images, the optical components must be precisely aligned.



**Figure 5: Schlieren images for two different tests of the dual-bell nozzle contour**

A schlieren-imaging system was designed by a previous project group<sup>6</sup>, but the system required a redesign and optimization before it was functional. Using an x-channel base so that the components of the system could be easily repositioned, a series of optimization exercises were conducted to determine the best location for each component. The result of this optimization was a set of distances between components and angles between the three different segments of the system. In order to simplify the alignment of the optical components, the system was transferred from the x-channel to an optical plate with precision-drilled holes at the optimal locations of all the optical components.

Reliable operation of the vacuum chamber and precise alignment of the optical elements of the schlieren system was crucial to the success of the wind tunnel experiments. For each test, the optics of the schlieren system were realigned to negate any disturbance between tests. Once the optical elements were set, the vacuum chamber was pumped down to approximately 6.6 Pa and the test was started immediately after the pump was switched off. Starting the test at this point ensured that the pressure in the chamber did not have time to rise significantly (from any residual leaking), thus giving the largest initial pressure ratio and the longest test run time. During each test, a series of images were taken in quick succession throughout the entire duration, to capture any flow effects revealed by the schlieren system. These images were analyzed and compared to the results of the Fluent simulation, to determine how the results from the Fluent tests apply to real, physical flows.

Using the optimized schlieren system, images of flow structures were obtained during tests with the wind tunnel. Figure 5 contains images from two different tests of the wind tunnel operating with the dual-bell contour. The right side of the image is the upstream section, where a flow pattern is clearly visible on both tests. The bright flow areas formed on the end side of an oblique shock, which is visible in Figure 5(A).

#### **IV. Fluent Analysis**

The full-scale and the wind tunnel-scaled contours were analyzed using ANSYS Fluent, operating through Workbench 14.5™. The mesh for each case was generated using the Workbench mesh generator using quadrilateral cells. The full-scale models included a large downstream section in order to examine the flow structures downstream of the nozzle.

A hot-fire nozzle test for a solid rocket booster involves complex mixtures, including combusting reactants, un-combusted and partially combusted particles mixing with the flow, non-ideal gas behavior, and significant heat transfer effects. Due to the added complexity of a full hot fire test combined with the initial testing involving a supersonic wind tunnel, the Fluent simulations were constructed to model cold flow tests. This had the added benefit

of reducing the demand on computational resources and allowing for testing multiple cases. Each case was set up assuming that the operating gas, air, behaved as an ideal gas. The  $\kappa$ -epsilon turbulence model<sup>6</sup> was selected for the simulations due to the focus on the flow structures within the nozzle. A final simplification applied to both the full-scale conventional and dual-bell nozzle cases in particular was to work mostly with relative pressure ratios starting from atmospheric and ending close to vacuum.

### A. Full Size Nozzle Comparison

The dual-bell nozzle was designed for ideal isentropic expansion at a pressure ratio of 1000 (downstream pressure) and 148 (upstream pressure). Oblique shock waves were expected to form at the inflection point at a pressure ratio of 148, which would direct most of the flow towards the exit of the nozzle. Figure 6(A) shows over-expanded flow at the nozzle exit plane for the high altitude design point (pressure ratio of 1000). This is due to the difference in assumptions used to design the nozzle and the cold flow testing assumption. The value of the ratio of specific heats for the Fluent simulations was 1.4, as it would be for a cold flow test. Using a ratio of specific heats of 1.4 and a pressure ratio of 1000 results in an isentropic area ratio of 38. In

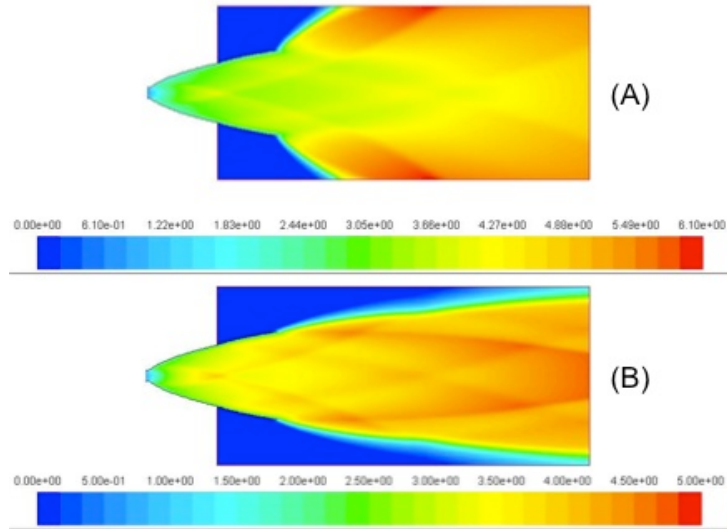


Figure 6: Dual-bell Mach contours for design pressure ratios of (A) 1000, (B) 148

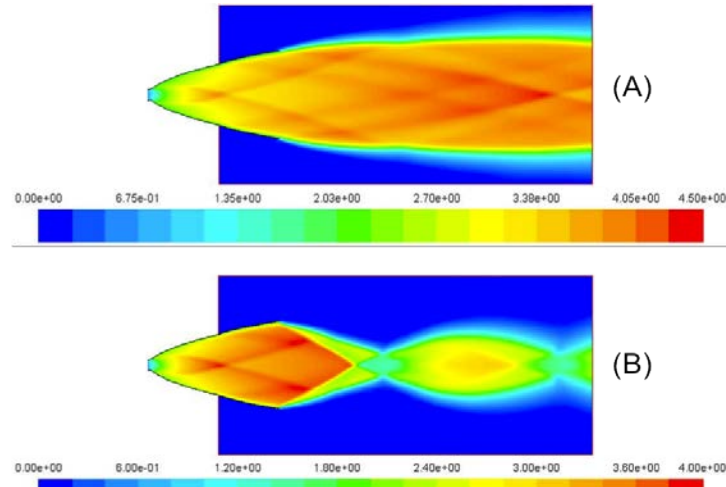


Figure 7: Dual-bell Mach contours for pressure ratios of (A) 100, and (B) 20

terms of the downstream behavior. The design pressure ratio of the conventional contour was 102, and like the dual-bell nozzle, it was over-expanded at the design pressure ratio. The main difference between the two contours can be seen in the internal flow structures. The flow within the conventional contour differed from the dual-bell nozzle in that in there was only boundary layer separation within the nozzle. No secondary flow structures formed, and the core flow was smooth as it reached the exit for the design point case (Figure 8(A)). The only extra core structures within the flow occurred in the under-expanded case where an oblique shock from the nozzle's edge met the core flow causing minor disturbances downstream that carried through into the Mach discs.

The average specific impulse over a range of backpressures was calculated using the mass averaged pressure and velocity over the nozzle's exit plane. The mass averaged pressure and velocity were calculated using Fluent for both nozzles. First, the thrust,  $T$ , that the nozzle produced was calculated using the ideal thrust equation.

$$T = \dot{m}u_e + (p_e - p_a)A_e \quad (5)$$



Where  $\dot{m}$  is the mass flow rate,  $u_e$  is the exit velocity,  $A_e$  is the exit area and  $p_e$  and  $p_a$  are the exit pressure and ambient pressure respectively. The specific impulse,  $I_{sp}$ , was calculated by dividing the thrust mass flow rate,  $\dot{m}$ , and Earth's gravitational constant,  $g_0$ , for each case and then averaging over the four cases.

$$I_{sp} = \frac{T}{\dot{m}g_0} \quad (6)$$

The algebraic average specific impulse was 64.9 s for the dual-bell contour and 71.6 s for the conventional contour nozzle. The dual-bell contour did not perform as well as the conventional nozzle contour. This could be due to the location of the inflection point on the dual-bell contour, to the optimal pressure ratio for each inflection, to boundary layer growth, or a combination of all three.

### B. Wind Tunnel Conventional and Dual-Bell Contour Comparison

The flow through the indraft supersonic wind tunnel was simulated in ANSYS Fluent. Both scale model nozzle contours were tested in order to have a point of comparison between the computational and experimental testing. A variety of backpressures were chosen to create a time-lapse series of snapshots of the flow field through the contours. Each picture presented here is a surface plot of the Mach number throughout the simulation domain.

The first test case consisted of a test with a pressure ratio (inlet to outlet) of 1013. The inlet pressure was atmospheric, matching the physical wind tunnel. For the conventional nozzle (Figure 9(A)), the flow is supersonic all the way to the exit plane of the contour, and there are Mach diamonds extending the length of the test section.

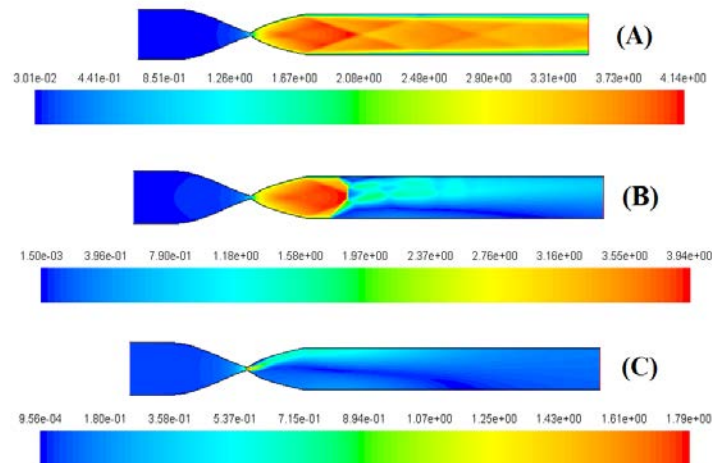


Figure 9: Conventional nozzle wind tunnel Mach contours for pressure ratios of (A) 1000, (B) 10, and (C) 2

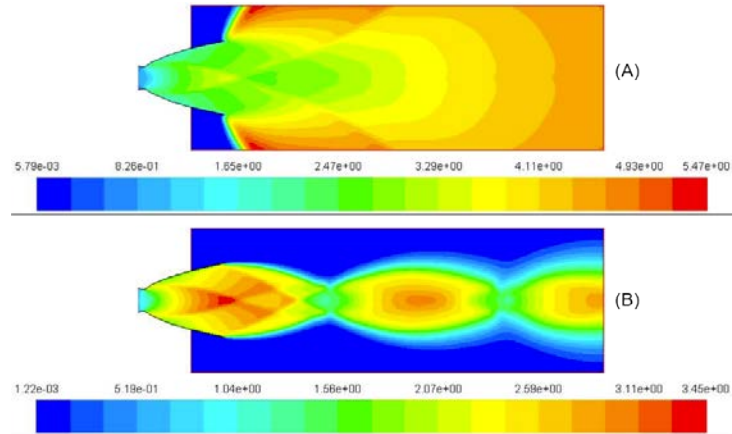


Figure 8: Conventional nozzle Mach contours for pressure ratios of (A) 1000 and (B) 10

The converging-diverging contour accelerates the flow to a peak Mach number of 4.13. As the flow continues down the post-nozzle section, a boundary layer grows, which slows the flow down to the exit Mach number of 3.6 at the center of the nozzle.

The second test case pressure ratio was 10, with the inlet pressure still remaining at atmospheric conditions. The flow is visible in Figure 9(B). There is a normal shock present just downstream of the exit of the nozzle. After the shock, a small section of the flow remains supersonic, but it is not symmetric. This is most likely due to a chaotic turbulence interaction and is a factor of over-expanded flow. If the flow could be pictured in motion, it would seesaw back and forth inside of the wind tunnel, but the results show a snapshot.

The final case would occur near the end of a test. The pressure ratio would be constantly falling, and therefore was set to 2, unchoking the nozzle as seen in Figure 9(C). In the computational results, there was still a small region of supersonic flow that was not predicted using 1D isentropic flow relations. However, the presence of a turbulent boundary layer may have created a smaller effective throat, pushing the pressure ratio threshold for choked flow down. In addition, the flow continued to exhibit the seesawing behavior seen in the previous case. All three tests were repeated for the dual-bell contour, as detailed in the next section.

The dual-bell test cases used a finer mesh than the conventional nozzle. This was a factor of the limits on the experimental testing and the different throat sizes. With the rougher mesh employed by the conventional nozzle, effects in and near the throat, as well as the effects due to the inflection point were masked and not clearly visible. In the interest of saving computational time, the meshes used were the simplest possible without losing a significant amount of clarity.

For the first test case, the dual-bell nozzle behaved in roughly the same way as the conventional nozzle, as is seen in Figure 10(A). Again, a Mach diamond structure started just beyond the exit of the nozzle. However, the maximum Mach number is 5.1 for this case due to the larger area ratio of the second bell. One interesting feature of these flows is the very small subsonic region about two nozzle lengths downstream of the end of the nozzle. This feature truncates the Mach diamonds. However, in the flow pattern itself, there are lines of reduced Mach number downstream of the inflection points. For this pressure ratio, both bells will be in full use. This would be equivalent to high-altitude flight for a launch vehicle.

In the second test case, major differences are seen when compared to the conventional nozzle. In the dual-bell test, the entire flow structure has broken down as is clearly visible in Figure 10(B). There is no clearly visible shock; instead, the flow has grossly over-expanded. This is expected, because the second bell of the contour is designed for a pressure ratio of 374 instead of the 102 for the conventional nozzle. The flow within the thin jet is still supersonic, reaching a Mach number of 3.5. There are small Mach diamond structures downstream of the core jet.

The third case for the dual-bell nozzle is similar to the conventional nozzle (Figure 10(C) and Figure 9(C), respectively). Again, there is a small supersonic region at the throat and the flow has tumbled off-center. The secondary flow jet is slightly smaller in the dual-bell case, as would be expected due to the smaller mass flow rate. The primary flow structure holds close to the upper contour at this instant, but we would expect the flow to not favor either direction.

## V. Comparison of Schlieren Images and CFD Results

The flow structures imaged in tests using the dual-bell contours are consistent with those obtained through Fluent analysis of the dual-bell wind tunnel contour. Boundary layer flow features were observed on the schlieren images collected during wind tunnel testing of the dual-bell contour. These features were also noted in the Fluent simulations of the dual-bell wind-tunnel contours at a pressure ratio of 10 (Figure 10(B)). While these two images compare the density gradient of the flow and the Mach number, the Mach number is dependent on the density. The

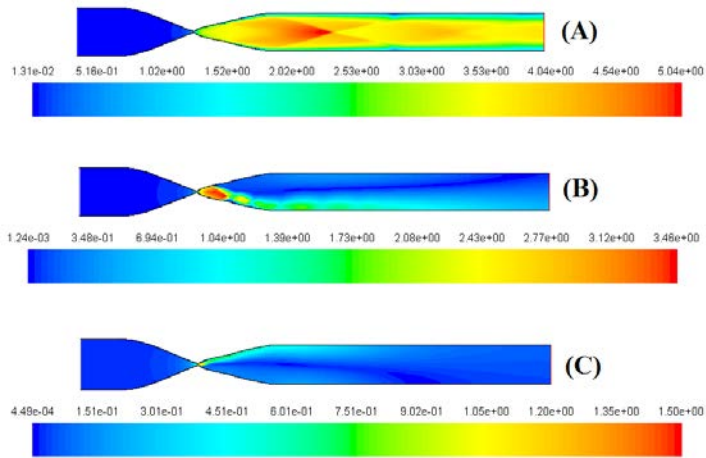


Figure 10: Dual-bell wind tunnel Mach contours for pressure ratios of (A) 1000, (B) 10, and (C) 2.



Figure 11: Comparison of schlieren (top) and Fluent (bottom) images of the density gradient.

first boundary layer flow feature appeared approximately 18 seconds into a 115 second test. They were visible at the tail end of an oblique shock, which appeared approximately 15 seconds into the test. This phenomenon is shown in Figure 11, where a schlieren image (top) showing flow features noticed 18 sec into the test were captured by a density gradient plot generated by Fluent. This suggests that both sets of results were consistent with physical phenomena and are valid for this application.

## VI. Conclusion

This project addressed a common issue in nozzle design and its effect on the efficiency of rocket engine systems. A dual-bell nozzle contour design procedure was developed and used to investigate a possible nozzle that could be implemented on a sounding rocket or nanosatellite launcher. The contour was adapted for physical testing in a supersonic wind tunnel. Schlieren imaging of flow in the tunnel showed oblique shock structures and boundary layer flow features. Analysis of the dual-bell contour in both configurations was performed using ANSYS Fluent simulations, and similar simulations were run for a conventional contour. This was done to compare flow structures within the proposed dual-bell contour to those of a conventional nozzle contour as well as to compare their performance characteristics. The conventional nozzle contour performed better than the proposed dual-bell contour, with an average specific impulse of 71.6 s compared to the dual-bell's 64.9 s. Future investigations will examine changing the inflection point to different locations within the nozzle and optimizing the design point pressure ratios. Mach contours generated from the Fluent simulations show similar flow features to the schlieren images from the wind tunnel testing. This indicates that the Fluent simulations are both valid and robust for this application. Further research shall be conducted to measure flow characteristics in the wind tunnel for a more accurate comparison with the Fluent wind tunnel simulations, leading to development of a full-size nozzle for cold-flow testing.

## Acknowledgments

We would like to thank Professor John Blandino for his help and guidance, Jonathon Jones of NASA for generously providing us with information on the ascent profile of the Nanolaunch 1250 launch system, and the WPI Machine Shop for their help in manufacturing the wind tunnel contours.

## References

- <sup>1</sup>Horn, M. & Fisher, S. Dual-bell altitude compensating nozzles. NASA Propulsion Engineering Research Center, 1993. 140-147.
- <sup>2</sup>Hagemann, G., Immich, H., Nguyen, T. V. & Dumnov, G. E. 1998. Advanced rocket nozzles. *Journal of Propulsion and Power*, 14,620- 634.
- <sup>3</sup>Jones, J. E. 2013. Nanolaunch 1200. NASA-Marshall Space Flight Center
- <sup>4</sup>Ceviz, M, and Kaymaz, I. 2005. Temperature and air-fuel ratio dependent specific heat ratio functions for lean burned and unburned mixture. *Journal of Energy Conversion Management*, 46, 2387-2404.
- <sup>5</sup>Settles, G. S. 2001. *Schlieren and Shadowgraph Techniques: Visualizing Phenomena in Transparent Media*. Heidelberg, Germany: Springer-Verlag Berlin Heidelberg.
- <sup>6</sup>Moin, P. & Mahesh, K. 1998. Direct Numerical Simulation: A Tool in Turbulence Research. *Annual Review of Fluid Mechanics*, 40.
- <sup>7</sup>Kulhanek, S. 2012. Design, Analysis, and Simulation of Rocket Propulsion System. Master of Science, University of Kansas.
- <sup>8</sup>Bugden, W., Fitton, K., Folinas, G., Fournier, N., Hogan, G., Ito, M., Lambert, J., Patel, N., Shin, D.-U., Wong, G. & Ziegler, E. 2013. Design and Construction of a Supersonic Wind Tunnel with Diagnostics Worcester, Massachusetts: Worcester Polytechnic Institute.
- <sup>9</sup>Östlund, J. 2002. Flow Processes in Rocket Engine Nozzles with Focus on Flow Separation and Side-Loads. Royal Institute of Technology.
- <sup>10</sup>Nurnberger-Genin, C. & Stark, R. 2009. Flow transition in dual bell nozzles. *Shock Waves*, 19, 265-270.
- <sup>11</sup>Nasuti, F., Onofri, M. & Martelli, E. 2005. Role of wall shape on the transition in axisymmetric dual-bell nozzles. *Journal of propulsion and power*, 21, 243-250.
- <sup>12</sup>Sutton, G. 2010. *Rocket Propulsion Elements*, Wiley.
- <sup>13</sup>Verma, S. B., Stark, R. & Haidn, O. 2012. Gas Density Effects on Dual-Bell Transition Behavior. *Journal of Propulsion and Power*, 28, 9.

- <sup>14</sup>Hagemann, G. & Frey, M. 2008. Shock pattern in the plume of rocket nozzles: Needs for design consideration *Shock Waves*, 9.
- <sup>15</sup>Frey, M. & Hagemann, G. 1999. Critical assessment of dual-bell nozzles. *Journal of propulsion and power*, 15, 137-143.
- <sup>16</sup>Nurnberger-Genin, C. & Stark, R. 2010. Experimental Study on Flow Transition in Dual-Bell Nozzles. *Journal of Propulsion and Power*, 26, 6.
- <sup>17</sup>Stark, R., Bohm, C., Haidn, O. J. & Zimmermann, H. 2006. Cold Flow Testing of Dual-Bell Nozzles in Altitude Simulation Chambers. European Conference for Aerospace Sciences. DLR, German Aerospace Center.
- <sup>18</sup>Auld & Srinivas 2006. A Body Placed in Subsonic and Supersonic Flows. *Aerodynamics for Students*.
- <sup>19</sup>Akin, J. E. 1994. *Finite Elements for Analysis and Design*, San Diego, CA, Academic Press Limited.
- <sup>20</sup>Mathew, J. 2010. Large Eddy Simulation. *Defence Science Journal*, 60,8.
- <sup>21</sup>Spalart, P. R. 2009. Detached-Eddy Simulation. *Annual Review of Fluid Mechanics*, 24.
- <sup>22</sup>Durbin, P. P.-R., B. A. 2010. *Statistical Theory and Modeling for Turbulent Flow*. 2nd ed. Hoboken, NJ, USA: Wiley

## **Appendix B: How to Use the Schlieren System**

- 1) Assemble the wind tunnel with the chosen contours, ensuring that caulk seals between the brackets and endplates are not broken and that the o-rings are in continuous contact with the windows.
- 2) Attach the wind tunnel to the vacuum chamber, ensuring that the windows are oriented perfectly vertically. Any error in the vertical orientation will result in light interference that will pollute the image.
- 3) Turn on the light.
- 4) Temporarily remove the slit and the razor blade from the light path and position the schlieren system such that the silhouette of the desired area of the tunnel is shown on the screen. This involves moving the entire table. Be sure to keep the light path perpendicular to the wind tunnel.
- 5) Reposition the slit to focus the image on the screen (approximately 4 cm away from the collimating lens).
- 6) Reposition the razor blade to just beyond the focal point of the second mirror. Adjust the height of the blade so that it cuts off half of the light beam. The highest contrast images will be produced if the image is a uniform, dim shade while no test is being run.
- 7) Test the alignment by spraying compressed air or holding a candle near the test section.

### **Troubleshooting**

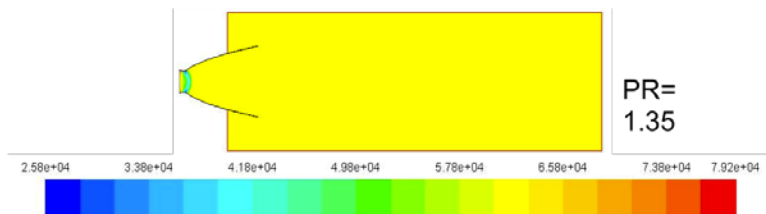
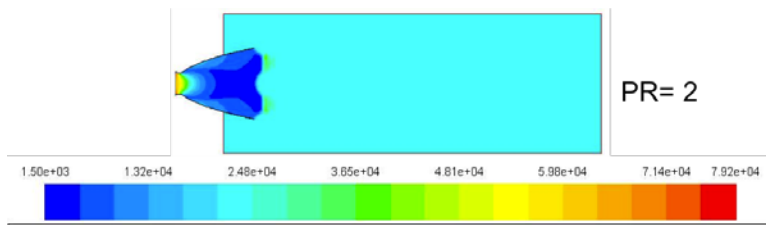
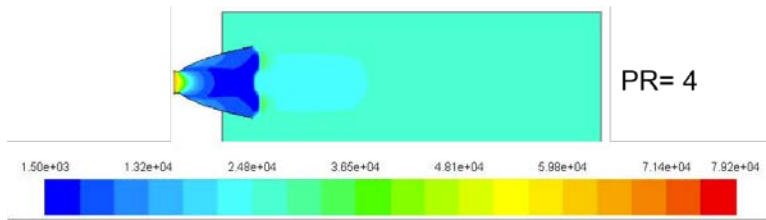
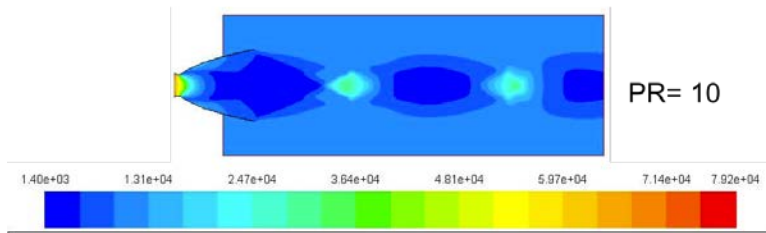
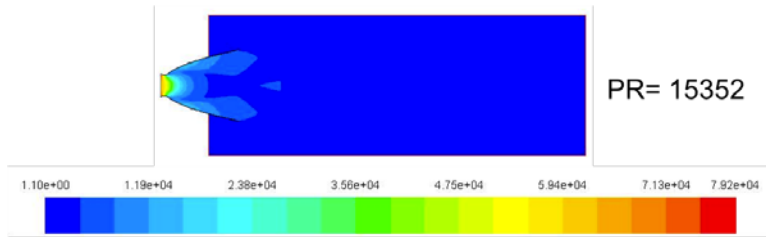
- If the image is out of focus, adjust the slit.
- If the image is low contrast, adjust the position and height of the razor blade.
- If the image has bright lines parallel to one of the contours, then the wind tunnel is not perfectly vertical. Remove the schlieren system, loosen the bolts that connect the wind tunnel to the vacuum chamber, and adjust the position until it is vertical.



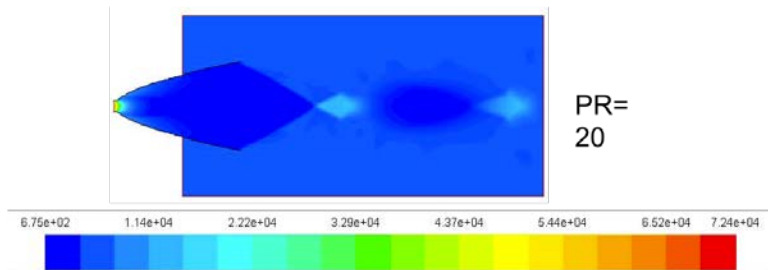
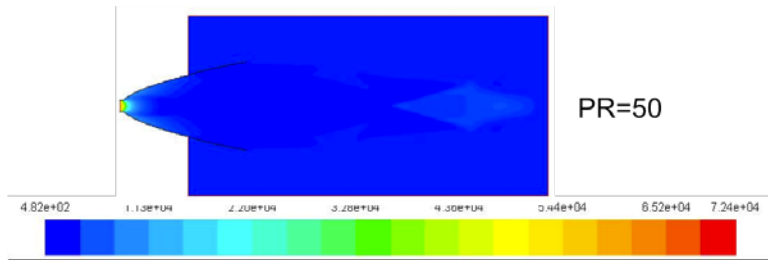
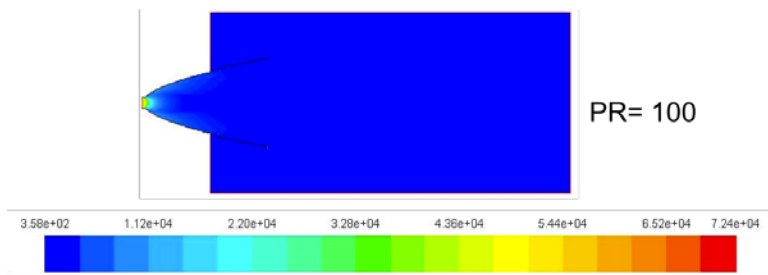
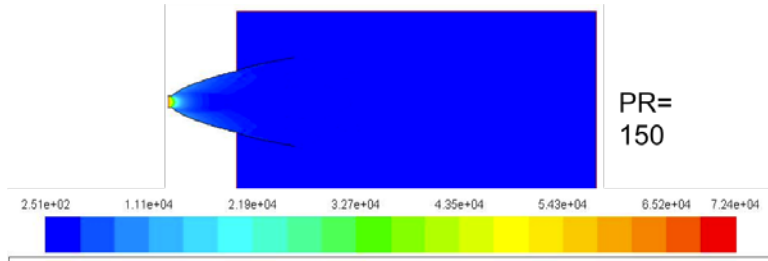
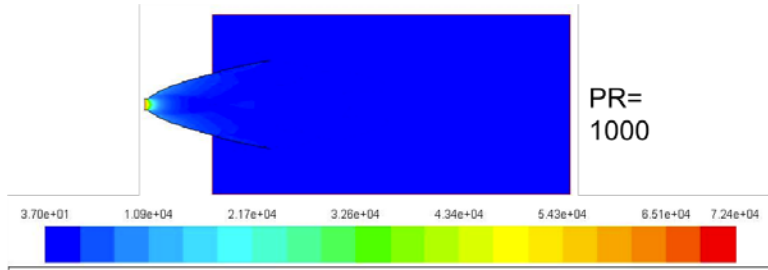
**Figure 58: Example of Light Interference**

# Appendix C: Fluent Contours of Pressure

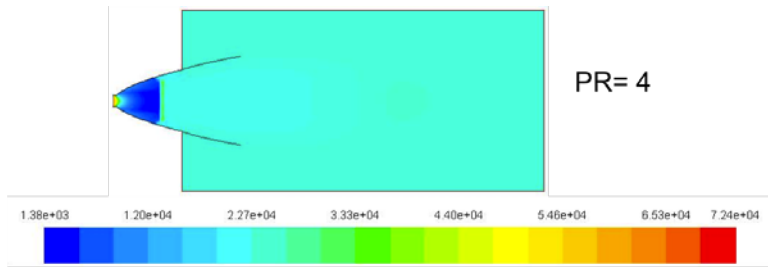
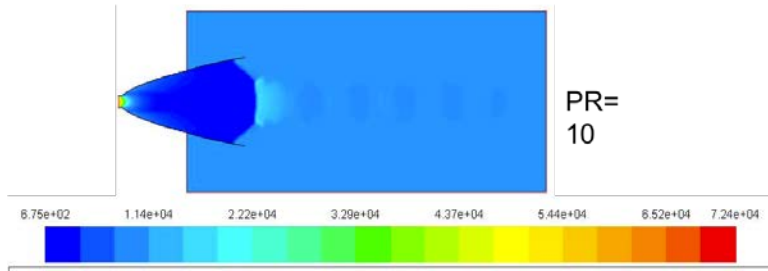
Rao Pressure Contours:



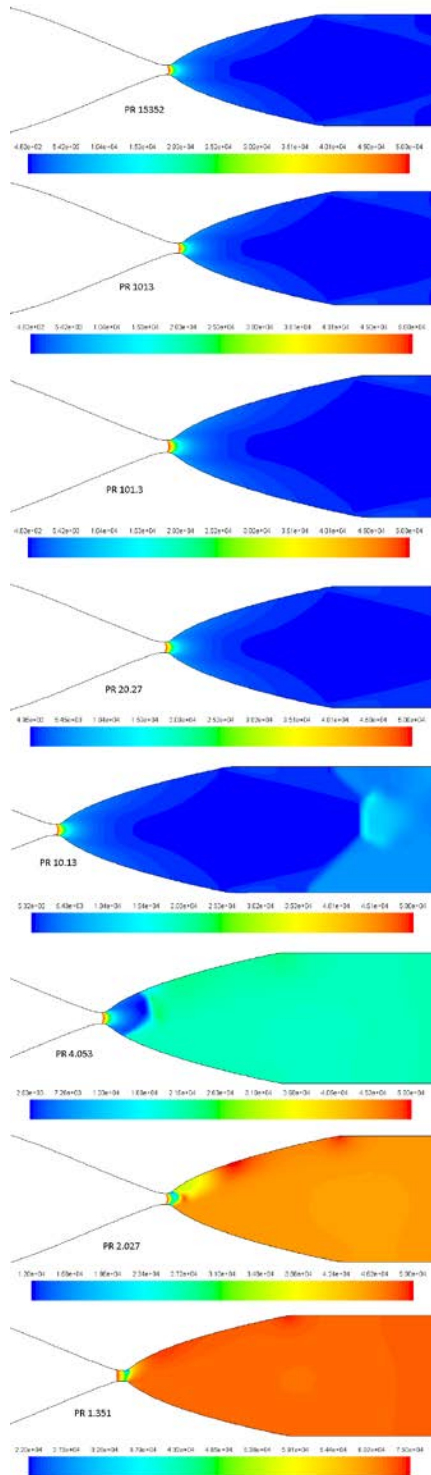
Dual-Bell Pressure Contours:



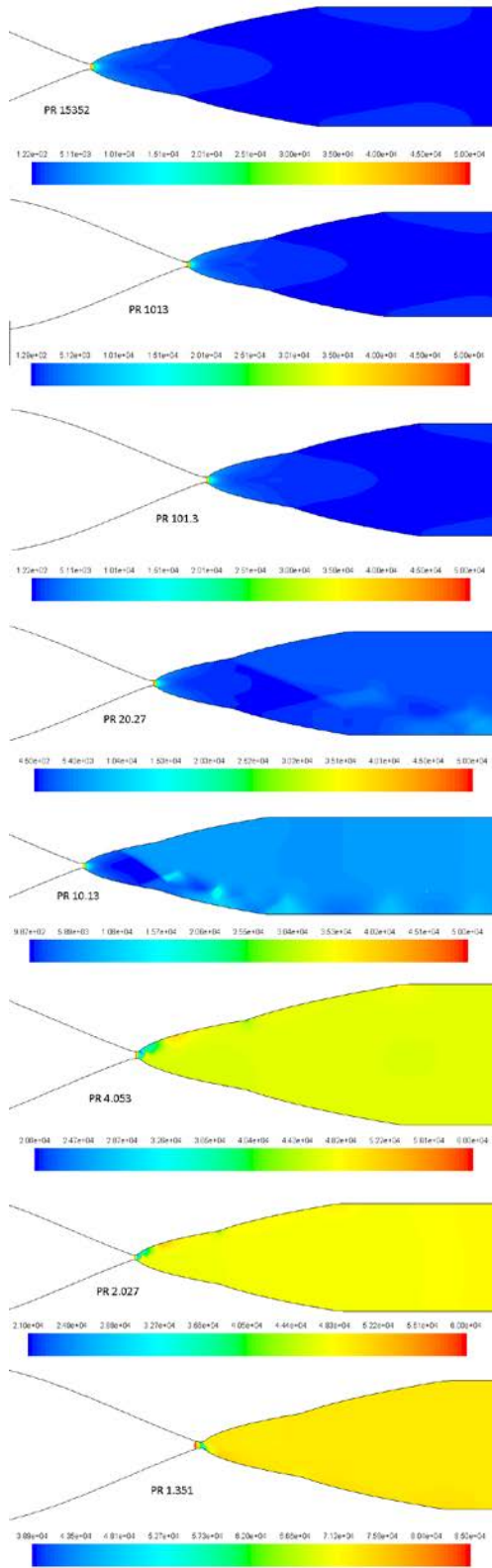




# Rao Wind Tunnel Nozzle Pressure Contours



# Dual-Bell Wind Tunnel Nozzle Pressure Contours



## Appendix D: Parabolic Coefficient Calculations

First parabola length:  $L_n = \frac{K(\sqrt{\varepsilon}-1)R_t}{\tan(\theta_e)}$

Equation of first curve:  $x^2 + (y - (R_t + 1.5R_t))^2 = (1.5R_t)^2$

Re-written:  $y = -\sqrt{(1.5R_t)^2 - x^2} + 2.5R_t$

Equation of second curve:  $x^2 + (y - (R_t + 0.382R_t))^2 = (0.382R_t)^2$

Re-written:  $y = -\sqrt{(0.382R_t)^2 - x^2} + 1.382R_t$

Derivative of first curve:  $\frac{dy}{dx} = \tan(\theta_1) = \frac{x_1}{\sqrt{(1.5R_t)^2 - x_1^2}}$

$$x_1 = -1.5R_t \sin(\theta_1)$$

Equation of parabola, for Rao and first parabola dual-bell:

$$x = ay^2 + by + c$$

Slope of parabola at point N:  $\frac{dy}{dx} = \tan(\theta_N) = \frac{x_N}{\sqrt{(0.382R_t)^2 - x^2}}$

Slope of curve one at point N:  $x_N = 0.382R_t \sin(\theta_N)$

Definition of  $x_N$ :  $x_N = aR_N^2 + bR_n + c$

Slope at  $x_N$ :  $\frac{dy}{dx} = \tan(\theta_N) = \frac{1}{2aR_N + b}$

Slope at exit (both dual-bell and Rao):  $\frac{dy}{dx} = \tan(\theta_e) = \frac{1}{2aR_e + b}$

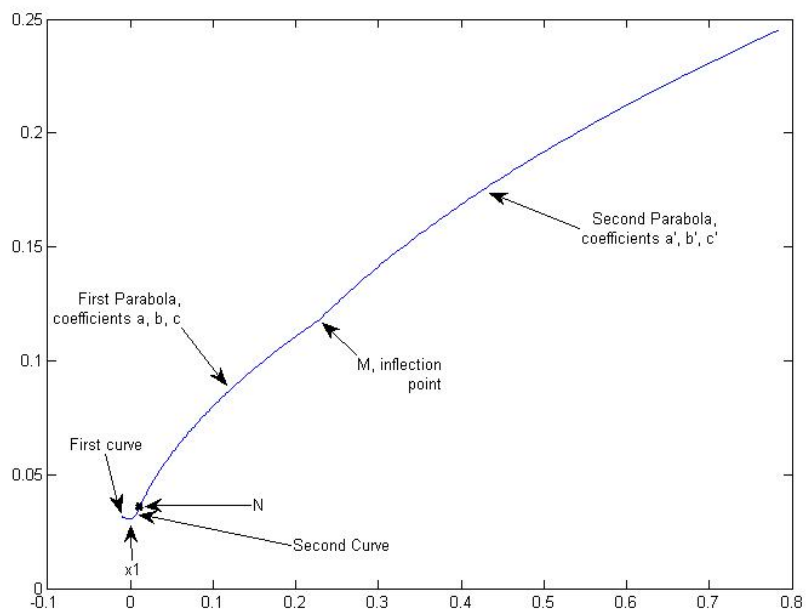
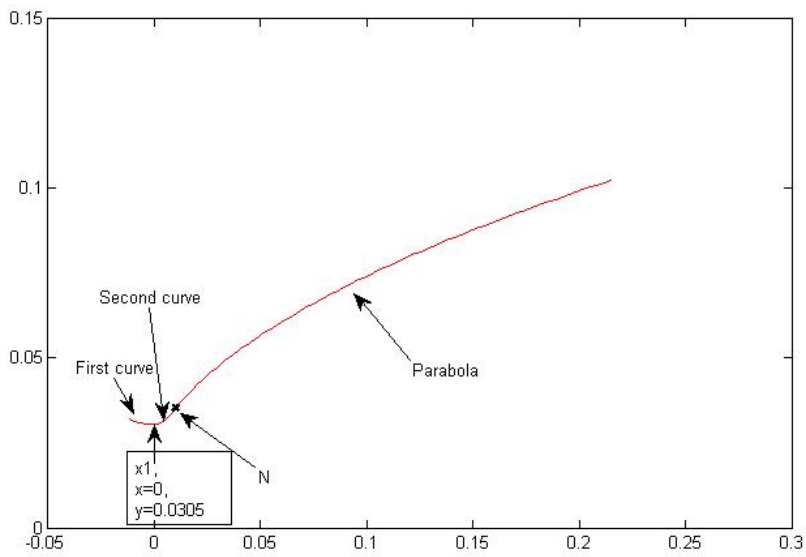
Full system of equations for the parabolic coefficients for the first parabola (also includes the only parabola for the Rao nozzle)

$$\begin{bmatrix} 2R_N & 1 & 0 \\ 2R_e & 1 & 0 \\ R_N^2 & R_N & 1 \end{bmatrix} \begin{bmatrix} a \\ b \\ c \end{bmatrix} = \begin{bmatrix} 1 \\ \tan(\theta_N) \\ 1 \\ \tan(\theta_e) \\ x_N \end{bmatrix}$$

Full length of dual-bell nozzle:  $L_M = \frac{K_M(\sqrt{\varepsilon}-1)R_t}{\tan(\theta_e)}$

Full system of equations for the second parabola of the dual-bell nozzle:

$$\begin{bmatrix} 2R_M & 1 & 0 \\ 2R_e & 1 & 0 \\ R_N^2 & R_N & 1 \end{bmatrix} \begin{bmatrix} a' \\ b' \\ c' \end{bmatrix} = \begin{bmatrix} 1 \\ \tan(\theta_M) \\ 1 \\ \tan(\theta_e) \\ x_M \end{bmatrix}$$



Note: The throat of the dual-bell nozzle is labeled and constructed the same as the Rao nozzle in the pictures.

## Appendix E: MATLAB Scripts

```
% Isentropic flow relations, pressure ratio input
% Called by all of the following codes
function [TR, PRt, TRt, M, AR]=isen_rlms(PR, k)
%Date Modified: 10/29/2013, Hannah McCallum
%given the Press. ratio; Calculates the pressure & temp ratios overall
%and at throat. Also calculates the area ratio and mach number.
%inputs are PR and the ratio of specific heats k

TR=PR^((k-1)/k);%temperature ratio overall
TRt=1+(k-1)/2;%TR at throat
PRt=(1+(k-1)/2)^(k/(k-1));%PRT
M=sqrt(2/(k-1)*(TR-1));%Mach number
AR=((k+1)/2)^(-(k+1)/(2*(k-1)))*(TR)^((k+1)/(2*(k-1)))/M;%Area ratio

%size_eqn-- Sizing the Rao nozzle and plotting it
%assumes a circular cross section
% inputs: K=percent length as compared to a conical nozzle
%with 15 deg 1/2 angle. AR=area ratio, th_e=exit angle
%th_N=initial angle, th_l=angle coming out of the combustion chamber
clear all
close all
clc
%Define necessary parameters
F=17405.7*4.4482216;%N, Thrust
mdot=7.119;%kg/s, mass flow rate
k=1.23;%ratio of specific heats
Mm=28;%kg/kmol, molar mass
R=8.314/(Mm*10^-3);%J/kg-K, gas constant
Isp=249;%s, specific impulse
Pc=1500;%psi, chamber pressure
Tc=1100;%K, guesstimate
Pa=14.7;%psi, SL pressure, initial design point
PR=Pc/Pa;%pressure ratio
g=9.8;%m/s^2
[TR, PRt, TRt, M, AR]=isen_rlms(PR, k);

%Calculate throat area
Tt=Tc*TRt;%K, temp at throat
Pt=Pc*PRt*101.3e3/14.7;%Pa, throat pressure
At=F/(Isp*Pt)*sqrt(R*Tt/(k*g));%m^2

Rt=sqrt(At/pi);%m, throat radius
Re=sqrt(AR)*Rt;%m, exit radius

%Calculate length of nozzle
K=0.8;% percent length of same AR conical nozzle
Ln=K*(sqrt(AR)-1)*Rt/tan(15*pi/180);%m, length of nozzle

%begin defining points
th_l=15*pi/180;%rad, angle at first circle
th_N=40*pi/180;%rad, angle b/w throat exit and parabola
```

```

x1=-1.5*Rt*sin(th_1);%x point of circle entering the nozzle
xN=0.382*Rt*sin(th_N);%X point at transition to parabola

%parabola coefficients
RN=-sqrt((0.382*Rt)^2-xN^2)+1.382*Rt;%radius at xN
tmp1=[2*RN, 1, 0;
      RN^2, RN, 1;
      Re^2, Re, 1];

tmp2=[1/tan(th_N); xN; Ln];
dd=tmp1\tmp2;
a=dd(1); b=dd(2); c=dd(3);
x_c1=linspace(x1,0,50);%note, in cm
x_c2=linspace(0,xN,50);%circle exiting nozzle
y3=linspace(RN,Re,100);

th_e=1/(2*a*Re+b)*180/pi%deg, flow exit angle
ufo=size(x_c1,2); ufa=size(x_c2,2); %ufe=size(x_c3,2);
y1=-((1.5*Rt)^2*ones(1,ufo)-x_c1.^2).^5+2.5*Rt*ones(1,ufo);
y2=-((0.382*Rt)^2*ones(1,ufa)-x_c2.^2).^5+1.382*Rt*ones(1,ufa);
x_c3=a*y3.^2+b*y3+c*ones(1,size(y3,2));

x=[x_c1,x_c2,x_c3];
y=[y1,y2,y3];
z=ones(length(x));
plot(x,y,'r')
%axes('square');
% hold on
% plot(x_c2,y2);
% plot(x_c3,y3);
zz=[x;y;zeros(1,length(x))];
% fid=fopen('nozzle.txt','w');
% fprintf(fid,'%6.2f %12.8f\n',zz);
% fclose(fid);

% xlswrite('nozzle.xls',zz);

```



```

%% Sizing the dual bell nozzle
% uses input pressure ratios to size the throat and
%the nozzles

clear all
close all
clc
%Define necessary parameters
F=17405.7*4.4482216;%N, Thrust
mdot=7.119;%kg/s, mass flow rate
k=1.23;%ratio of specific heats
Mm=28;%kg/kmol, molar mass
R=8.314/(Mm*10^-3);%J/kg-K, gas constant
Isp=249;%s, specific impulse
Pc=1500;%psi, chamber pressure
Tc=1100;%K, guesstimate
Pai=10.1;%psi, SL pressure, initial design point
Paf=1.5;
PRi=Pc/Pai;%pressure ratio
PRf=Pc/Paf;
g=9.8;%m/s^2

[TRm,PRtm,TRtm,Mm,ARm]=isen_rlns(PRi,k);
[TRf,PRtf,TRtf,Mf,ARf]=isen_rlns(PRf,k);

%Calculate throat area
Ttf=Tc*TRtf;%K, temp at throat
Ptf=Pc*PRtf*101.3e3/14.7;%Pa, throat pressure
Atf=F/(Isp*Ptf)*sqrt(R*Ttf/(k*g));%m^2
Rt=sqrt(Atf/pi);%m, throat radius
Rm=sqrt(ARm)*Rt;%m, first radius
Rf=sqrt(ARf)*Rt;%m, exit radius

%Define lengths of each section
K1=0.7; K2=0.8;% percent length based off of 15 deg conical nozzle
th_N=40*pi/180;% circle-parabola transition angle
th_f=9.5*pi/180;% Flow exit angle
th_M=20*pi/180;%flow entrance angel at M pt
Lm=K1*(sqrt(ARm)-1)*Rt/tan(15*pi/180);% m, M point
Lf=K2*(sqrt(ARf)-1)*Rt/tan(15*pi/180);% m, Exit length
xN=sin(th_N)*0.382*Rt;%m, x position at N point
RN=-sqrt((0.382*Rt)^2-xN^2)+1.382*Rt;%radius at xN
x1=-sin(15*pi/180)*1.5*Rt;%m, x posn into throat
% calculate both parabolic coefficients
tmp1nm=[2*RN, 1 0;% 1/tan(th_N)=2a*radius_N+b
        RN^2, RN, 1;
        Rm^2, Rm, 1];
tmp2nm=[1/tan(th_N); xN; Lm];

p_cnm=tmp1nm\tmp2nm;%solve for the coefficients
a_nm=p_cnm(1); b_nm=p_cnm(2); c_nm=p_cnm(3);

tmp1mf=[Rm^2, Rm, 1;

```

```

2*Rm, 1, 0;
2*Rf, 1, 0];
tmp2mf=[Lm; 1/tan(th_M); 1/tan(th_f)];

p_cmf=tmp1mf\tmp2mf;
a_mf=p_cmf(1); b_mf=p_cmf(2); c_mf=p_cmf(3);

%Plotting
th_f=1/(2*a_mf*Rf+b_mf)*180/pi%deg, flow exit angle
th_Nn=1/(2*a_nm*Rm+b_nm)*180/pi%deg
th_Np=1/(2*a_mf*Rm+b_mf)*180/pi%deg
x_c12=linspace(x1,0,50);%x-coordinates into throat
x_c2n=linspace(0,xN,50);%x-coordinates out of throat
y_NM=linspace(RN,Rm,100);%y-coordinates in first parabola
y_MF=linspace(Rm,Rf,100);%y-coordinates second bell
ufa=size(x_c12); ufe=size(x_c2n); ufi=size(y_NM);
ufo=size(y_MF);

y_12=-((1.5*Rt)^2*ones(ufa)-x_c12.^2).^0.5+2.5*Rt*ones(ufa);
y_2n=-((0.382*Rt)^2*ones(ufe)-x_c2n.^2).^0.5+1.382*Rt*ones(ufe);
x_NM=a_nm*y_NM.^2+b_nm*y_NM+c_nm*ones(ufi);
x_MF=a_mf*y_MF.^2+b_mf*y_MF+c_mf*ones(ufo);

plot(x_c12,y_12)
hold on
plot(x_c2n,y_2n)
plot(x_NM,y_NM)
plot(x_MF,y_MF)

zz=[x_c12, x_c2n,x_NM,x_MF;
y_12, y_2n, y_NM,y_MF;
zeros(1,length([x_c12, x_c2n,x_NM,x_MF]))];

%xlswrite('dual_bell1125.xlsx',zz')

```

```

%% Find the location of shocks within the DB and Rao nozzle
%ref. Gas Dynamics Third Ed. By John and Keith
% process on P. 138
clear all
close all
clc
k=1.4;
%Rao nozzle
%AR1=11.2983;%Area ratio
%DB nozzle full expansion
AR1=64.560298396194440;%AR second bell
% AR1=31.475417685853465; %AR first bell
PR=4.05^-1;%Pressure ratio SL
%PR=3.8/1500; %PR first bell
% PR=1.5/1500; %PR second bell
[TR,PRt,TRt,M,AR]=isen_rlns(PR,k);

Me2=-1/(k-1)+sqrt((1/(k-1))^2+(2/(k-1))*(2/(k+1))^...
((k+1)/(k-1))*PR^-2*AR1^-2);
Me=sqrt(Me2);
%Step2
PR2=(1+(k-1)/2*Me2)^(-k/(k-1)); %Pe/Po2
%Step 3
PR3=PR/PR2;%Po2/Po1
AR2=PR3^-1;
%Step 4
a=AR2; b=(k+1)/(2*(k-1)); c=2/(k+1); %Coefficients
Mtmp=3*ones(1000,1);%initial guess mach number
f=zeros(size(Mtmp));
df=zeros(size(Mtmp));
for i=1:length(Mtmp)
    f(i)=a*Mtmp(i)-c^b*(1+Mtmp(i)^2/(2*b*c))^b;
    df(i)=a-c^(b-1)*Mtmp(i)*(1+Mtmp(i)^2/(2*b*c))^(b-1);
    Mtmp(i+1)=Mtmp(i)-f(i)/df(i);
    if abs(Mtmp(i+1)-Mtmp(i))<=1e-6
        M1=Mtmp(i);
        break
    end
end
end

%Step 5
ARsl=1/M1*((2/(1+k))*(1+(k-1)/2*M1^2))^((k+1)/(2*(k-1))) %AREA ratio shock location
Rt= 0.030493751973379; %m, throat radius

Rsl=Rt*sqrt(ARsl)

```

```

%Wind Tunnel Contours in Inches
clc
clear all
close all
format long
%% Rao Contour
%7 segments
%12 inches overall length
x1=linspace(-3,-2,500);
x2=linspace(-2, -.113519111,500);
x3=linspace(-.113519111,0,500);
x4=linspace(0, .0543321508,500);
y5=linspace(0.064029642509604,.5,500);
y6=linspace(.5, 0.511057497691736,500);
x7=linspace(1.45061952,9,500);

y1=.651*ones(1,length(x1));
%Segment One Equation
%%y=.651
%Runs from -3" to -2"

tmp1=[x2(1)^3, x2(1)^2, x2(1), 1;
      3*x2(1)^2, 2*x2(1), 1, 0;
      x2(500)^3, x2(500)^2, x2(500), 1;
      3*x2(500)^2, 2*x2(500), 1, 0];

tmp2=[.651; 0; 0.064270838953427; -tan(.349065850398866)];
dd=tmp1\tmp2;
a2=dd(1); b2=dd(2); c2=dd(3); d2=dd(4);
y2=a2.*x2.^3+b2.*x2.^2+c2.*x2+d2;
%Segment Two Equation
%%y=0.072514515238398x^3+0.133423178936475x^2-0.336481467114878x+0.024460471931529
%Runs from -2" to -.113519111"

y3=-((0.331907676376092)^2-x3.^2).^5+0.376162033226238;
%Segment Three Equation
%%y=-sqrt(0.110162705637377-x^2)+0.376162033226238
%Runs from -.113519111" to 0"

y4=-((0.084525821583778)^2-x4.^2).^5+0.128780178433924;
%Segment Four Equation
%%y=-sqrt(0.007144614514413-x^2)+0.128780178433924
%Runs from 0" to .0543321508"

%%WARNING: Five and Six are defined in terms of y. WARNING

tmp1=[2*y5(1), 1, 0;
      y5(1)^2, y5(1), 1;
      2*y5(500), 1, 0];

```

```

tmp2=[1/tan(0.698131700797732); x4(500); 1/tan(0.208408020651391)];
dd=tmp1\tmp2;
x5=dd(1)*y5.^2+dd(2)*y5+dd(3);
%Segment Five Equation
%%x=4.056302035911394y^2+0.672306454053439y-0.005345398401642
%%y=1.79231*10^(-17)*sqrt(7.6744*10^32*x+2.54813*10^31)-0.0828718
%Runs from .0543321508" to 1.344880377"

parabola_end_slope=2*dd(1)*y5(length(x5))+dd(2);
th_sweep=atan(parabola_end_slope^-1)*180/pi;
del_x=tan(th_sweep*pi/180)*y5(500);
radius=sqrt(y5(500)^2+del_x^2);
endptx=x5(length(y5))+del_x;
endpty=radius;

x6=-sqrt(radius.^2-y6.^2)+endptx;
%Segment Six Equation
%%x=-sqrt(0.261180810669137-y^2)+1.450622690112467
%%y=sqrt(0.261180810669137-(1.450622690112467-x)^2)
%Runs from 1.344880377" to 1.45061952"

y7=0.511057498*ones(1,length(x5));
%Segment Seven Equation
%%y=0.511057498
%Runs from 1.45061952" to 9"
hold on
plot(x1,y1)
plot(x2,y2)
plot(x3,y3)
plot(x4,y4)
plot(x5,y5)
plot(x6,y6)
plot(x7,y7)

%% Dual Bell Contour
%8 Segments
%12 inches long

x1b=linspace(-3,-2,500);
x2b=linspace(-2, -.0491587,500);
x3b=linspace(-.0491587,0,500);
x4b=linspace(0, .03109164,500);
y5b=linspace(0.036641044,.25,500);
y6b=linspace(.25,0.5,500);
y7b=linspace(.5,.5069515,500);
x8b=linspace(1.961474,9,500);

y1b=.651*ones(1,length(x1b));
%Segment One Equation
%%y=.651
%Runs from -3" to -2"

```

```

tmpB1=[x2b(1)^3, x2b(1)^2, x2b(1), 1;
      3*x2b(1)^2, 2*x2b(1), 1, 0;
      x3b(1)^3, x3b(1)^2, x3b(1), 1;
      3*x3b(1)^2, 2*x3b(1), 1, 0];

tmpB2=[.651; 0; 0.031796475610309; -tan( 0.349065850398866)];
p_B=tmpB1\tmpB2;
y2b=p_B(1)*x2b.^3+p_B(2)*x2b.^2+p_B(3)*x2b+p_B(4);
%Segment Two Equation
%%y=0.071164465280019x^3+0.125455470338936x^2-0.352151702004480x+0.014190436875445
%Runs from -2" to -.0491587"

y3b=-((0.189934586397618)^2-x3b.^2).^0.5+0.215259197917300;
%Segment Three Equation
%%y=-sqrt(0.036075147110034-x^2)+0.215259197917300
%Runs from -.0491587" to 0"

y4b=-((0.048370008002593)^2-x4b.^2).^0.5+0.073694619522276;
%Segment Four Equation
%%y=-sqrt(0.002339657674171-x^2)+0.073694619522276
%Runs from 0" to .03109164"

%%WARNING: DEFINED IN TERMS OF Y FOR THE NEXT THREE

tmpE1=[2*y5b(1), 1, 0;
      y5b(1)^2, y5b(1), 1;
      y5b(500)^2, y5b(500), 1];
tmpE2=[1/tan(0.698131700797732); x4b(500); 0.7874];

p_E=tmpE1\tmpE2;
x5b=p_E(1)*y5b.^2+p_E(2)*y5b+p_E(3);
%Segment Five Equation
%%x=11.028438365209242y^2+0.38356660181237x+0.002230951721330
%%y=(-2.11791)*10^(-17)*sqrt(2.02148*(10^32)*(x)+2.23199*10^29)-0.0173899
%Runs from 0.03109164" to 0.7874"

tmpF1=[y6b(1)^2, y6b(1), 1;
      2*y6b(1), 1, 0;
      2*y6b(500), 1, 0];
tmpF2=[x5b(500); 1/tan(0.349065850398866); 1/tan(0.165806278939461)];

p_F=tmpF1\tmpF2;
x6b=p_F(1)*y6b.^2+p_F(2)*y6b+p_F(3);
%Segment Six Equation
%%x=6.456573889956910x^2-0.480809525523833x+0.504066513258651
%%y=1.65541*10^(-17)*sqrt(5.65183*10^32*x-2.79831*10^32)+0.0372341
%Runs from .7874 to 1.8778"

parabola_end_slope=2*p_F(1)*y6b(500)+p_F(2);
th_sweep=atan(parabola_end_slope^-1)*180/pi;
del_x=tan(th_sweep*pi/180)*y6b(500);
radius=sqrt(y6b(500)^2+del_x^2);
endptx=x6b(length(y6b))+del_x;

```

```

endpty=radius;

x7b=-sqrt(radius.^2-y7b.^2)+endptx;
%Segment Seven Equation
%%x=-sqrt(0.257000887203544-y^2)+1.961476527526672
%%y=sqrt(0.257000887203544-(1.961476527526672-x)^2)
%Runs from 1.8778" to 1.96044"

y8b=y7b(500)*ones(1,length(x7b));
%Segment Eight Equation
%%x=.5069515
%Runs from 1.96044" to 9"

figure
hold on
plot(x1b,y1b)
plot(x2b,y2b)
plot(x3b,y3b)
plot(x4b,y4b)
plot(x5b,y5b)
plot(x6b,y6b)
plot(x7b,y7b)
plot(x8b,y8b)

```